Substrate Effect, Pile-Up and Sink-In Factors during Thin Film Nanoindentation

by

Kevin Russell Schwieker

A thesis submitted to the Graduate Faculty of
Auburn University
in partial fulfillment of the
requirements for the Degree of
Master of Science

Auburn, Alabama
December 12th, 2011

Keywords: Nanoindentation, Thin Films, Erroneous Contact Area, Instrumented Indentation Testing, Continuous Stiffness Measurement

Copyright 2011 by Kevin Russell Schwieker

Approved by

Barton Prorok, Chair, Associate Professor of Materials Engineering
Ruel Overfelt, Professor of Materials Engineering
Robert Jackson, Associate Professor of Mechanical Engineering

Abstract

Theoretical and experimental models continue to be developed for thin-film nanoindentation that attempt to account for substrate effects in differing film-substrate combinations. While many models have been developed to extract film properties independent of the substrate through simple instrumented indentation testing, it is important for a sufficient model that correctly predicts the behavior in a wide range of materials. One recent model developed by Zhou et al. has shown a more developed understanding of the interface between the substrate and film, and shows promise to better describe many material combinations, but has not been sufficiently vetted for films on substrates that more easily plastically deform. The focus of this work is to apply the aforementioned model to situations that it has not been before, and to evaluate its ability to accurately extract the film's Young's modulus and Poisson's ratio from the experimental composite modulus.

Acknowledgments

I would like to thank Dr. Prorok for his support and guidance throughout this process. I would like to thank my committee members, Dr. Overfelt and Dr. Jackson for their time and suggestions toward my thesis and research. I would also like to thank both the current and previous members of my group; Bo, Brandon, Nicole, Shakib, Madhu, Naveed and Dong as well as all of the other faculty, staff and students at Auburn University who have helped me during the course of my work; especially Jacob and Steve. I would like to thank my family for their love and unwavering support throughout my time at Auburn University, as always having you behind me has been a pillar of support that I have needed and will always be thankful for. And finally I would like to thank Brian for all of the early morning coffee and conversation throughout the years.

Table of Contents

Abstract ii

Acknowledgments iii

List of Tables vi

List of Figures vii

List of Abbreviations xii

Chapter 1: Introduction 1

1.1 Overview 1

1.2 Thesis Structure 2

Chapter 2: Literature Review of Instrumented Thin Film Indentation 3

2.1 Instrumented Indentation Testing 3

2.2 Continuous Stiffness Measurement 6

2.3 Erroneous Contact Area 8

2.4 Modeling Thin Film Substrate Effects 9

Chapter 3: Material Selection 18

3.1 Material Selection and Their Mechanical Properties 18

Chapter 4: Experimental Setup and Fabrication 20

4.1 Substrates 20

4.2 Film Deposition 26

4.3 Nanoindentation 37

Chapter 5: Results and Discussions 39

5.1 Experimental Nanoindentation Analysis 39

5.2 Validity of Zhou-Prorok Model in Investigated Materials 65

Chapter 6: Conclusions 71

References 72

List of Tables

Table 2.1.1 Geometries of different indenter tips; C-f = centerline to face angle, d = indentation depth, and a = tip radius for cone and spherical indenters. 4

Table 3.1.1 Material candidates for film and substrates with desirable Young's modulus and Poisson's ratio. Highlighted materials were chosen to be substrates or deposited as a film due to having the most favorable mechanical properties, being safe to work with and their availability. 19

Table 4.1.1 Spectrum analysis of energy-dispersive X-ray spectroscopy of indium substrate after polishing; all results in weight %. 22

Table 4.2.1 Sputtering parameters for Al film from Denton sputtering system log book. 27

Table 4.2.2 Sputtering conditions for Al films to evaluate how changing sputtering power influences Hillock grain formation and density. 30

Table 4.2.3 Sputtering conditions for Al films to evaluate how varying film thickness influences Hillock grain formation and density. 32

Table 4.2.4 Sputtering parameters of 230nm Pt film with Ti adhesion layer. 35

Table 4.2.5 Film thickness of sputtered platinum films..36

Table 5.1.1 Values of films' Young's moduli and alphas from Eq. (15) and (17) for each Pt film on substrate combination, as well each substrate's Young's Modulus obtained from nanoindenting directly into the substrate..51

List of Figures

Figure 2.1.1 Schematic of nanoindentation system. 3

Figure 2.1.2 (a) Load verses displacement plots for a typical, a relatively soft, and a relatively hard material. (b) Cross-sectional schematic of certain stages of the loading-unloading curve as shown in the typical load verses displacement plot.[9] 6

Figure 2.2.1 Load-Displacement curve during the continuous stiffness method. 7

Figure 2.2.2 Young's Modulus verses Displacement into surface for (a) bulk material, (b) compliant film on hard substrate and (c) hard film on compliant substrate.[11] 8

Figure 2.3.1 Schematics of the pile-up and sink-in effect. 9

Figure 2.4.1 Schematic of a indentation's cross section showing h, h_f, h_c, and h_s and how they relate to indention depth and elastic recovery after removal of load P.[13]...........................11

Figure 2.4.2 (a) Schematic illustrating the concept of continuous transfer of strain between the film and substrate, (b) simulation indicating that strain discontinuously transferred between the film and substrate, and (c) schematic showing how the film and substrate components are decoupled in the discontinuous elastic interface transfer model. 13

Figure 2.4.3 Finite element analysis of the AlOx film/substrate composites showing the elastic strain distribution for an indent penetrating 5nm into each film; (a) SiO_2, (b), Ge, (c) Si, (d) MgO, and (e) Sapphire. 16

Figure 2.4.4 Zhou et al. demonstrating that the film's modulus does not correspond to E_{flat} that their second model has the ability to accurately extract film modulus from the composite nanoindentation data. 17

Figure 4.1.1 Struers RotoPol-11 Surface Polisher. 21

Figure 4.1.2 JEOL JSM 7000F Scanning Electron Microscope. 21

Figure 4.1.3 Location of spectrums for energy-dispersive X-ray spectroscopy of indium substrate after polishing. 22

Figure 4.1.4 (a) Arbor press used to flatten both the indium and tin substrates for a smooth surface. (b) Illustration to show how force was evenly distributed across substrate surface.23

Figure 4.1.5 Micrographs at 1,000 magnification of In (a) 0.5mm surface as received, (b) 0.5mm thick In compressed, (c,d) 2mm thick In compressed 25

Figure 4.1.6 Micrographs at 1,000 magnification of Sn (a) 2mm surface as received, (b) 0.5mm thick Sn compressed, (c,d) 2mm thick Sn compressed 26

Figure 4.2.1 Denton Vacuum Inc. DC & RF sputtering system. 27

Figure 4.2.2 Tencor Instruments "Alpha-Step 200" profilometer. 28

Figure 4.2.3 Hillock growth grains on film surface of 400nm Al on SiO_2. 29

Figure 4.2.4 Micrographs of Al film surface as sputtered at different powers of 75, 125, 175, 300, 400, 600 and 700W at 10,000 magnifications. 31

Figure 4.2.5 Micrographs of Al film surfaces as sputtered to different thickness of 250, 500, 750 and 1000nm at 10,000 magnifications. 33

Figure 4.2.6 Micrographs of 250nm Al film on SiO2 at (a) 25x and (b) 1000x showing sporadic coverage. 34

Figure 4.2.7 Surface quality of platinum film on SiO2 substrate. 36

Figure 4.3.1 Image of MTS Nano Indenter XP nanoindentation system. 38

Figure 5.1.1 *E-h* curve of an example erroneous indention that would be deleted before averaging indentation results. 40

Figure 5.1.2 Checking validity of changing Poisson's ratio through Excel when compared to recalculating the sample through TestWorks. 41
Figure 5.1.3a *E-h* curve for In substrate after flattening with Arbor press. 42
Figure 5.1.3b *E-h* curve for Sn substrate after flattening with Arbor press. 43
Figure 5.1.3c *E-h* curve for Al single crystal substrate, orientation (100). 43
Figure 5.1.3d *E-h* curve for Cu single crystal substrate, orientation (100). 44
Figure 5.1.3e *E-h* curve for Ti substrate. 44
Figure 5.1.3f *E-h* curve for Pt substrate. 45
Figure 5.1.3g *E-h* curve for Ta substrate. 45
Figure 5.1.3h *E-h* curve for Si single crystal substrate, orientation (100). 46
Figure 5.1.4a *E-h* curve for 230nm Pt on In with Z-P model, film E and film alpha. 47
Figure 5.1.4b *E-h* curve for 230nm Pt on Sn with Z-P model, film E, and film alpha. 48
Figure 5.1.4c *E-h* curve for 230nm Pt on Al with Z-P model, D-N model, film E, and film alpha.48
Figure 5.1.4d *E-h* curve for 230nm Pt on Cu with Z-P model, film E, and film alpha. 49
Figure 5.1.4e *E-h* curve for 230nm Pt on Ti with Z-P model, D-N model, film E, and film alpha.49
Figure 5.1.4f *E-h* curve for 230nm Pt on Pt with Z-P model, film E, and film alpha 50
Figure 5.1.4g *E-h* curve for 230nm Pt on Ta with Z-P model, film E, and film alpha. 50
Figure 5.1.4h *E-h* curve for 230nm Pt on Si with Z-P model, D-N model, film E, and film alpha.51
Figure 5.1.5a 230nm Pt on In: 500nm indention 52
Figure 5.1.5b 230nm Pt on Sn: 500nm indention. 53
Figure 5.1.5c 230nm Pt on Al: 500nm indention...53
Figure 5.1.5d 230nm Pt on Cu: 500nm indention. 54
Figure 5.1.5e 230nm Pt on Ti: 500nm indention. 54

Figure 5.1.5f 230nm Pt on Pt: 500nm indention..55

Figure 5.1.5g 230nm Pt on Ta: 500nm indention. 55

Figure 5.1.5h 230nm Pt on Si: 500nm indention. 56

Figure 5.1.6 500nm indentions into 230nm Pt on Indium have a larger radius of volume than indicated by sharp edges shown in the 20,000 magnification. 57

Figure 5.1.7 Stiff film plastically deforming a larger area than typical in a softer substrate, causing the readily visible residual indention to be much smaller than if deformation was localized to under the tip. 58

Figure 5.1.7a Micrograph of 230nm Pt on In. Left: secondary e^-. Right: back-scattered e^-. 60

Figure 5.1.7b Micrograph of 230nm Pt on Sn. Left: secondary e^-. Right: back-scattered e^-.........60

Figure 5.1.7c Micrograph of 230nm Pt on Al. Left: secondary e^-. Right: back-scattered e^-. 61

Figure 5.1.7d Micrograph of 230nm Pt on Cu. Left: secondary e^-. Right: back-scattered e^-. 61

Figure 5.1.7e Micrograph of 230nm Pt on Ti. Left: secondary e^-. Right: back-scattered e^-..........62

Figure 5.1.7f Micrograph of 230nm Pt on Pt. Left: secondary e^-. Right: back-scattered e^-. 62

Figure 5.1.7g Micrograph of 230nm Pt on Ta. Left: secondary e^-. Right: back-scattered e^-.........63

Figure 5.1.7h Micrograph of 230nm Pt on Si. Left: secondary e^-. Right: back-scattered e^-..........63

Figure 5.1.8 EDS of 500nm indention into 230nm Pt on Si. a) Spectrum locations for b) Spectrum 1, c) Spectrum 2 and d) Spectrum 3. 64

Figure 5.2.1 E_{flat} plotted against E_s for all substrates as a means to suggest the Pt film's actual Young's modulus by where it crosses the line of plastic homogeneity indicated by the dashed line. 66

Figure 5.2.2 Plots of $\Delta Ef'$ verses the substrate modulus normalized by Ef'. 67

Figure 5.2.3 Micrograph of 230nm Pt on Si 500nm indention at a 70° tilt. 68

Figure 5.2.4 Micrograph of 230nm Pt on Al 500nm indention at a 70° tilt. 69

Figure 5.2.5 Micrograph of 230nm Pt on Ti 500nm indention at a 70° tilt. 69

Figure 5.2.6 Micrograph of 230nm Pt on Ta 500nm indention at a 70° tilt. 70

List of Abbreviations

E	Composite Young’s Modulus
DC	Direct Current
RF	Radio Frequency
D-N	In relation to Doerner and Nix Model
O-P	In relation to Oliver and Pharr Model
H-C	In relation to Hay and Crawford Model
Z-P	In relation to Zhou and Prorok Model
S-N	In relation to Saha and Nix Model
f	As subscript: of the film
i	As subscript: of the indenter
Å	Angstrom
nm	Nanometer
φ	Weighting factor
s	As subscript: of the substrate
μ	Shear Modulus
v	Poisson’s Ratio
SEM	Scanning Electron Microscope
CSM	Continuous Stiffness Method
MEMS	Microelectromechanical systems

Chapter 1: Introduction

1.1 Overview

Indentations of materials on a macro and micro scale have been a cornerstone of determining mechanical properties, such as hardness, of materials for the last century. During indentation, a tip with known geometric size and mechanical properties is pressed into a material. Once loading is complete, the hardness of the indented material is then calculated from the maximum load applied and the measured contact area from the remaining indent. As the experimentation method has progressed, there has been a desire to make smaller and less intrusive indents on smaller and smaller scales. Over the last few decades instrumented indentation on the nano-scale, nanoindentation, has gained attention as a method to extract the hardness and Young's modulus of a samples that require higher precision and much lower loads that can be applied by direct human interaction.

With nanoindentation came the possibility to indent on a sample that consists of a thin layer, or film, of one material on the surface of a different bulk material, or substrate. The interest in thin films comes from their use in a wide range of material applications such as optical coatings, very large-scale integrated circuits, anti-corrosion, anti-wear and fuel cells. Even when the applications are not centered on the mechanical behavior of the thin films, increasing their ability to withstand processing, and durability during their lifetime is still needed. One current shortcoming of nanoindenting thin films being widely researched is that as the film's thickness decreases, the substrate starts to play more of a role in the properties determined through indentation, even at very low penetration depths of the film. Recent authors[1-7] have developed theoretical models based on both experimental and finite element analysis that attempt to extract

the mechanical properties of the film, independent of the substrate. While all of these models have their strengths, they also tend to only work for certain material combinations; such as compliant films on hard substrates, or hard films on compliant substrates.

The goal of this research is to thoroughly review one of the more recent models to of been developed that takes a new approach in describing the film and substrates composite behavior. This model, developed by Zhou et al. takes into account that the transfer of energy across the film-substrate interface is not linear, but actually discontinuous; allowing it to better describe the film's behavior for a broader range of material combinations. A group of materials were selected for their similar Poisson's ratio, but varying Young's modulus, to have a single thin film layer sputtered on them which also has a similar Poisson's ratio to the substrates. The samples were then nanoindented, comparing the Young's modulus verses indention depth to the behavior expected through the evaluated model.

1.2 Thesis Structure

Chapter 2 includes a literature review of instrumented indentation testing, and looks at each of the major models that have been developed to extract the film's intrinsic mechanical values. Chapter 3 discusses the method and line of thought throughout the process of material selection for both the film and substrates used in terms of which mechanical properties were desired, and why. Chapter 4 details the experimental setup of how the substrates were prepared, the parameters used for thin film deposition, and characterization of the resulting composite film-substrate samples through SEM and nanoindentation. Chapter 5 and 6 present the results, a discussion of their meaning, and a summary of the research.

Chapter 2: Literature Review of Instrumented Thin Film Indentation

2.1 Instrumented Indentation Testing

Instrumented Indentation Testing, or nanoindentation, is applying a measurable load on a sample through a tip of known geometry and mechanical properties, and then measuring the material's response as the tip is withdrawn as well as the load required to displace the tip into the sample. While there are a range of commercial available indentation systems that use their own methodology, a schematic of one of the most common implementations is shown in Figure 2.1.1; a magnet and coil in an induction force generation system to generate load, with the displacement being measured through a capacitance displacement gauge.[8]

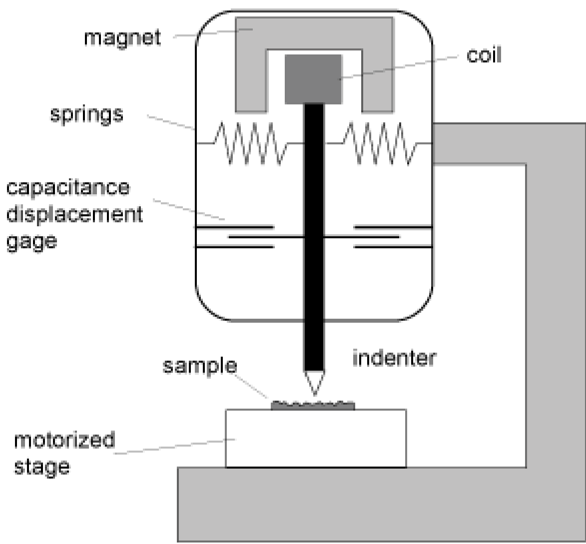

Figure 2.1.1 Schematic of nanoindentation system.[8]

There are a range of indentation tips that can be utilized, each having their own area of purpose, and associated advantages and disadvantages. The most commonly used tips for

indentation are spherical and Berkovich, a three sided pyramidal shape. While conical tips are self-similar, meaning they have the same geometric relationship through a range of depths, and are good for defining mechanical properties, sufficiently hard specimens are increasing hard to manufacture at smaller scales. The Berkovich tip also allows for a self-similar shape at increasing indent depth, but is able to be fabricated to an extremely sharp point through traditional grinding techniques on only three sides; making it the most commonly used indenter due to its low production costs. A selection of available tips and their associated geometries are given in Table 2.1.1.[9]

Table 2.1.1 Geometries of different indenter tips; C-f = centerline to face angle, d = indentation depth, and a = tip radius for cone and spherical indenters.[9]

Parameter	Berkovich	Cube-corner	Cone	Spherical	Vickers
Shape					
C-f angle	65.35°	35.264°	—	—	68°
Projected Contact area	$24.5600d^2$	$2.5981d^2$	πa^2	πa^2	$24.5044d^2$

Once the tip penetrates the surface of the sample, the deformation that occurs has both elastic and plastic components. These two components are intertwined until the tip is unloaded, at which point only the elastic behavior is causing a force that pushes back on the tip as it moves out of the material. As this mechanism is isolated from plasticity, the measured slope of the unloading curve is used to determine how elastic the material is. The more stiff the material, the more energy that is able to be stored elastically between atoms, which is then applied back to the tip during unload; leading to an unloading curve that more closely follows the path of the loading

curve. Consequently, the less stiff the material, the more vertical the unloading curve is, as the energy has been dispersed as plastic behavior so there is less stored energy to be transferred back to the tip. Load verses displacement plots for typical, soft, and hard materials are given in Figure 2.1.2(a), and the resulting sample's responses at different points are shown in Figure 2.1.2(b).[9] This unloading stiffness, *S*, can be related to Young's modulus, *E*, of the material through the equation

$$S = \frac{dP}{dh} = \frac{2}{\sqrt{\pi}} E_r \sqrt{A} \tag{1}$$

where *dP* is the change in load, *dh* is the change in displacement, *A* is the contact area, and E_r is the effective modulus determined by

$$\frac{1}{E_r} = \frac{(1-v^2)}{E} + \frac{(1-v_i^2)}{E_i} \tag{2}$$

where *E* and E_i are the elastic moduli of the sample and indenter respectively, while *v* and v_i are the Poisson's ratio of the sample and indenter tip.[9]

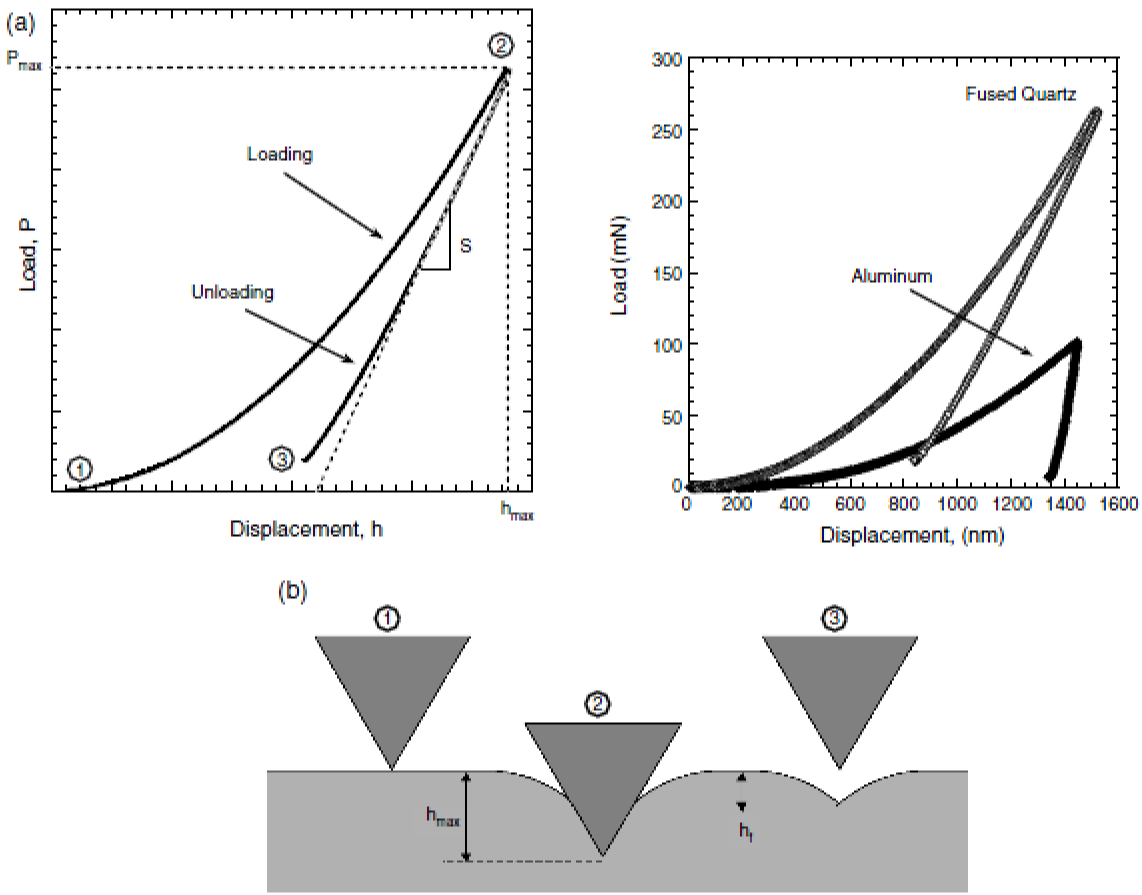

Figure 2.1.2 (a) Load verses displacement plots for a typical, a relatively soft, and a relatively hard material. (b) Cross-sectional schematic of certain stages of the loading-unloading curve as shown in the typical load verses displacement plot.[9]

2.2 Continuous Stiffness Measurement

With thin films comes the desire to be able to show the Young's modulus or hardness verses the indention depth into the sample as this allows for the separation of film and substrate properties. A method used to accomplish this is the continuous stiffness method, or CSM. Also known as the dynamic stiffness measurement, CSM applies an oscillatory force to the increasing load of a standard instrumented indentation test. Shown in Figure 2.2.1 the oscillation of the load allows for the stiffness to be measured at many points as displacement increases.

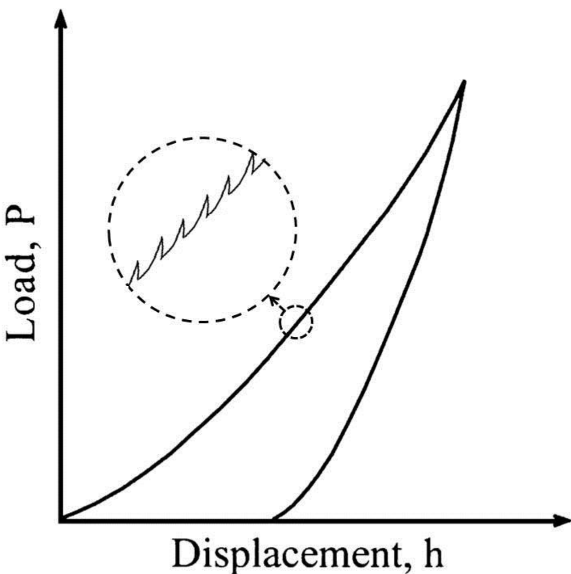

Figure 2.2.1 Load-Displacement curve during the continuous stiffness method.[10]

In the case of thin film nanoindentation, the advantage of CSM is the ability to the show mechanical properties for a range of displacement, not one set depth per indention, as it is with typical indentation methods. At the earlier stage of the indention, the returned mechanical properties are mostly comprised of the thin film, and as the tip moves deeper into the film, the substrate's effect starts to take over, eventually coming to dominate as the depth approaches, and surpasses, the thickness of the film. If a bulk material is indented using CSM, the resulting Young's modulus verses displacement plot will show a constant horizontal line, as the property of the material would not change with depth. Indenting a sample that is composed of a soft, or compliant, film on a hard substrate, the Young's modulus will start near the value of the film's material in bulk, and rise toward that of the substrate. When indenting a hard film on a compliant substrate the modulus-displacement curve starts near the value of the film and has a

negative trending slope as you move deeper into the sample. Summaries of each of these different occasions are given in Figure 2.2.2.

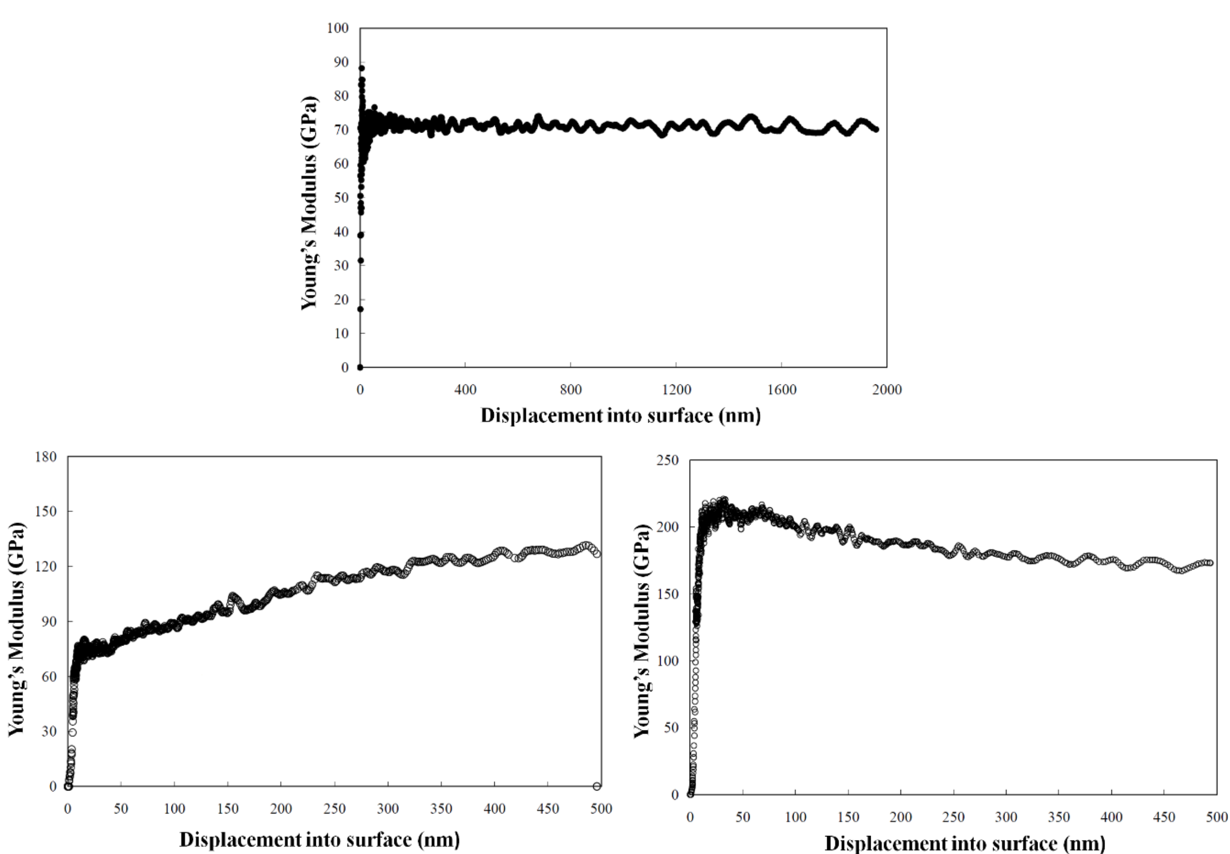

Figure 2.2.2 Young's Modulus verses Displacement into surface for (a) bulk material, (b) compliant film on hard substrate and (c) hard film on compliant substrate.[11]

2.3 Erroneous Contact Area

One substantial challenge to nanoindentation is the difficulty in accurately measuring the contact area during displacement, due to how the material being indented can plastically deform around the indenter, causing a change in actual contact area between the sample and tip, also known as erroneous contact area. If the material is soft it will tend to pile-up around the indenter tip, causing an increase in contact area, leading to an overestimation of the material's modulus,

and hardness, as there is more material providing elastic recovery. Harder materials have the tendency to translate their strain further away from the tip, allowing for a greater volume of material to distribute the deformation, causing the area around the tip to sink-in, reducing the contact area of the tip. The sink-in effect leads to an underestimation of the material's modulus, and hardness. A cross sectional schematic of both effects during indentation, and the resulting top-down view of the recovered material after unload is shown in Figure 2.3.1.[12]

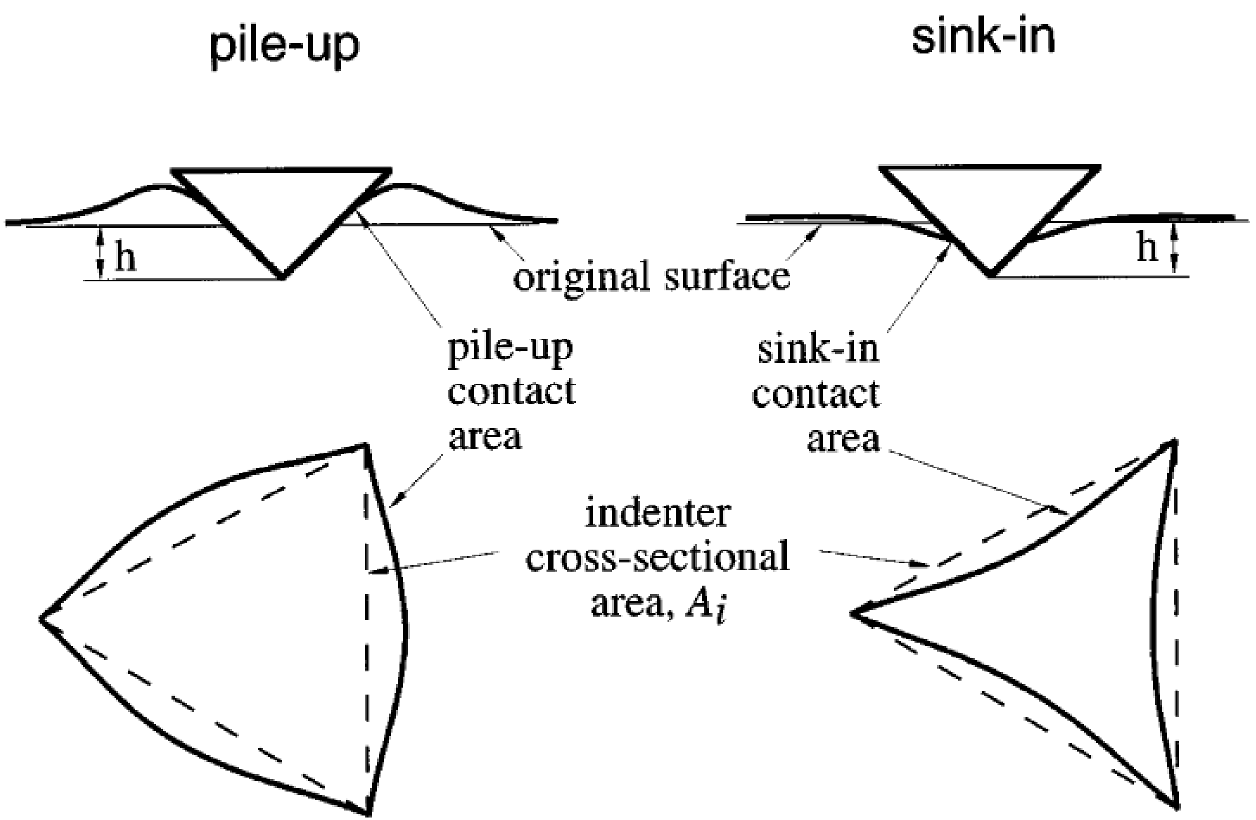

Figure 2.3.1 Schematics of the pile-up and sink-in effect.[12]

2.4 Modeling Thin Film Substrate Effects

As instrumented indentation has approached the nanoscale, a new issue has appeared that has been an area of research is how the mechanical properties of the substrate influence the

experimental indentation data, even at very shallow depth. As the field of nanoindentation has continued to develop, a range of approaches have developed different models that attempt to extract the film's properties independent of the substrate.[1, 2, 5, 7, 13, 14] While some of these models better describe certain material combinations, the goal is to have a model that describes the majority of film-substrate material combinations with a wide range of mechanical behavior.

Not satisfied with the underlying assumption that the unloading load-displacement curve is linear, Oliver and Pharr showed that for most materials the unloading curve relates to stiffness through a power law function

$$P = B\left(h - h_f\right)^m \tag{3}$$

where B and m are empirically determined constants and h_f is final displacement after the material is allowed to elastically recover.[13]

With the stiffness data, S, the reduced Young's modulus and hardness, E_r and H respectively can be calculated from

$$E_r = \frac{\sqrt{\pi}}{2}\frac{S}{\sqrt{A}} \tag{4}$$

and

$$H = \frac{P}{A} \tag{5}$$

where A is the projected contact area at peak load and is a function of h_c, the vertical distance along which contact is made, in the form $A = f(h_c)$. A schematic cross section of an indent before and after elastic recovery to show the related different depths is shown in Figure 2.4.1. For a perfect Berkovich tip, A is calculated as

$$A = 24.5h_c^2 \tag{6}$$

but in practice as a perfect tip cannot be obtained, another relationship

$$A = 24.5h_c^2 + C_1 h_c^1 + C_2 h_c^{1/2} + C_3 h_c^{1/4} + \ldots\ldots + C_8 h_c^{1/128} \quad (7)$$

can be used where C_1 through C_8 are constants. The lead term describes a perfect Berkovich tip, with the following terms representing changes to the tip's geometry due to blunting. The Oliver and Pharr method to calculate mechanical properties from instrumented indention testing is currently the most common used in practice.

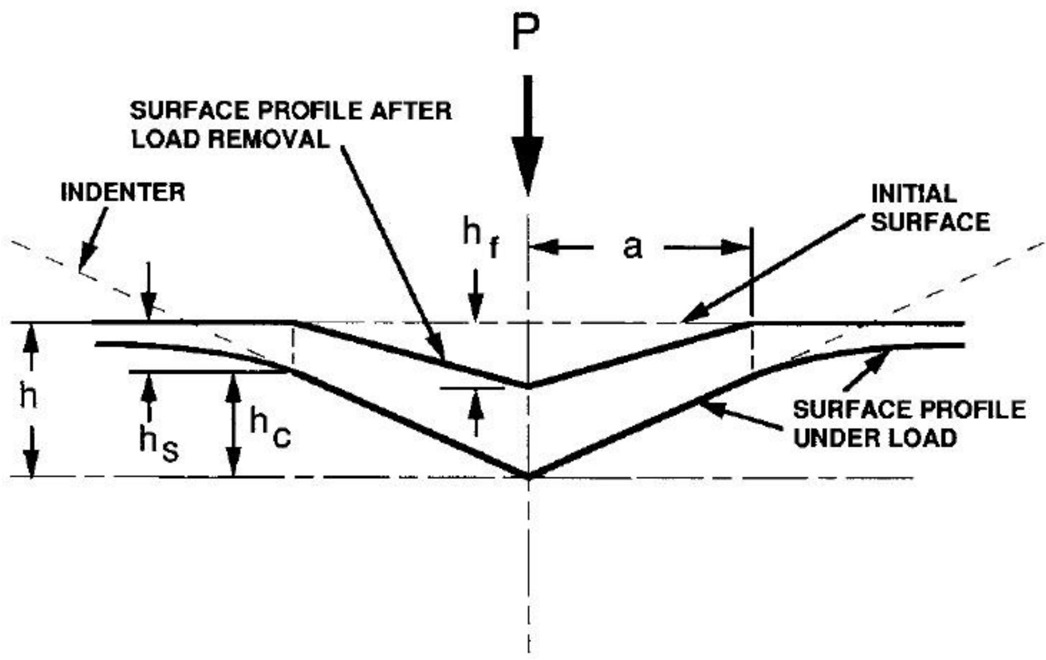

Figure 2.4.1 Schematic of a indentation's cross section showing h, h_f, h_c, and h_s and how they relate to indention depth and elastic recovery after removal of load P.[13]

Doerner and Nix were the first to develop a model that allowed for the determination of the film’s modulus from the substrate affected Young’s modulus.[1] In the Doerner-Nix model there is a continuous transfer of energy through the film-substrate boundary, meaning that the values of strain were equivalent on both sides of the interface, as shown in Figure 2.4.2(a). This

continuous transfer of energy through to the substrate allowed for a single weighting factor to be used in their model,

$$\frac{1}{E'} = \frac{1}{E'_f} + \left(\frac{1}{E'_s} - \frac{1}{E'_f}\right)\varphi_{D-N} \tag{8}$$

where, E' is the composite modulus, $E'_f = E_f/(1 - v_f^2)$, $E'_s = E_s/(1 - v_s^2)$, and φ_{D-N} is the Doerner-Nix weighting factor. φ_{D-N} accounts for the increasing contribution of the substrate to the composite modulus as the indenter moves deeper into the sample, and is given as,

$$\varphi_{D-N} = e^{-\alpha(t/h_{eff})} \tag{9}$$

where, t is the film's thickness, h_{eff} is the effective indentation depth, and α is the empirically determined constant suggested as 0.25 for most materials.

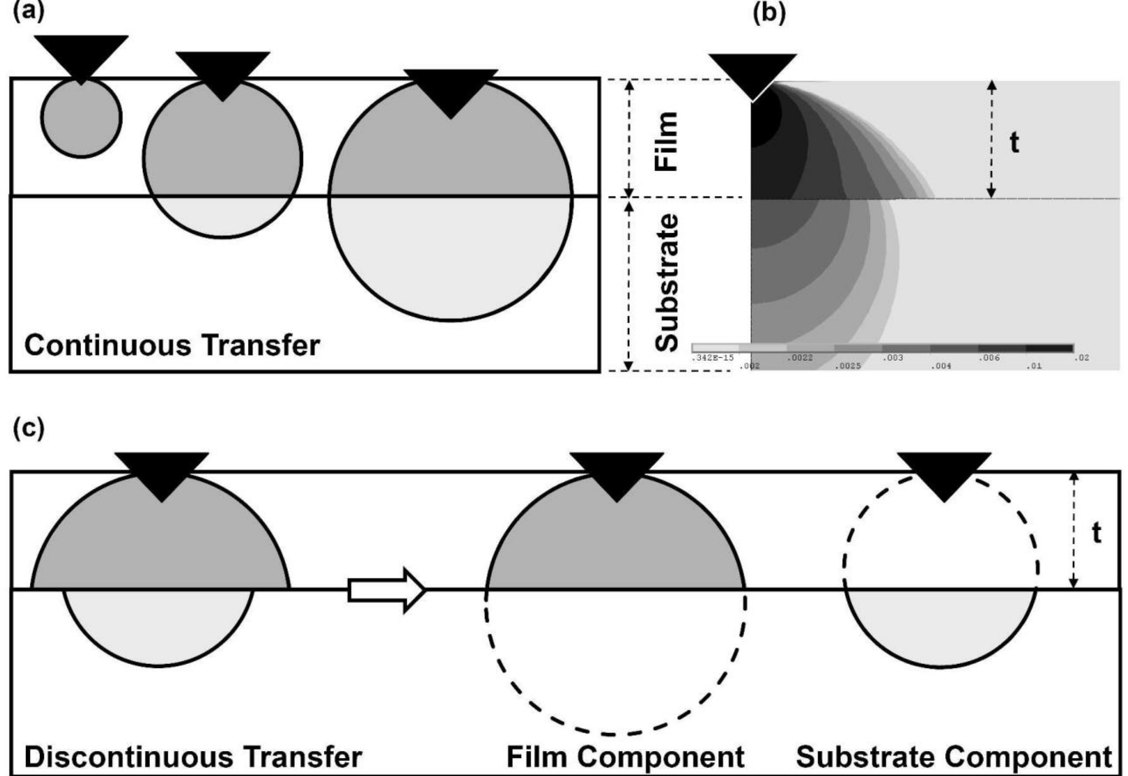

Figure 2.4.2 (a) Schematic illustrating the concept of continuous transfer of strain between the film and substrate, (b) simulation indicating that strain discontinuously transferred between the film and substrate, and (c) schematic showing how the film and substrate components are decoupled in the discontinuous elastic interface transfer model.[7]

Modifying the Doerner and Nix model to work with a wider variety of substrate-film combinations, King et al. used numerical evaluation of a flat triangular punch to extend Eq. (8) and (9) to

$$\frac{1}{E_r} = \frac{1-\nu_i^2}{E_i} + \frac{1-\nu_f^2}{E_f}\left(1 - e^{-\frac{\alpha t}{a}}\right) + \frac{1-\nu_s^2}{E_s}\left(e^{-\frac{\alpha t}{a}}\right) \tag{10}$$

where a is the square root of the projected contact area, t is the thickness of the film, and α is a scaling parameter that differs for different tip geometries, as it is a function of the normalized

punch size.[3] This new equation allows for a term that is able to describe the substrate effect and extract the intrinsic film modulus, an attribute missing from the Doerner & Nix model.

Saha and Nix then made an effort to alter King model so that it allow for a Berkovich type indenter's geometry.[5] To do this they imagined that a flat punch was situated at the tip of the Berkovich indenter changing the effective film thickness, *t*, to be realized as *t-h*, where h is the total indenter displacement. Substituting t-h for t in Eq. (10) leads to

$$\frac{1}{E_r} = \frac{1-\nu_i^2}{E_i} + \frac{1-\nu_f^2}{E_f}\left(1 - e^{-\frac{\alpha(t-h)}{a}}\right) + \frac{1-\nu_s^2}{E_s}\left(e^{-\frac{\alpha(t-h)}{a}}\right). \quad (11)$$

As α is a function of *a/t*, which of course also change with indenter geometry, it was also taken into consideration and extrapolated to larger ratios of *a/t*. With the modified version of King's model, Saha and Nix plotted E_f against displacement for several films of varying thickness; showing a reasonable match to the expected film modulus for indentions up to 50% of the film's thickness.

Building upon the Song-Pharr model, the Hay-Crawford model better represents stiff films on compliant substrates.[2, 14] The Song-Pharr model assumes a column of the sample material; film and substrate, under the indenter as isolated from the surrounding material allowing it to be treated as springs in series; one for the film and one for the substrate. The shear modulus of each spring is then weighted according to the tip's contact area and film's effective thickness through the transition function I_0. Hay's method takes into consideration an inherent problem of all models that treat the film and substrate as springs in series; that the material under the indenter cannot be isolated from the surrounding material, especially with stiff films, as there is a quite a bit of lateral support.

The Hay-Crawford model proposes to let the film also act as a spring in parallel with the substrate, not just in series. Having the film also behave as if in parallel allows for the consideration of several mechanisms. First, as the film becomes stiff, it dominates the response of the material. Second, as the film becomes thin and stiff, the deformation in the top layer of the substrate approaches that of the film; coinciding with two different stiffness springs acting in parallel when they experience equal deformation. Third, when there is significant lateral support from the film then it behaves as the leaf springs that support the indenter column, which are well modeled by a parallel spring. As parallel springs are treated by adding their stiffness, Hay's model is derived as:

$$\frac{1}{\mu_a} = (1 - I_0)\frac{1}{\mu_s + F I_0 \mu_f} + I_0 \frac{1}{\mu_f} \tag{12}$$

Where μ_a, μ_s and μ_f are the apparent, substrate and film shear modulus respectively, I_0 is the aforementioned Gao weighting factor, and F is a dimensionless constant used to moderate the influence of the film modulus; by finite-element analysis, F was determined to have the constant value 0.0626. The shear modulus of the film is then calculated from the apparent value, which is then used along with the Poisson's ratio to calculate the elastic modulus of the film.

Figure 2.4.3 illustrates that how through finite element analysis Zhou and Prorok showed that the transfer of strain between the film and substrate were not continuous, but instead discontinuous.[6] Building upon Doerner-Nix, the Zhou-Prorok model allows for two weighting factors to account for the film and the substrate individually and is given as,

$$\frac{1}{E'} = \frac{1}{E'_f}(1 - \varphi_s) + \frac{1}{E'_s}\varphi_f \tag{13}$$

where,

$$\varphi_f = e^{-\alpha_f (t/h)} \text{ and } \varphi_s = e^{-\alpha_s (t/h)} \tag{14}$$

Here φ_f and φ_s are the aforementioned weighting factors, with their physical meaning illustrated in Figure 2.4.2(b,c); α_f and α_s are the Poisson's ratio of each the film and substrate respectively.

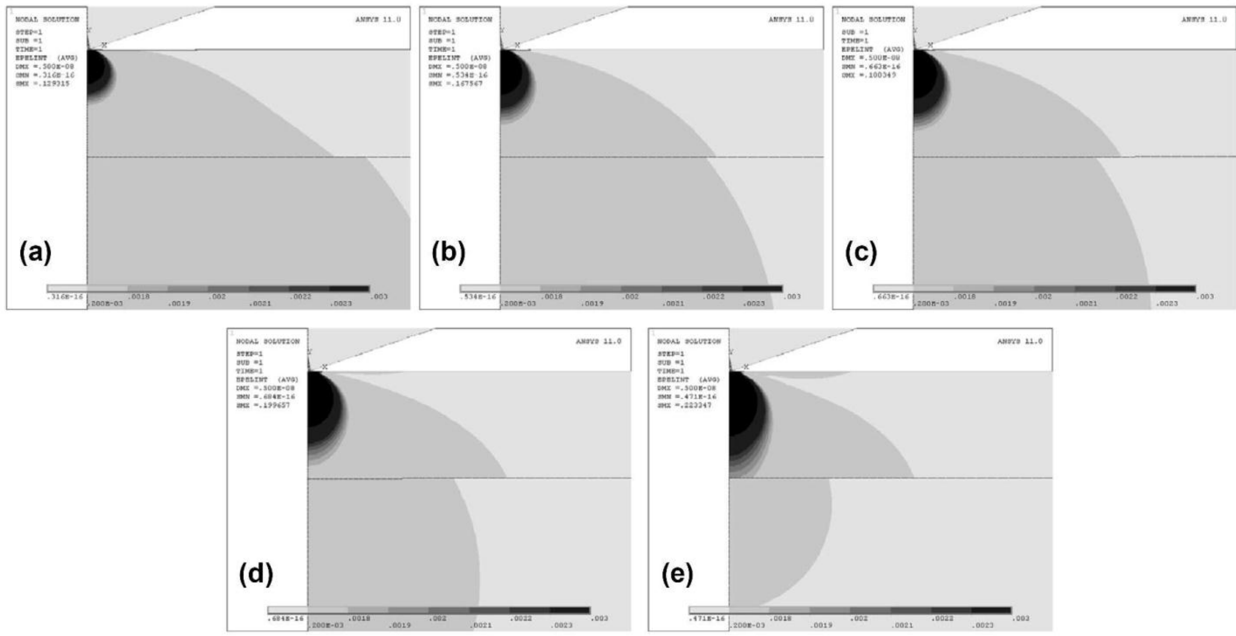

Figure 2.4.3 Finite element analysis of the AlOx film/substrate composites showing the elastic strain distribution for an indent penetrating 5nm into each film; (a) SiO_2, (b), Ge, (c) Si, (d) MgO, and (e) Sapphire.

The Zhou-Prorok model was further investigated for a wide variety of film, substrate combinations and Zhou et al. noted that the flat regions seen at shallow indents were not purely representative of the film alone and still had an influence from the substrate.[7] Through application of a power law function to their model they were able to reliably extract the film's Young's modulus independent of indenter penetration through the equation

$$\frac{1}{E'} = \frac{1}{E'_f}(1-\varphi_s)\left(\frac{E'_f}{E'_s}\right)^{0.1} + \frac{1}{E'_s}\varphi_f \tag{15}$$

employing the standard Oliver and Pharr method. With this new model they were able to accurately extract the film's Young's modulus as determined through membrane deflection experiment, or MDE, demonstrated in Figure 2.4.4.

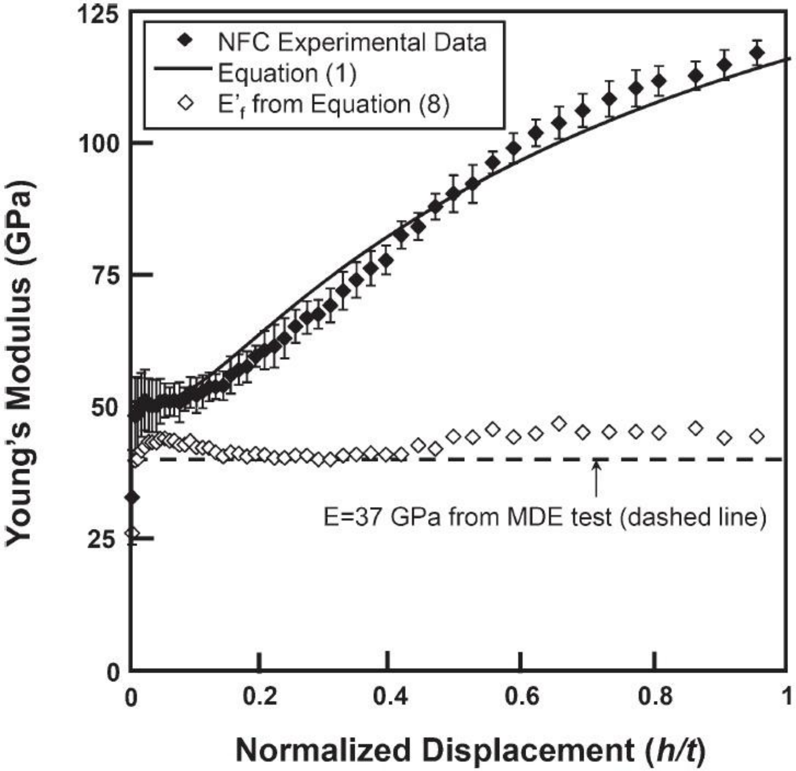

Figure 2.4.4 Zhou et al. demonstrating that the film's modulus does not correspond to E_{flat} that their second model has the ability to accurately extract film modulus from the composite nanoindentation data.

Chapter 3: Material Selection

3.1 Material Selection and Their Mechanical Properties

To explore the effects of the differences between the film and substrate's Young's modulus on the composite modulus and how it relates to errant contact area, a range of substrates were investigated that had equivalent Poisson's ratio, but different Young's modulus. The films used not only needed to have a Poisson's ratio that was near the substrates', but also have a mid-range Young's modulus in order to facilitate substrates with both a lower and higher Young's modulus. As possibly creating sink-in with a soft film that usually exhibits pile-up behavior, the film's modulus was kept in the lower portion of mid-range, specifically 70 to 90GPa. Beyond their mechanical behavior, the materials must be available for purchase and safe to work with as they would be mechanically polished and exposed to a range of temperatures during film deposition. A list of possible candidate materials first looked at for both the film and substrates are given in Table 3.1.1. Aluminum and platinum were chosen as film candidates while In, Sn, Al, Ag, Cu, Pt and Ta were chosen for substrates as all of these materials have a Poisson's ratio near 0.35, with Young's moduli ranging from 11 to 186GPa. Si was also added to the substrates as its mechanical behavior is widely known, and can serve as a substrate that does not plastically deform; a baseline to connect with the samples used in the creation of the Zhou-Prorok model. While In has a Poisson's ratio a bit higher than the rest at 0.44, it was included as it has an extremely low Young's modulus in comparison to Al and Pt.

Table 3.1.1 Material candidates for film and substrates with desirable Young's modulus and Poisson's ratio. Highlighted materials were chosen to be substrates or deposited as a film due to having the most favorable mechanical properties, being safe to work with and their availability.

Films			**Substrates**			
Material	**E (GPa)**	**ν**	**Material**	**E (GPa)**	**ν**	**References**
Au	72	0.44	Se	10	0.33	
Al	70	0.35	In	11	0.44	
Ag	83	0.37	Mg	45	0.35	[15]
Pt	168	0.36	Sn	50	0.36	
			Cd	50	0.30	[15]
			Al (100)	63-70	0.35	[13, 15, 16]
			SiO_2	72	0.18	[11, 13, 15]
			Au	78	0.44	[15]
			Ag	83	0.37	[15]
			Zr	88	0.34	
			Nb	105	0.40	[15]
			Ti	116	0.32	[15]
			Cu (100)	66.7-117	0.35	[15]
			Pd	121	0.39	
			Pt	168	0.36	[17-19]
			Si	178	0.28	[9, 11, 13, 15, 20]
			Ta	186	0.34	[15]
			Ni	200	0.31	[15]
			Co	209	0.31	
			Mo	329	0.31	
			Re	463	0.30	

Chapter 4: Experimental Setup and Fabrication

4.1 Substrates

Unpolished metallic substrates of copper, aluminum, silver, tin, tantalum, platinum, titanium, and indium of 0.5mm thick and 25x25mm or larger and at least 99.99% pure were obtained from Alfa Aesar, Ward Hill, MA. The substrates were then cut into smaller pieces using a Dremel rotary tool as opposed to shearing as to reduce bending and the resulting microstructural changes and internal stresses. Once they were in 5 to 10mm squares, they were first rough polished using ANSI 2000 grit abrasive disc, and then polished to a mirror finish using 0.5μm, then 0.05μm alumina particle suspension with a Struers RotoPol-11 (Ballerup, Denmark), Figure 4.1.1. Scanning Electron Micrographs obtained using a JEOL JSM 7000F (Tokyo, Japan), shown in Figure 4.1.2, indicated that the majority of substrates, specifically the softer materials of In, Sn, Al, and Cu had particles imbedded into their surface. Figure 4.1.3 and Table 4.1.1 display the results of energy-dispersive X-ray spectroscopy, or EDS, that was performed on the In substrate to identify that the particles present were contaminates, AlOx and Si, from the polishing process.

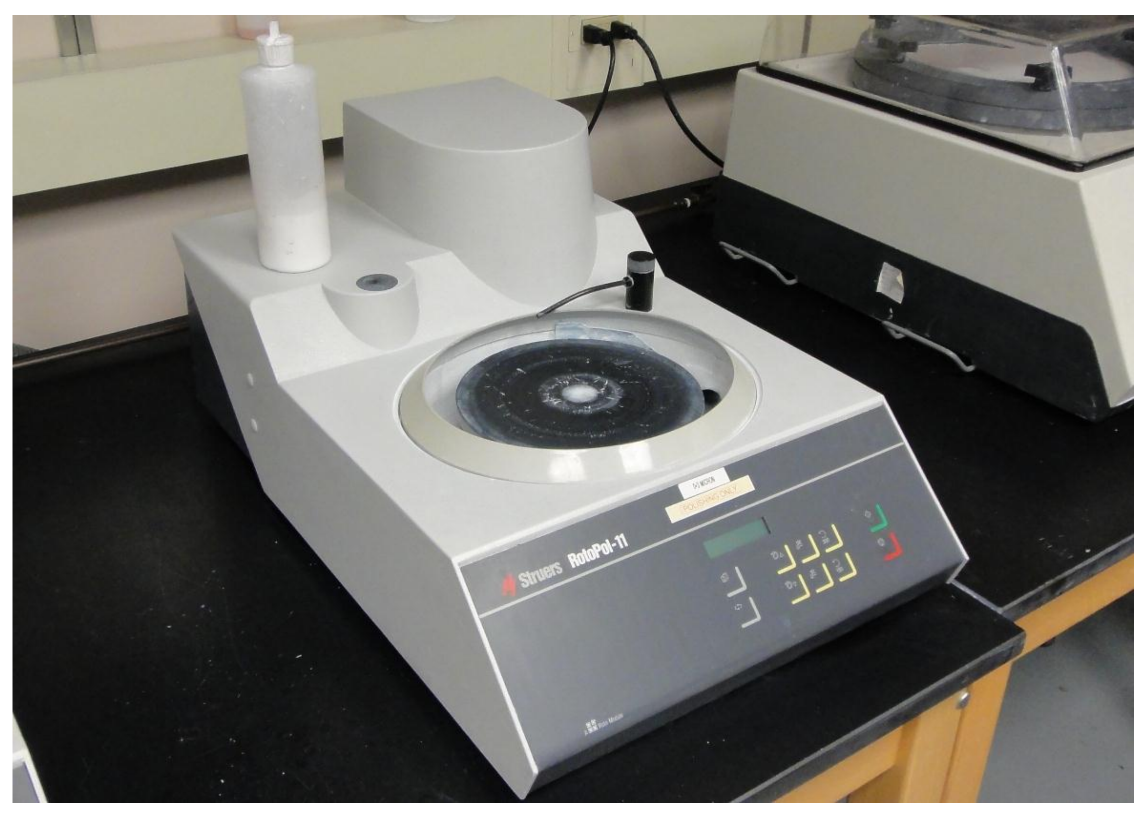

Figure 4.1.1 Struers RotoPol-11 Surface Polisher.

Figure 4.1.2 JEOL JSM 7000F Scanning Electron Microscope.

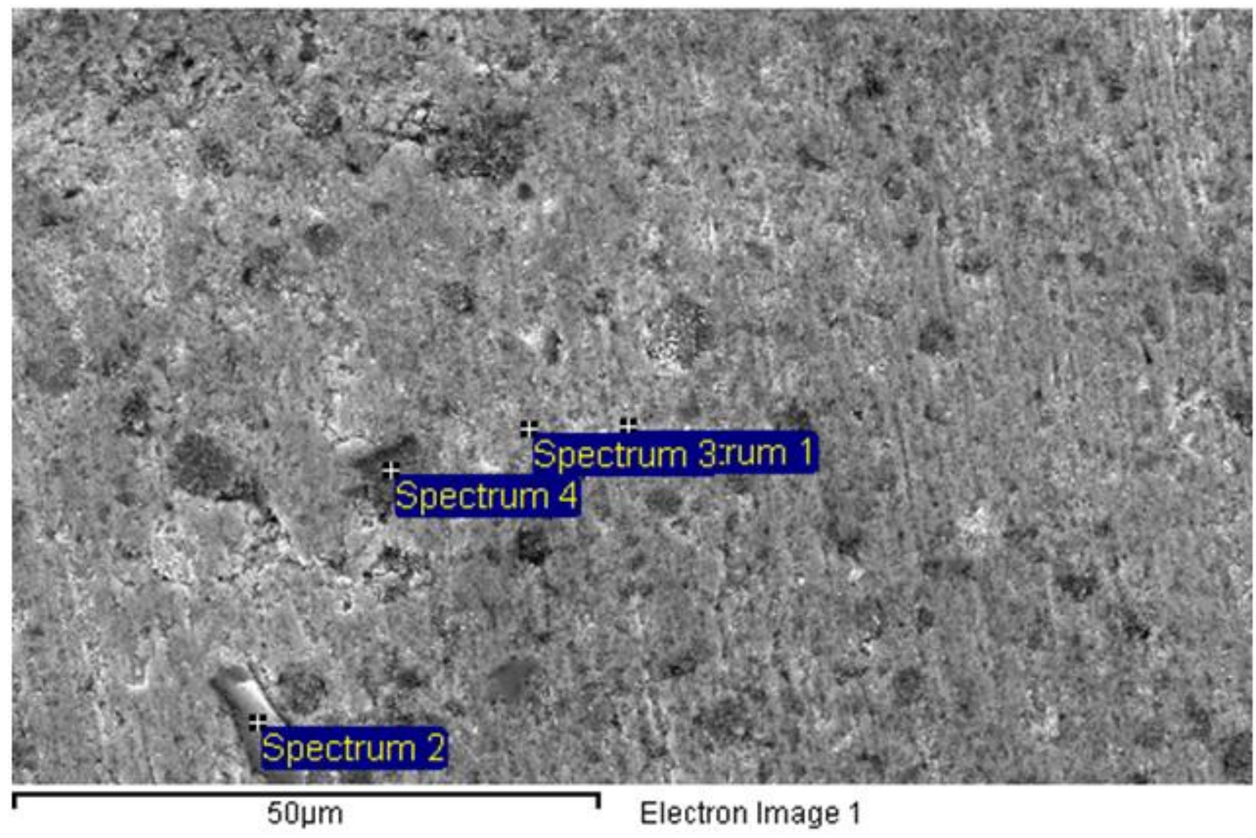

Figure 4.1.3 Location of spectrums for energy-dispersive X-ray spectroscopy of indium substrate after polishing.

Table 4.1.1 Spectrum analysis of energy-dispersive X-ray spectroscopy of indium substrate after polishing; all results in weight %.

Spectrum #	**O**	**Al**	**Si**	**In**	**Total**
1	51.40	34.97		13.63	100.00
2			100.00		100.00
3		4.75		95.25	100.00
4	51.72	42.39		5.89	100.00

To obtain these softer substrates with a mirror polish, <100> orientation single crystal substrates of aluminum and copper pre-polished by means of chemical-mechanical planarization to less than 100Å roughness, were ordered from MTI Corporation (Richmond, CA). No readily

available polished substrates were found for the softest of the materials, indium and tin. In order to create substrates of indium and tin with a smooth surface, they were mechanically flattened using pressure applied to their surface using an arbor press shown in Figure 4.1.4(a). Aluminum pucks were used to distribute the force evenly across a polished sapphire substrate as illustrated in Figure 4.1.4(b), in order to maintain a smooth and uniform surface across the entire substrate.

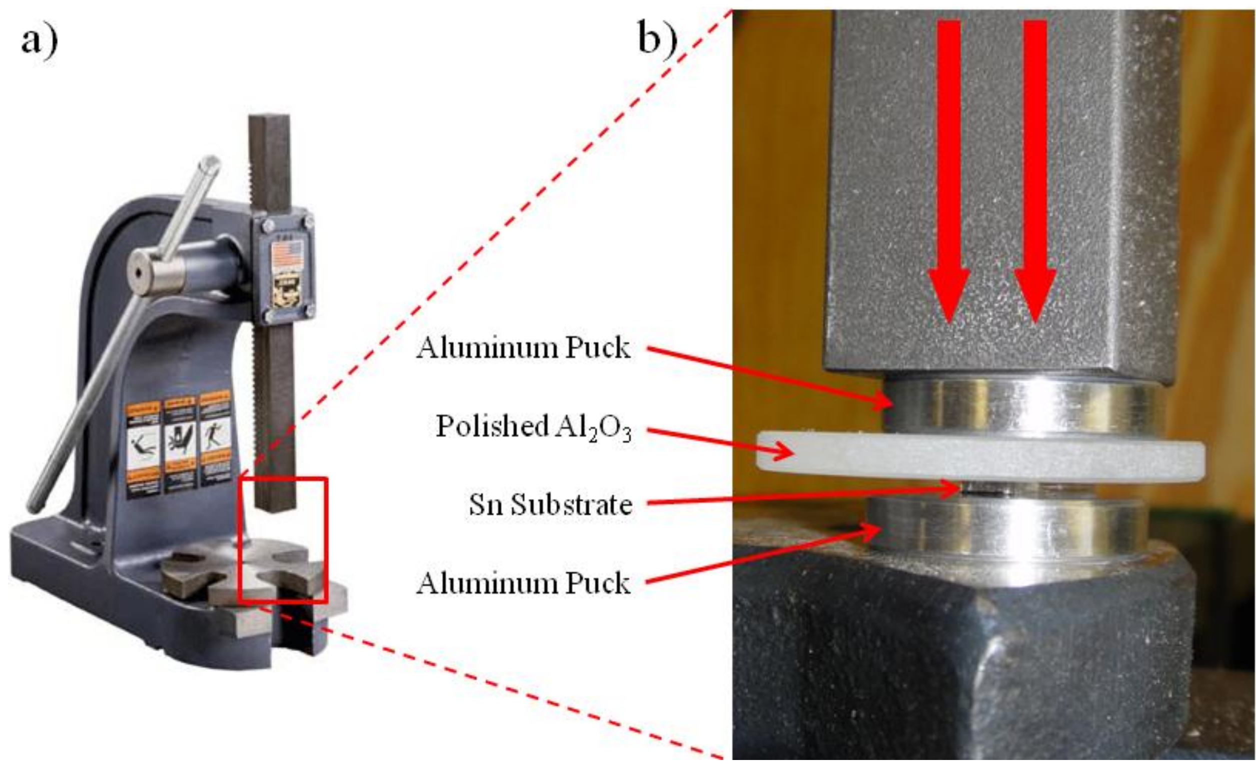

Figure 4.1.4 (a) Arbor press used to flatten both the indium and tin substrates for a smooth surface. (b) Illustration to show how force was evenly distributed across substrate surface.

At first, the results from using the arbor press were varied, and while the pressed substrates showed an improved flatness, they were still not suitable for film deposition and then nanoindentation. The first attempt at flattening an indium sample resulted in what appeared to be a very smooth surface, but the sample was compressed into a foil no more than 150um thick

which is not enough to ensure that during nanoindentation there is zero influence from the aluminum puck or bonding used to attach the substrate to the puck. From this mistake, and the following attempts' inability to be smooth while maintaining a sufficient thickness, came the realization that if a substrate of original thickness of 2mm or more is compressed, it will allow for a larger degree of plastic deformation which will allow for a flatter surface. To that end, 2mm thick indium and tin substrates were ordered. These were then cut into 3 or 4mm squares and flattened through the same method as before. SEM micrograph comparisons of the surfaces before being compressed and after the various attempts to make a smoother surface for In are shown in Figure 4.1.5, and in Figure 4.1.6 for Sn.

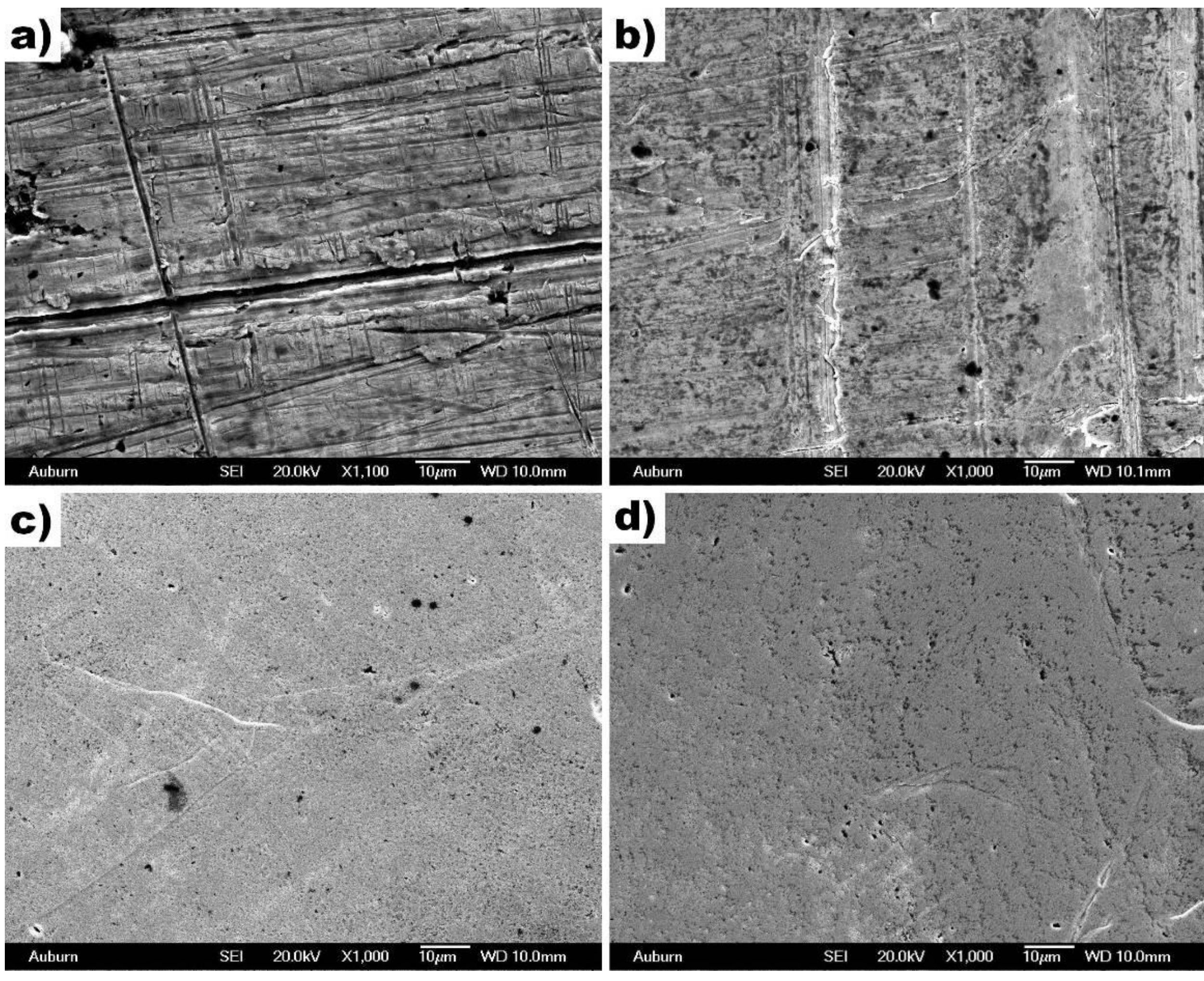

Figure 4.1.5 Micrographs at 1,000 magnification of In (a) 0.5mm surface as received, (b) 0.5mm thick In compressed, (c,d) 2mm thick In compressed.

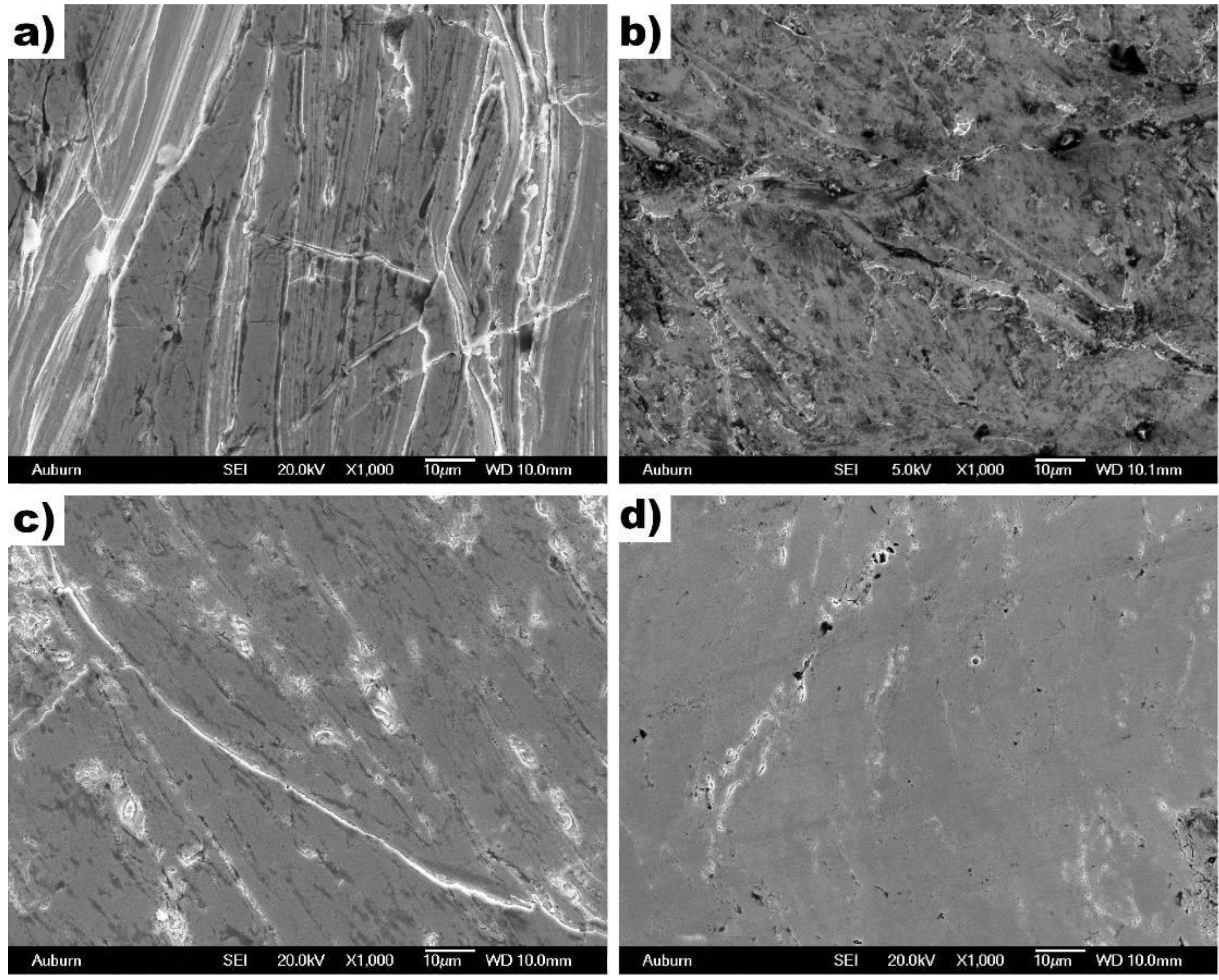

Figure 4.1.6 Micrographs at 1,000 magnification of Sn (a) 2mm surface as received, (b) 0.5mm thick Sn compressed, (c,d) 2mm thick Sn compressed.

4.2 Film Deposition

Once the substrates were in order, a thin film of aluminum was to be deposited using a Denton Vacuum Inc. DC & RF magnetron sputtering system, shown in Figure 4.2.1. When depositing films for thin film nanoindentation it is crucial that the films are of uniform quality in terms of surface roughness and depth. To measure the quality of film deposited, the aluminum was first sputtered onto a cleaned fused silica microscope slide, or SiO_2. The parameters initially

used were extracted from the sputtering system's log book, recorded when aluminum was previously sputtered by other users when running this system as shown in Table 4.2.1. From these values it was chosen to go with a sputtering power of 200 watts as it was used for the film that most closely resembles the desired thickness of 500nm. To compensate for the original film being 400nm, the sputtering time was increased to 1125 seconds in line with the deposition rate to reach an expected thickness of 500nm.

Figure 4.2.1 Denton Vacuum Inc. DC & RF sputtering system.

Table 4.2.1 Sputtering parameters for Al film from Denton sputtering system log book.

Date	**Base Pressure (Torr)**	**Sputter Power (W)**	**Sputter Time (s)**	**Ar Flow (sccm)**	**Deposition Pressure (mTorr)**	**Deposition Temp (°C)**	**Expected Thickness (nm)**	**Deposition Rate (Å/sec)**
03/15/07	$5.0x10^{-5}$	400	1200	25	4.8	25	1500	12.5
11/29/07	$4.0x10^{-6}$	200	900	25	4.8	25	400	4.4
11/08/08	$2.7x10^{-6}$	100	435	25	4.8	25	100	2.3

After deposition, the film thickness was measured using a Tencor Instruments "Alpha-Step 200" profilometer shown in Figure 4.2.2. The profilometer's tip was moved across the substrate to film edge in three locations across the tape pull, determining a uniform film thickness of 400nm; 100nm less than expected. Also noted was that the film's profile shows that the film lifted off near the edge before settling back to the true film's thickness indicating there is a lack of adhesion which can be corrected with 10nm layer of titanium in future depositions. Upon viewing the film's surface with SEM it was determined that while the film was uniformly thick, the surface roughness was inadequate due to grains that were protruding from the surface as shown in Figure 4.2.3. These grains were determined to be Hillock growth formations that arise due to the internal stress of the film increasing, forcing the grains to the surface.

Figure 4.2.2 Tencor Instruments "Alpha-Step 200" profilometer.

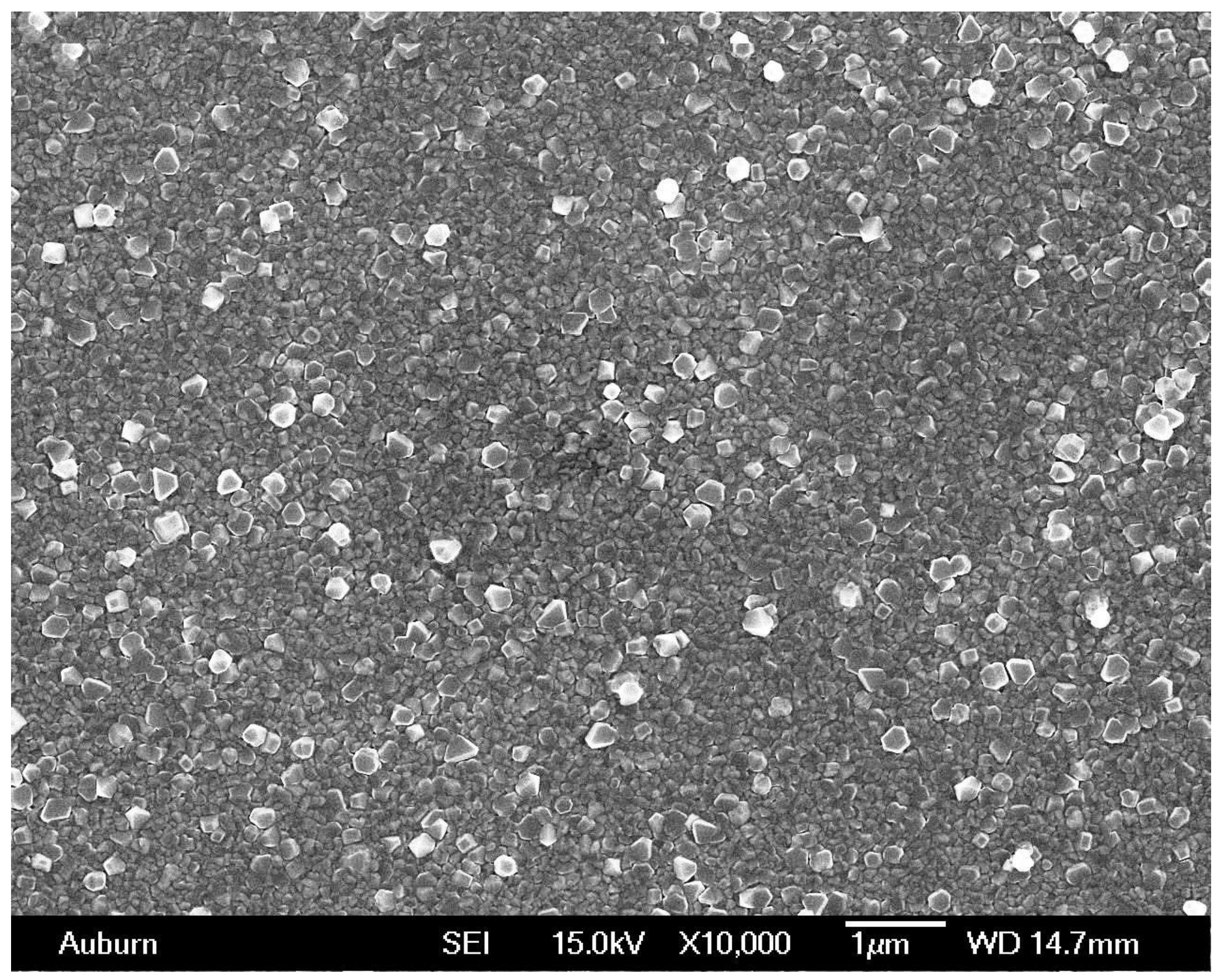

Figure 4.2.3 Hillock growth grains on film surface of 400nm Al on SiO_2.

It was determined that there are two main factors that facilitate internal film stress and consequently the growth of Hillock grains, both directly relating to sputtering power; chamber temperature and sputtering time. While a lower sputtering power decreases the resulting temperature of the chamber, making the Hillock grains grow at a slower rate, it also gives them more time to grow as it takes longer to sputter an equivalent film than at higher sputtering power. In order to fully investigate the influence of sputtering power on Hillock growth a series of

separate Al films, all with 10nm thick Ti layer for proper adhesion, were again deposited on SiO_2 substrates, each at a different sputtering power and time to maintain a consistent thickness of 500nm. The power ranged from a relatively low 75W to 700W which is the maximum allowed for this sputtering system. The sputtering conditions used are listed in Table 4.2.2. The actual film thickness was again determined using a profilometer across the film-substrate boundary averaged over three or four locations.

Table 4.2.2 Sputtering conditions for Al films to evaluate how changing sputtering power influences Hillock grain formation and density.

Sputter Power (W)	Base Pressure (Torr)	Sputter Time (s)	Ar Flow Rate (sccm)	Deposition Pressure (mTorr)	Temp (°C)	Expected Thickness (nm)	Actual Thickness (nm)	Deposit Rate (Å/sec)
75	$8.2x10^{-6}$	4000	25	4.8	25	500	480	1.2
125	$7.7x10^{-6}$	2400	25	4.8	25	500	450	1.9
175	$7.6x10^{-6}$	1715	25	4.8	25	500	500	2.9
300	$8.0x10^{-6}$	1000	25	4.8	25	500	500	5.0
400	$5.0x10^{-6}$	750	25	4.8	25	500	500	6.7
600	$8.2x10^{-6}$	500	25	4.8	25	500	500	10.0
700	$7.7x10^{-6}$	428	25	4.8	25	500	505	11.8

Each film was then viewed using the SEM to determine the film quality and density of Hillock formations as shown in Figure 4.2.4. As sputtering power increased, Hillock grain density decreased, improving the surface quality of the film which corresponds with literature.[21-23] It was decided to use 700W for all following Al depositions as it allowed for the lowest concentration of Hillock grains.

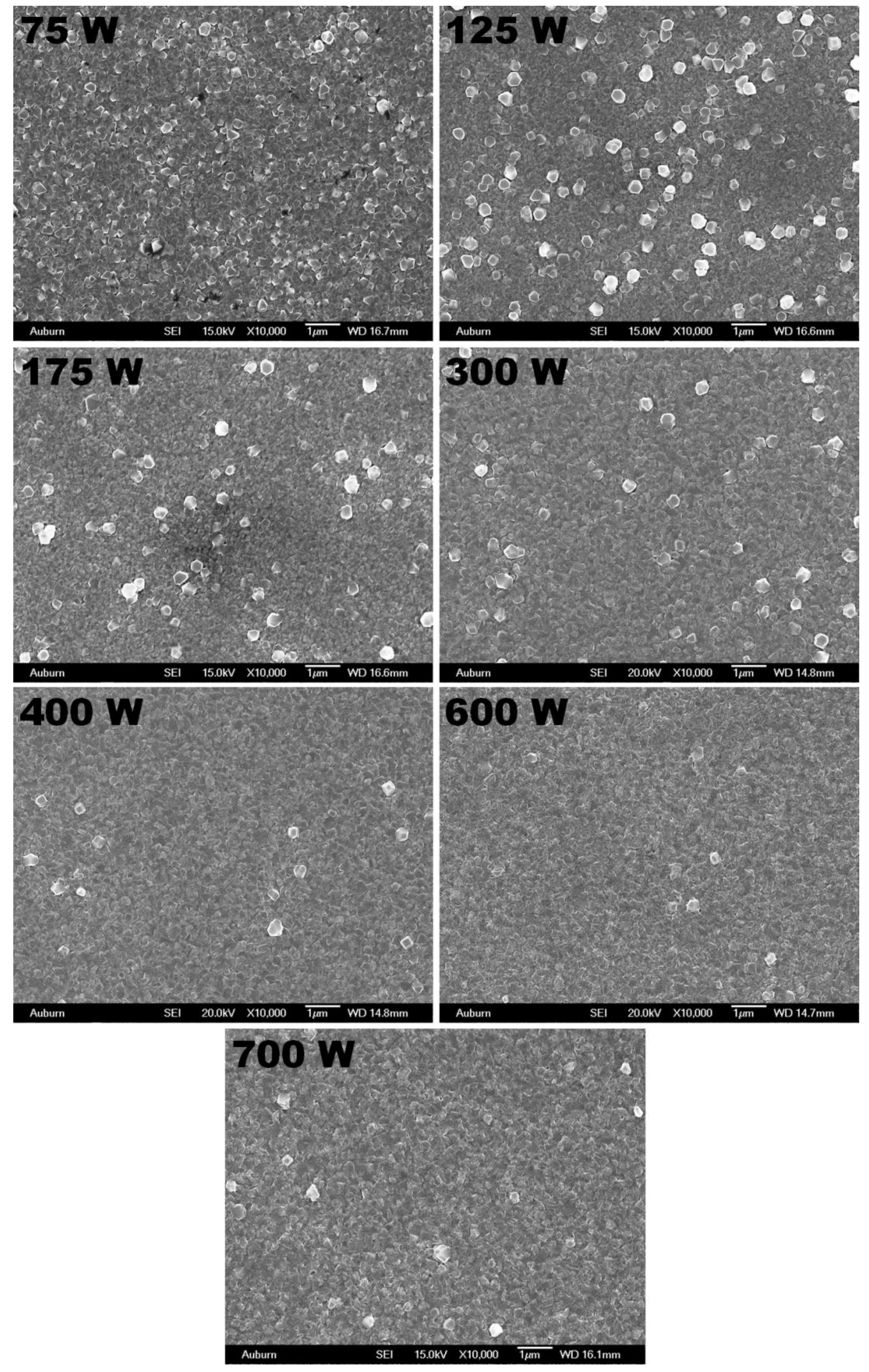

Figure 4.2.4 Micrographs of Al film surface as sputtered at different powers of 75, 125, 175, 300, 400, 600 and 700W at 10,000 magnifications.

Upon review of literature, the thickness of the aluminum film also has a large influence on Hillock growth grains as it allows them more time to grow due to the longer deposition time.[21-23] To evaluate this, and determine the effect film thickness has using the Denton Sputtering system at 700W, another group of depositions were performed, with parameters listed in Table 4.2.3, to vary the film thickness as 250nm, 500nm, 750nm and 1000nm. As before, all SiO_2 substrates were first deposited with a 10nm layer of Ti for proper adhesion, and film thickness was measured in at three different locations using a profilometer to determine actual thickness.

Table 4.2.3 Sputtering conditions for Al films to evaluate how varying film thickness influences Hillock grain formation and density.

Sputter Power (W)	Base Pressure (Torr)	Sputter Time (s)	Ar Flow Rate (sccm)	Deposition Pressure (mTorr)	Temp (°C)	Expected Thickness (nm)	Actual Thickness (nm)	Deposit Rate (Å/sec)
700	$3.9x10^{-6}$	215	25	5.0	25	250	243	11.3
700	$6.2x10^{-6}$	428	25	5.0	25	500	505	11.8
700	$5.5x10^{-6}$	645	25	5.0	25	750	743	11.5
700	$6.3x10^{-6}$	860	25	5.0	25	1000	1059	12.3

The samples were then viewed and compared using the SEM as shown in Figure 4.2.5. As expected through literature, the Hillock growths become much more prominent on the surface of the film as the thickness, and therefore sputtering time are increased. On the 250nm film, Hillock formations were extremely sporadic, and even their average size had been reduced to less than 100nm, making the film surface more desirable than the other thickness evaluated, but possibly still not sufficient. It was noted however that when viewing the film with the SEM, there are localized areas of the film that appeared to have a less uniform thickness. Figure 4.2.6

illustrates these areas, and this sporadic coverage originates from such a short sputtering time due to the high power required to avoid Hillock growth formations. While it is believed that it would be possible to indent in areas that look to have consistent coverage through the nanoindentation systems optical microscope, the exact film thickness would not be known; which is unsuitable for thin film nanoindentation as film thickness is a required parameter used in the studied models.

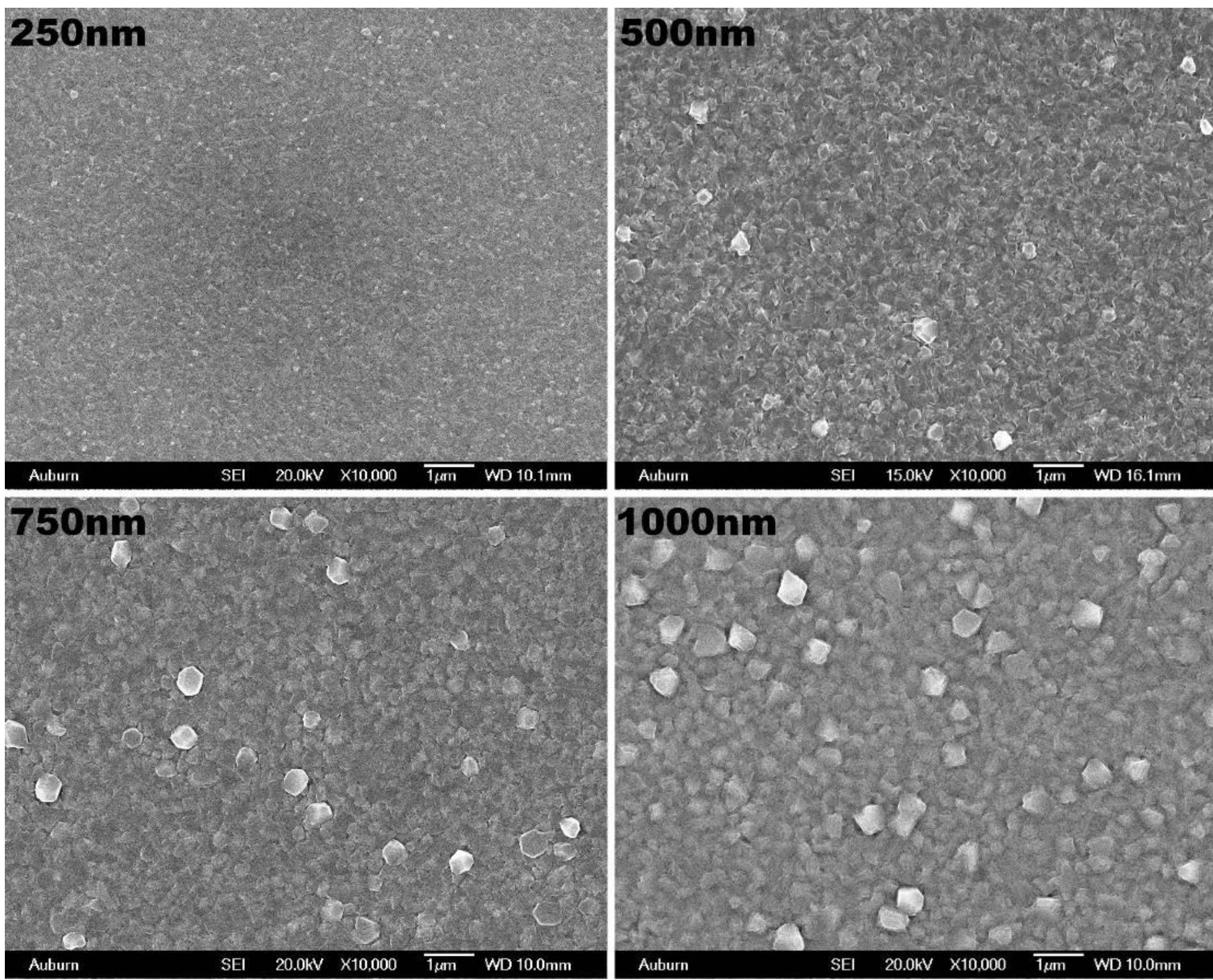

Figure 4.2.5 Micrographs of Al film surfaces as sputtered to different thickness of 250, 500, 750 and 1000nm at 10,000 magnifications.

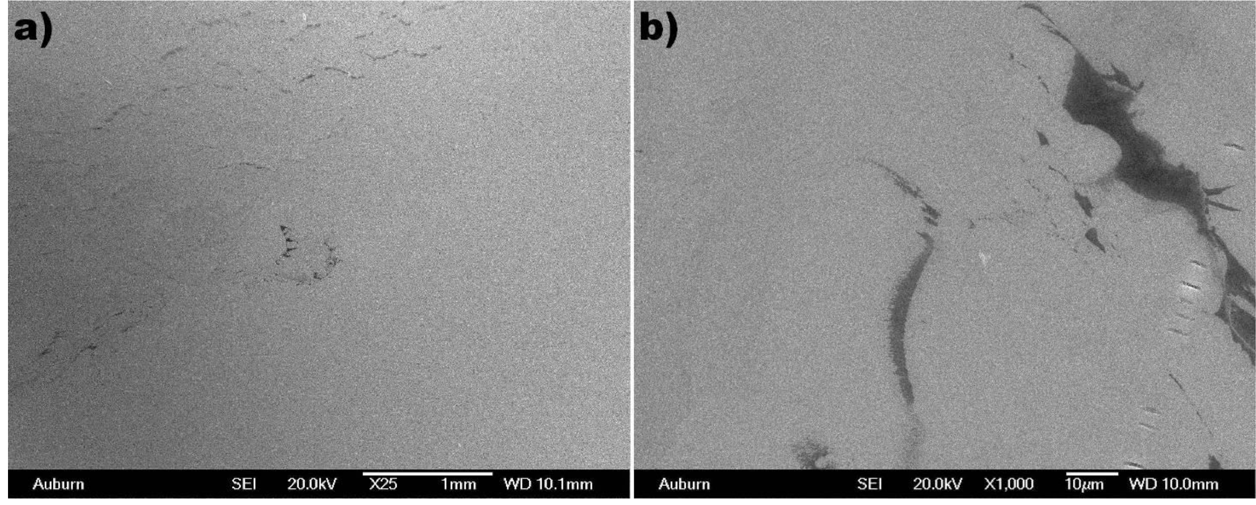

Figure 4.2.6 Micrographs of 250nm Al film on SiO2 at (a) 25x and (b) 1000x showing sporadic coverage.

Due to the inability to create a consistent thickness film of aluminum with adequate surface quality, it was determined to use another film, platinum, that has a similar Poisson's ratio of 0.36, with widely understood deposition parameters and results due to its wide use in MEMS research.[18, 19] While the Young's modulus of platinum is a bit higher at 168 GPa, it still has a pile-up behavior when indented allowing for one of the same goals as the aluminum film.[18] The sputtering parameters to obtain a 230nm thick layer of platinum with titanium adhesion layer are listed in Table 4.2.4.

Table 4.2.4 Sputtering parameters of 230nm Pt film with Ti adhesion layer.

Substrates	Al, Si, Cu, In, Sn, Pt, Ti, Ta	
Base Pressure (Torr)	2.6×10^{-6}	
Magnetron Type	**DC**	**DC**
Target Material	Pt	Ti
Pre-Sputtering Power (W)	100	400
Pre-Sputtering Time (sec)	15	25
Sputtering Power (W)	100	400
Sputtering Time (sec)	800	25
Gas 1 (Ar) flow rate (sccm)	25	25
Gas 2 (O2/N2) flow rate (sccm)	0	0
Deposition Pressure (mTorr)	4.7	4.7
Deposition Temperature (°C)	23	23
Soak Time (sec)	0	0
Substrate holder rotation (%)	50	50
Ignition Pressure (mTorr)	50	50
Expected Film Thickness (nm)	250	10
Actual Film Thickness (nm)	230	10

The resulting platinum film was observed with SEM and found to have consistent coverage and excellent surface quality, shown in Figure 4.2.7. Table 4.2.5 shows that using the profilometer, the film thickness of each film-substrate combination was measured in three locations and then averaged to determine the film thickness of 230nm. As the platinum film had a good surface quality with no disproportionally large protrusions over the film's surface, this platinum film was determined to be the best candidate for indentations.

Table 4.2.5 Film thickness of sputtered platinum films.

Substrate	Location 1 (nm)	Location 2 (nm)	Location 3 (nm)	Average (nm)
SiO_2	220	235	220	225
Si	235	236	231	234
Pt	210	235	214	220
Al	235	236	225	232
Ta	232	225	240	232
Ti	239	246	220	235
In	210	233	243	229
Sn	230	246	210	229
Cu	231	243	228	234

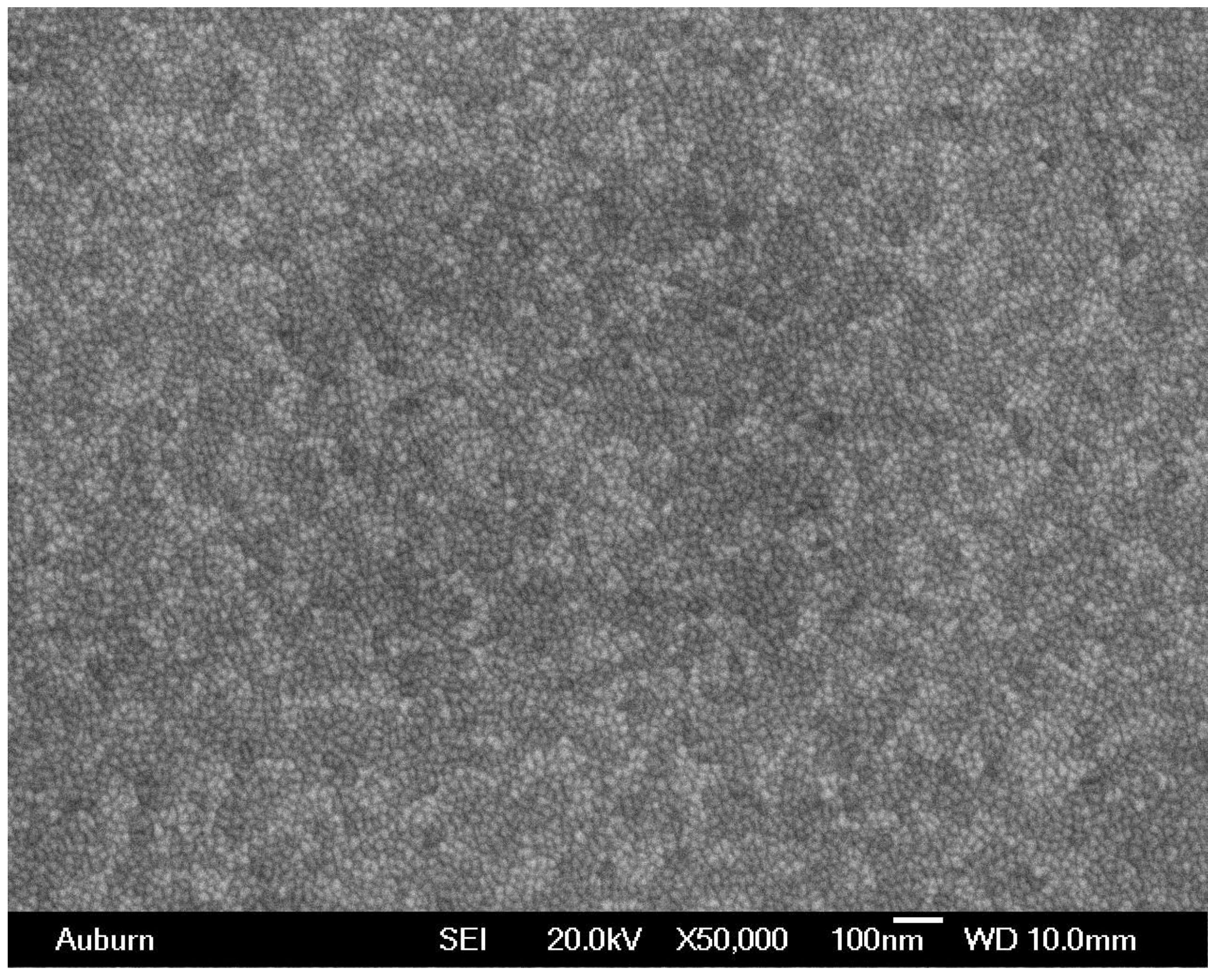

Figure 4.2.7 Surface quality of platinum film on SiO2 substrate.

4.3 Nanoindentation

Nanoindentation was performed using TestWorks 4 to drive an MTS Nanoindenter XP (Agilent Technologies, Santa Clara, CA), as shown in Figure 4.3.1, through a continuous stiffness measurement, or CSM. The depth controlled tests used a Berkovich type diamond tip with a harmonic displacement of 2nm, and an allowable drift rate of 0.05nm/s. Twenty-five indents were performed on a fused silica reference in order to calibrate the area coefficients of the tip. For each sample tested, single crystal aluminum was first deeply indented to remove any debris or contamination from the tip, followed by a minimum of four indents in the silica reference to refine the tip calibration if needed. The Poisson's ratio used in testing film-substrate samples was the bulk value of the film. For each film and substrate combination, twenty-five 500nm CSM indents were run to fully cover behavior through the film, and then averaged for the composite, or apparent Young's modulus verses indention depth using the standard Oliver-Pharr analysis.[13]

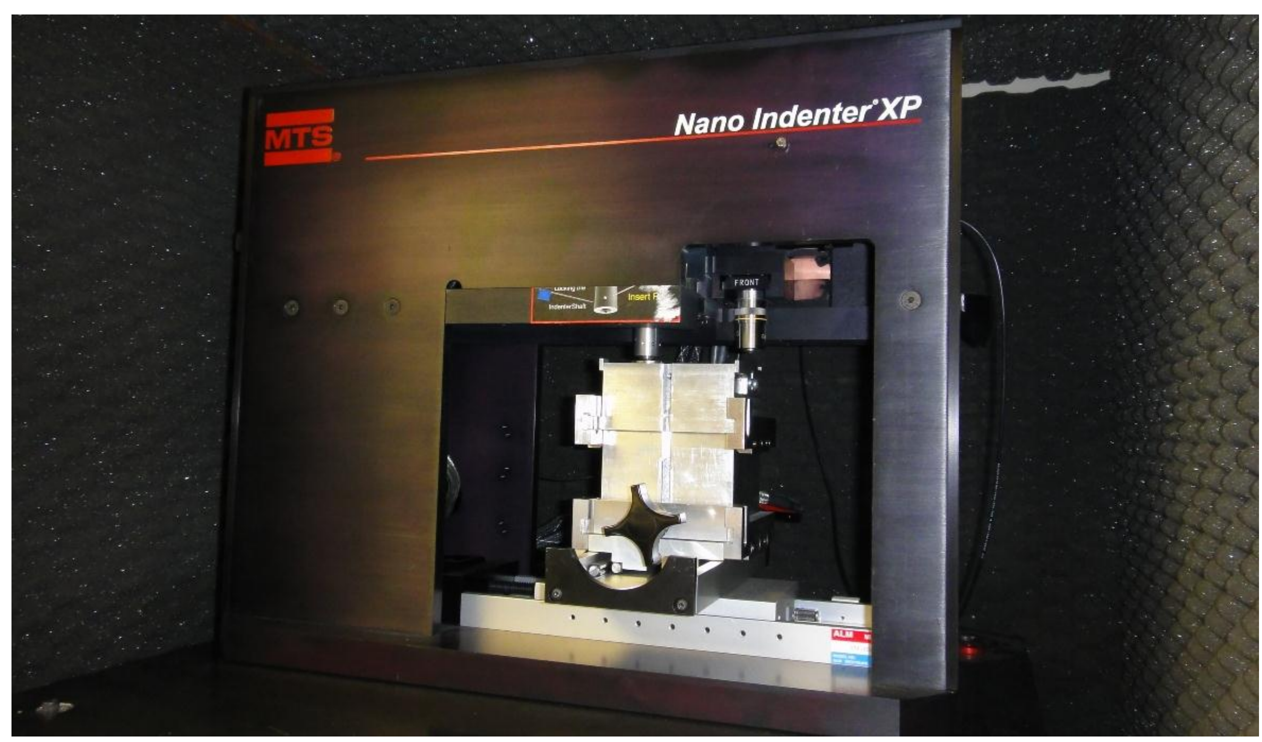

Figure 4.3.1 Image of MTS Nano Indenter XP nanoindentation system.

Chapter 5: Results and Discussions

5.1 Experimental Nanoindentation Analysis

After twenty-five indents were run on each substrate, and film-substrate sample, erroneous tests were removed, and then an averaged Young's modulus verses indention depth was plotted along with its correlating standard deviation error bars. The erroneous tests result from the indenter believing it has made contact with the surface when it has usually due a sharp vibration causing the tip to momentarily make contact before withdrawing, reporting no Young's modulus until it does eventually reach the surface again; resulting in a Young's modulus verses displacement plot similar to Figure 5.1.1. While these tests are deleted, there is no possibility of them being confused with a legitimate, but unexpected result.

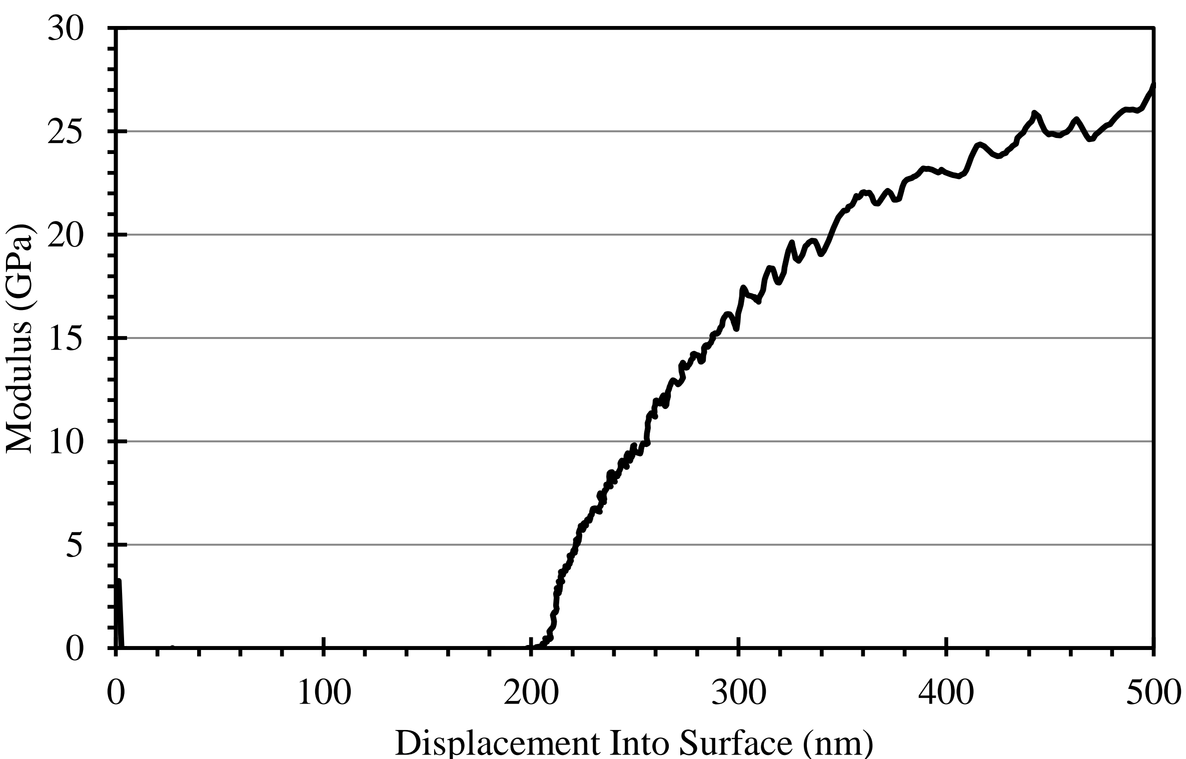

Figure 5.1.1 *E-h* curve of an example erroneous indention that would be deleted before averaging indentation results.

To further understand the methodology of how TestWorks arrives at its reported Young's modulus of the sample and for a method to change the Poisson's ratio on the fly, an Microsoft Excel worksheet was created that derives the raw modulus using the original Poisson's ratio used, and then allows for a recalculation using a different Poisson's ratio using Eq. (2). To check validity, a sample was recalculated within TestWorks and Excel using a Poisson's ratio of 0.10, 0.20, 0.30, 0.40, and 0.50, and then compared in Figure 5.1.2 to show they match and that the Excel file correctly recalculates Young's modulus, if a change of Poisson's ratio is desired.

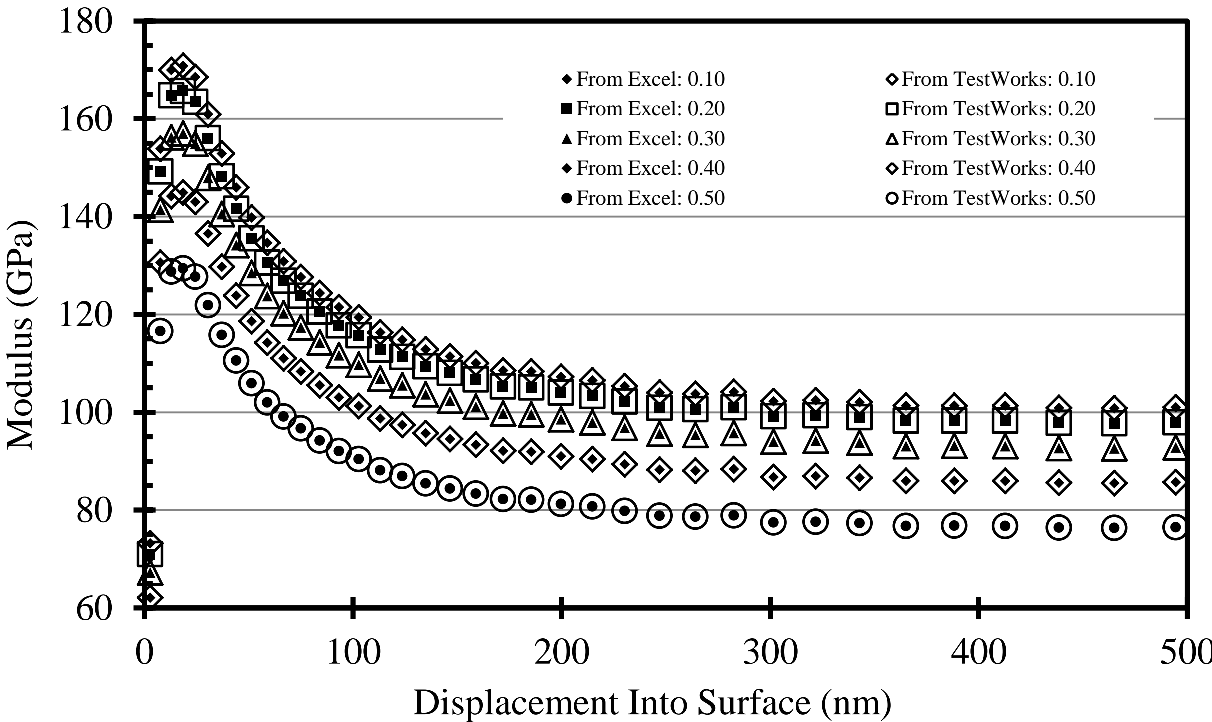

Figure 5.1.2 Checking validity of changing Poisson's ratio through Excel when compared to recalculating the sample through TestWorks.

The Young's modulus, *E* verses indention depth, *h*, or *E-h* curves, are shown in Figures 5.1.3a through 5.1.3h. These indentions were preformed, instead of relying on the values from literature, as the substrates' Young's moduli can vary due to are a number of factors that can influence the elastic behavior such as crystal orientation, or large enough grain size that you can indent on that single grain's different crystal structure. It is notable that for very shallow displacement the Young's modulus does not immediately start at the bulk value of the materials. This behavior is due to the loss of contact between the tip and material as the tip lifts from the surface during the oscillation cycle of the indenter in accordance to CSM.[4] For the substrates that do not have pile-up around the indenter tip, Ti, Pt, Ta and Si the curves immediately rise to their Young's modulus and remain constant independent of indention depth. A higher Young's

modulus is reported for the single crystal Al and Cu (100) as they readily plastically deform causing material to pile-up around the tip as it penetrates, leading to more elastic recovery than there would be otherwise. Once the tip moves deep enough, the pile-up against the tip becomes less a less dominate factor, allowing for the Young's modulus to reduce toward its true value. Both the In and Sn substrates have relatively larger error bars due to their previously discussed inability to be polished and their resulting lack of surface quality.

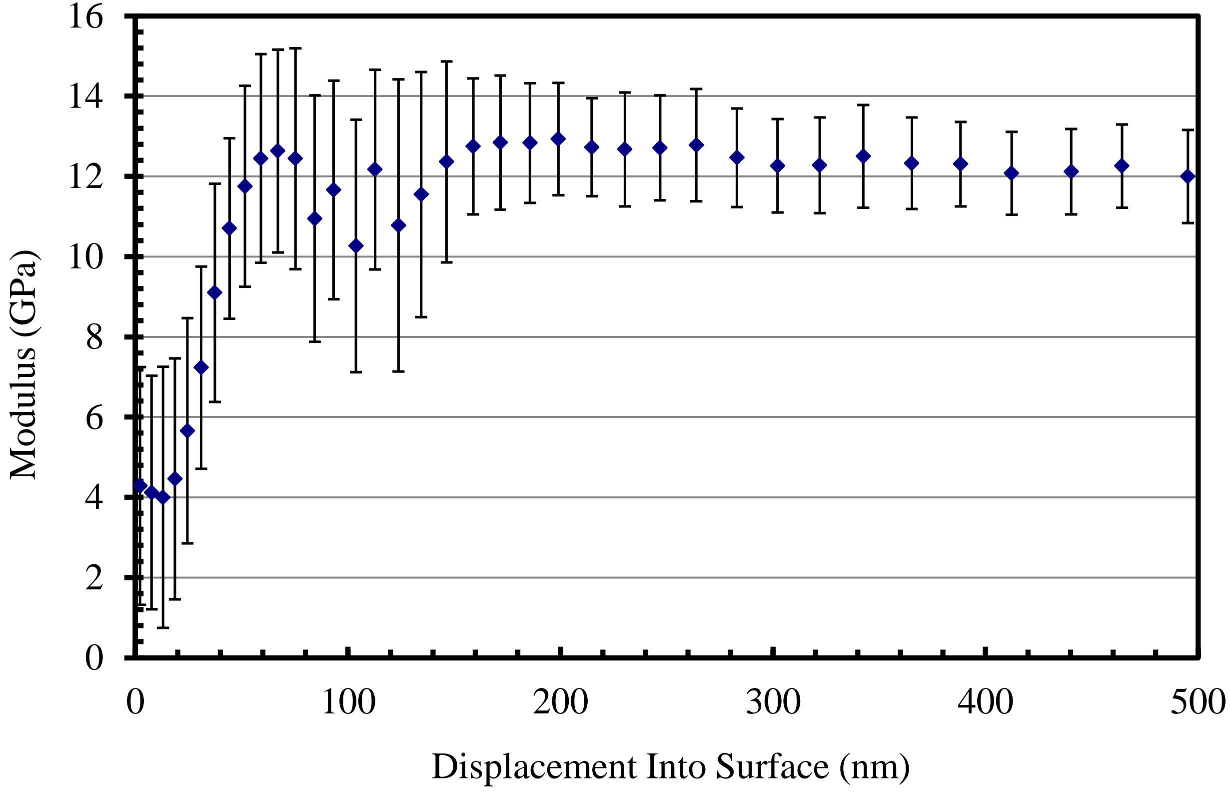

Figure 5.1.3a *E-h* curve for In substrate after flattening with Arbor press.

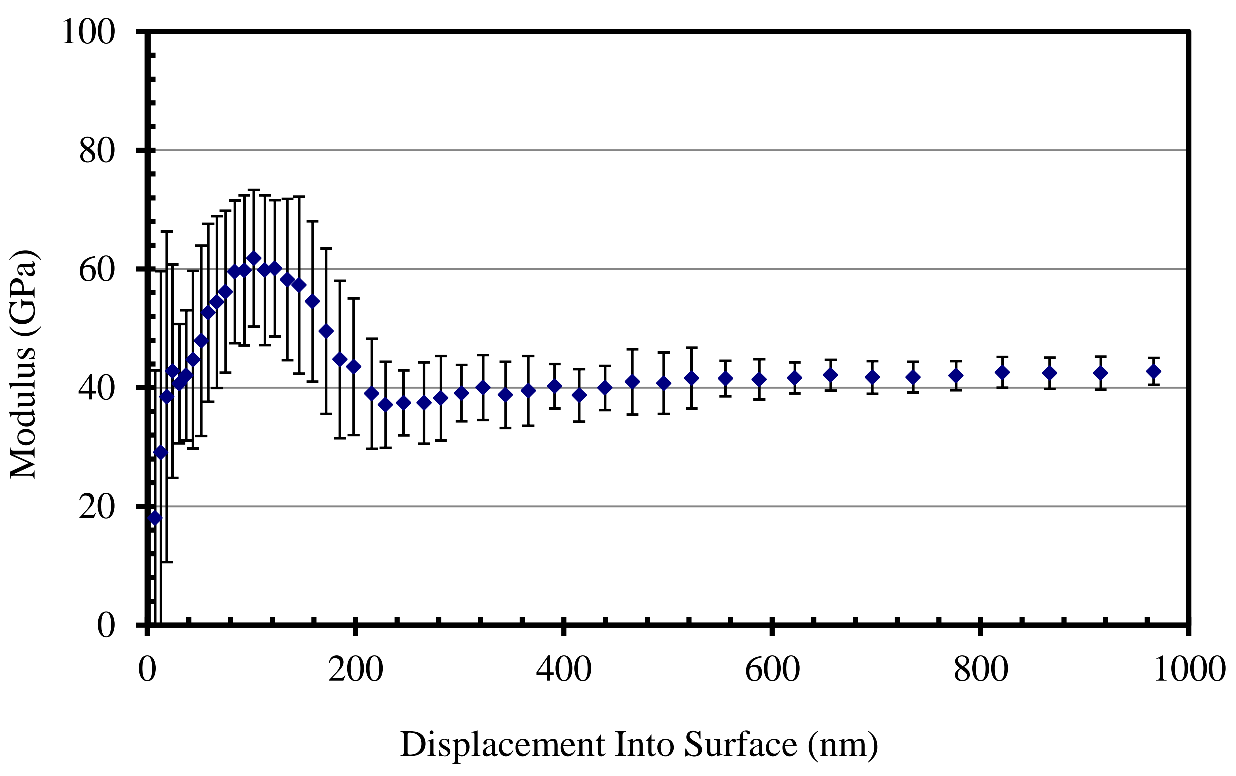

Figure 5.1.3b *E-h* curve for Sn substrate after flattening with Arbor press.

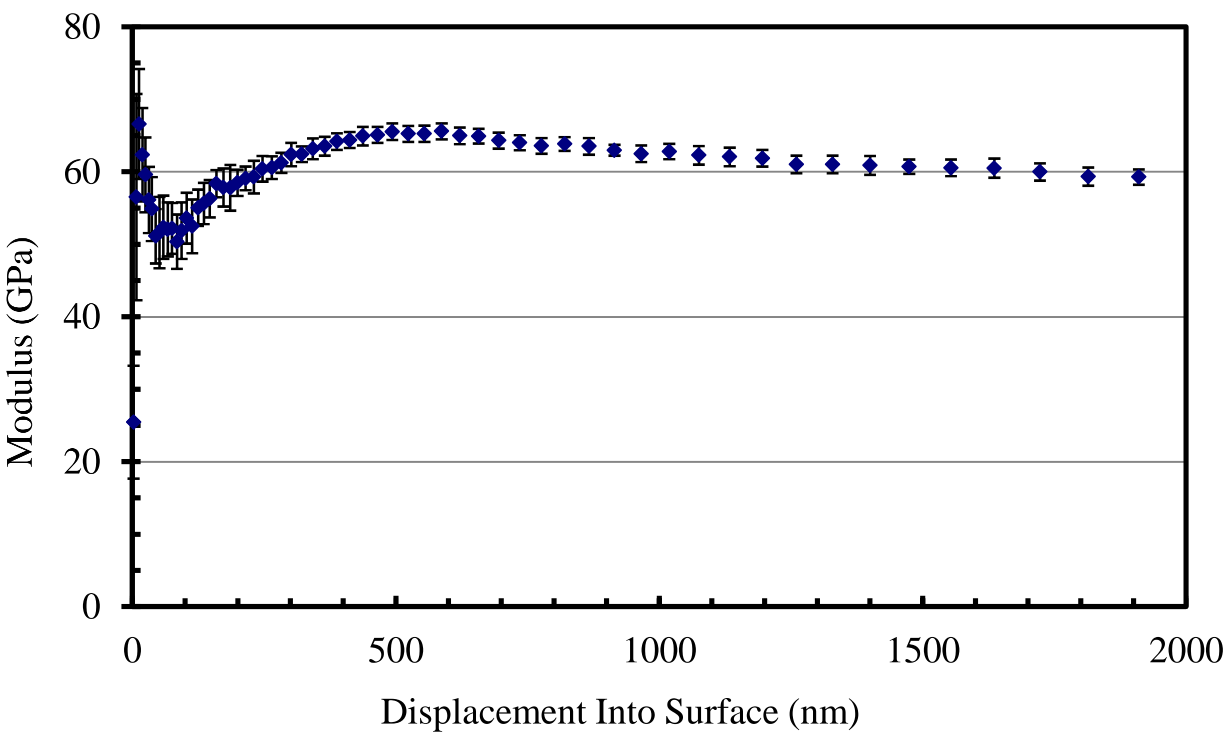

Figure 5.1.3c *E-h* curve for Al single crystal substrate, orientation (100).

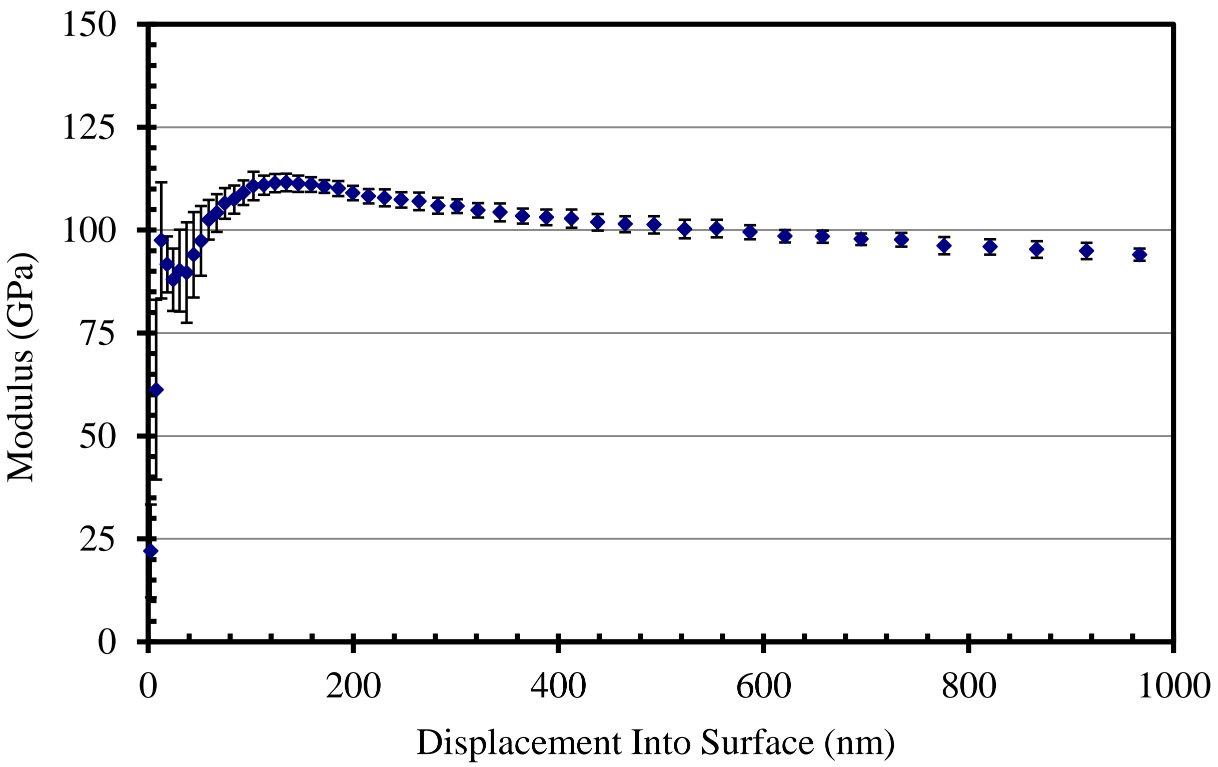

Figure 5.1.3d *E*-*h* curve for Cu single crystal substrate, orientation (100).

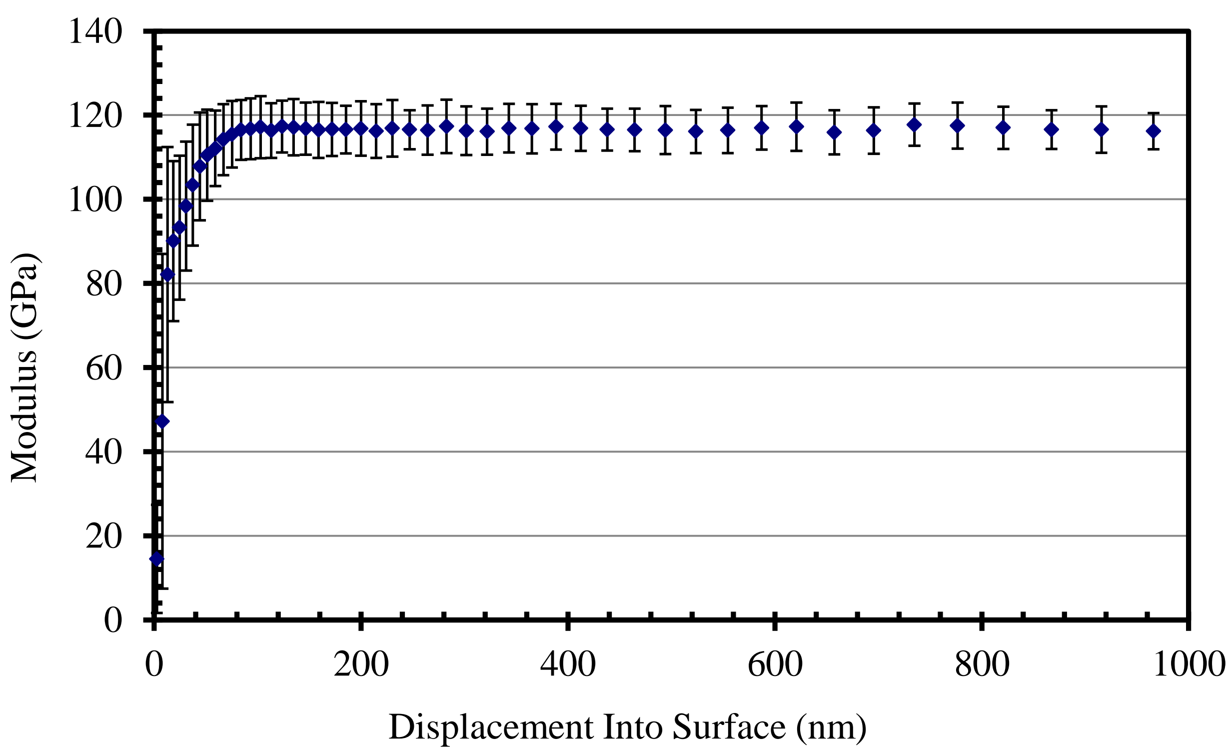

Figure 5.1.3e *E*-*h* curve for Ti substrate.

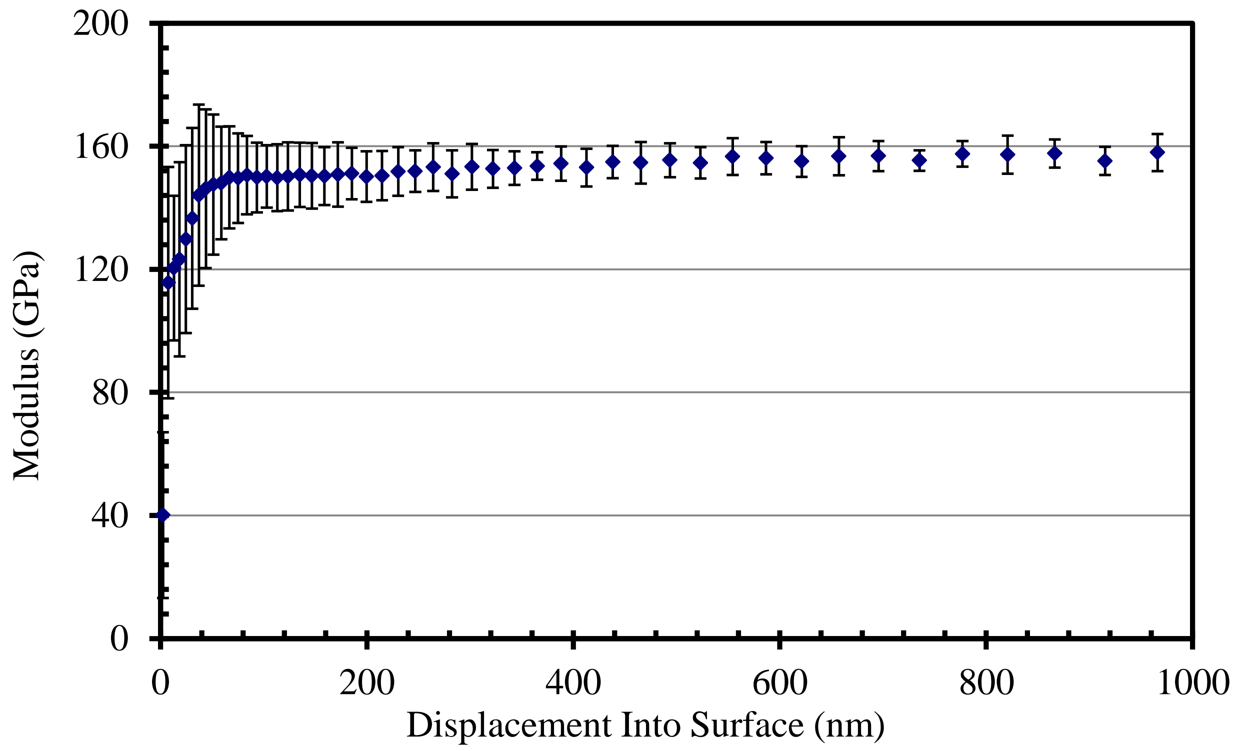

Figure 5.1.3f *E-h* curve for Pt substrate.

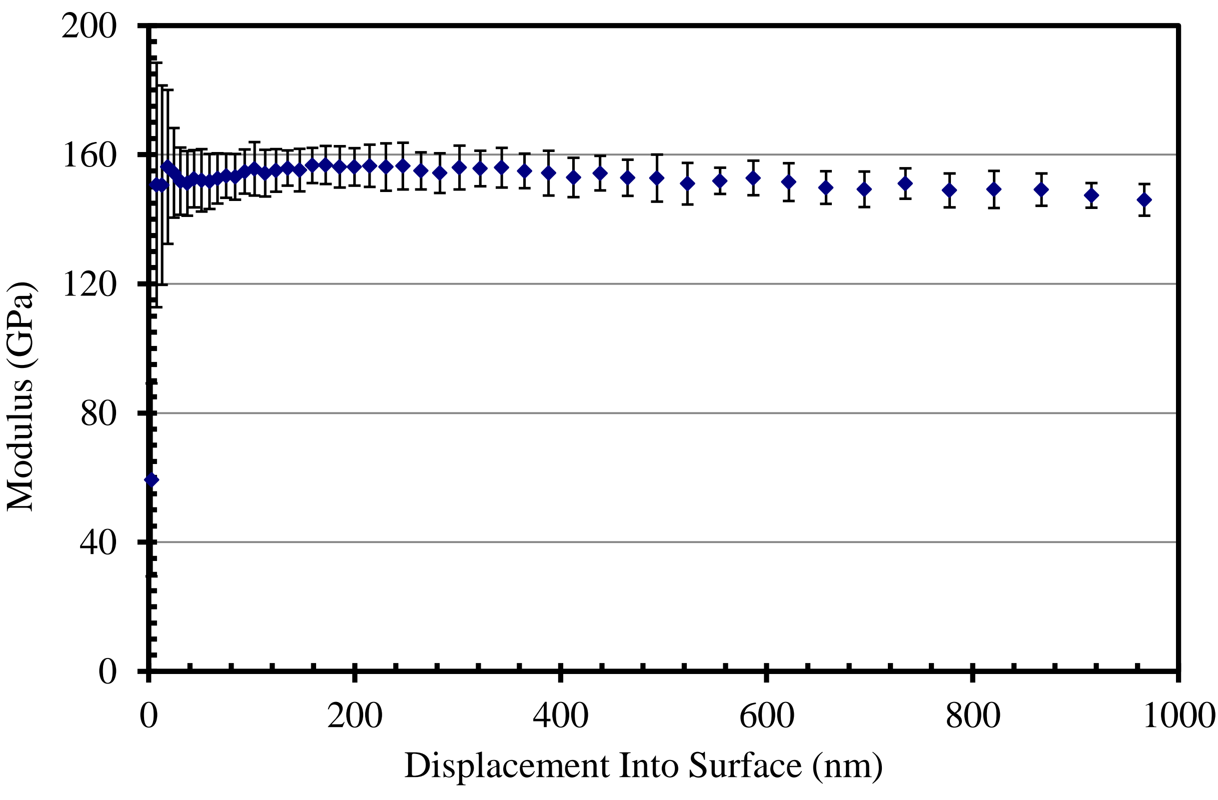

Figure 5.1.3g *E-h* curve for Ta substrate.

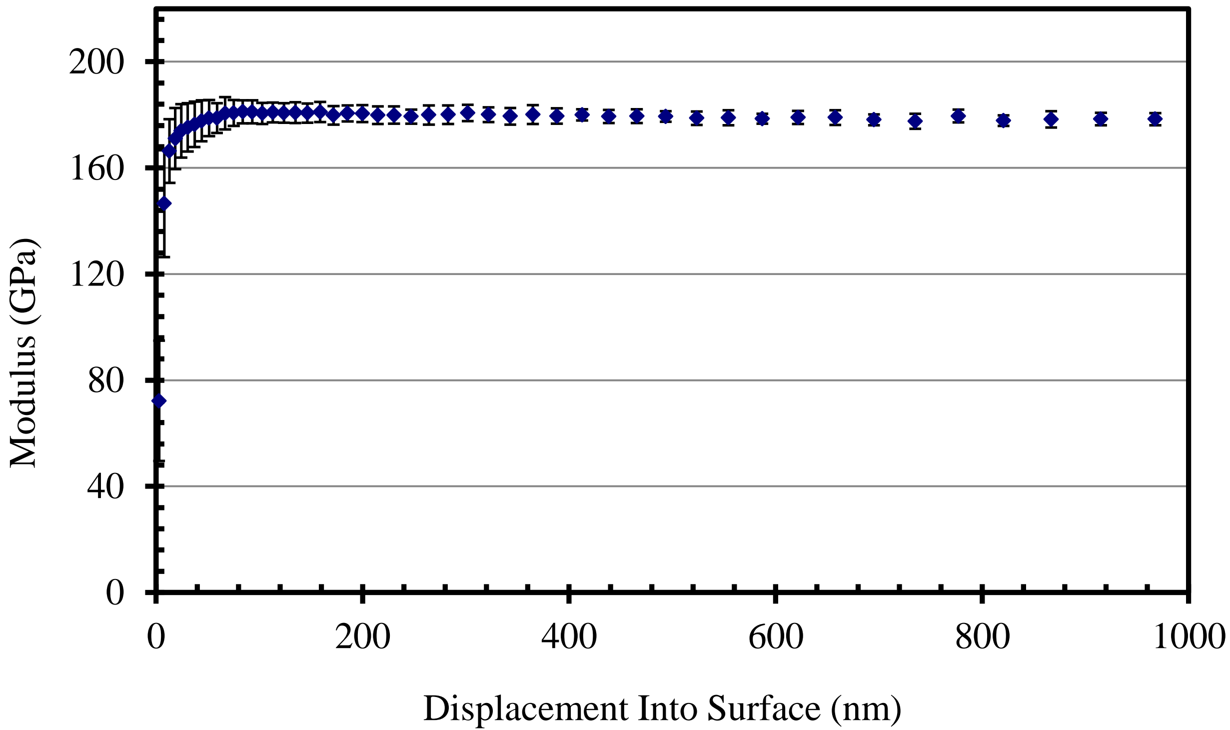

Figure 5.1.3h *E-h* curve for Si single crystal substrate, orientation (100).

Once it was known how the substrates deposited on behaved when indented independent of films, the Pt film-substrate samples were indented and *E-h* curves shown along with several other variables of interest in Figures 5.1.4a through 5.1.4h; the Zhou-Prorok model from in Eq. (13), film's alpha extracted from Eq. (13), and film's Young's modulus extracted from Eq. (15). The film's alpha from Eq. (13) or Poisson's ratio, as described by Zhou et al. is useful as it lends credence to the Zhou-Prorok model when it remains constant through all indention depth as the film's Young modulus is independent of indention depth, pile-up or sink effects and substrate properties. The film's Young's modulus is extracted from Eq. (15) as it also important since it should ideally remain constant independent of all other variables. The film's alpha is obtained from Eq. (13) opposed to the film's Young's modulus from Eq. (15) as the latter was created to better describe the substrate's effect on the film's modulus, and does not more precisely

characterize the film's alpha. Also included is the Doerner-Nix model in select cases to show how it compares to the Zhou-Prorok model in its ability to predict the composite modulus for the same parameters. From this data, the previously mentioned extracted values for the film's Poisson's ratio and Young's modulus match well with their expected values, and are shown in Table 5.1.1.

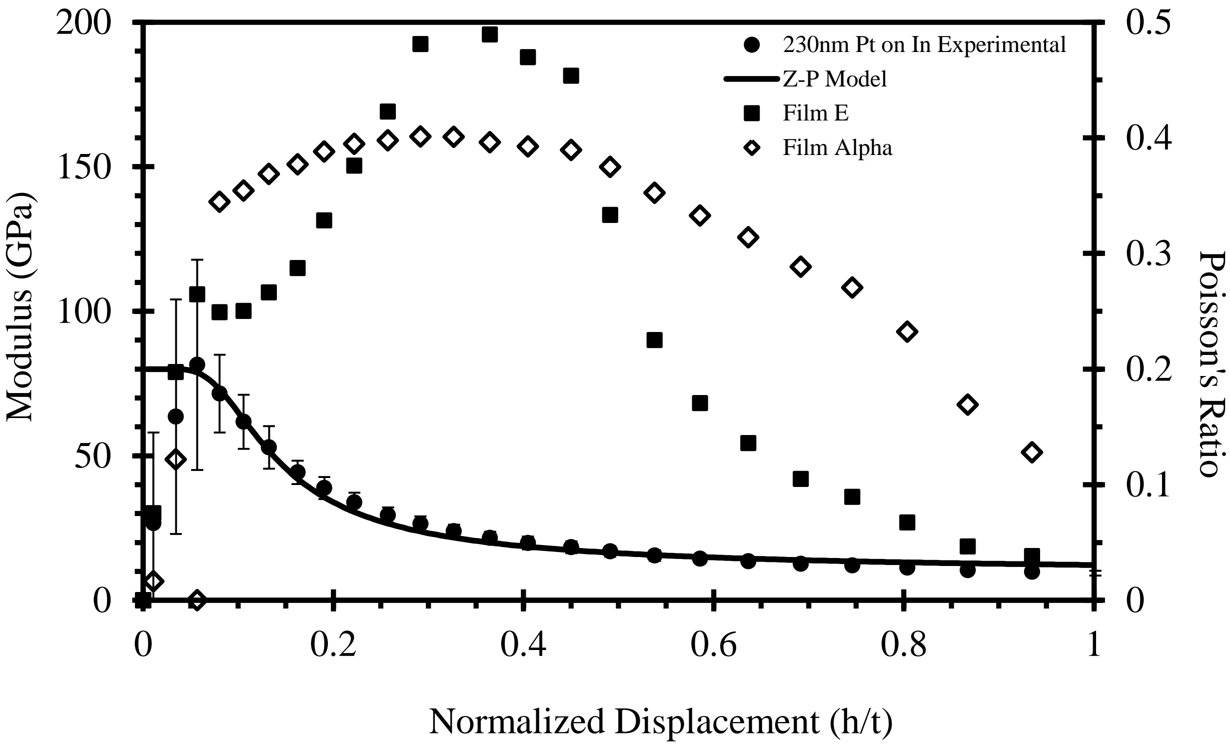

Figure 5.1.4a *E-h* curve for 230nm Pt on In with Z-P model, film E and film alpha.

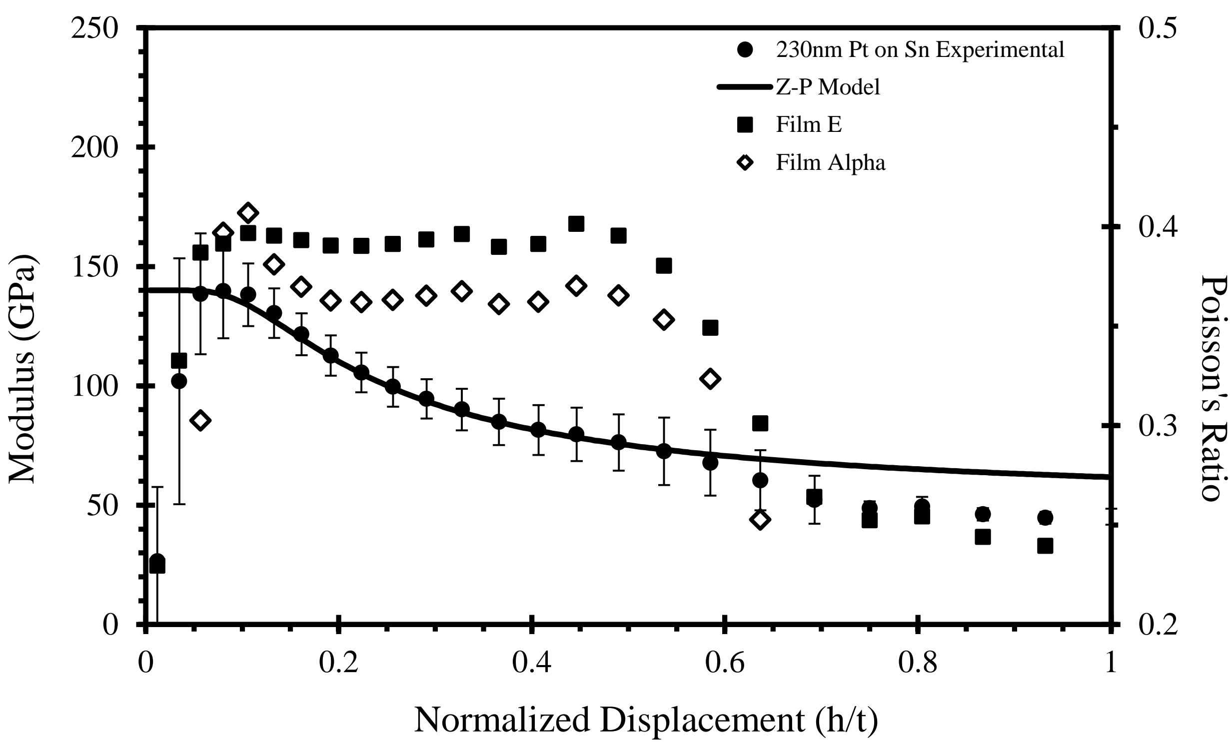

Figure 5.1.4b *E-h* curve for 230nm Pt on Sn with Z-P model, film E, and film alpha.

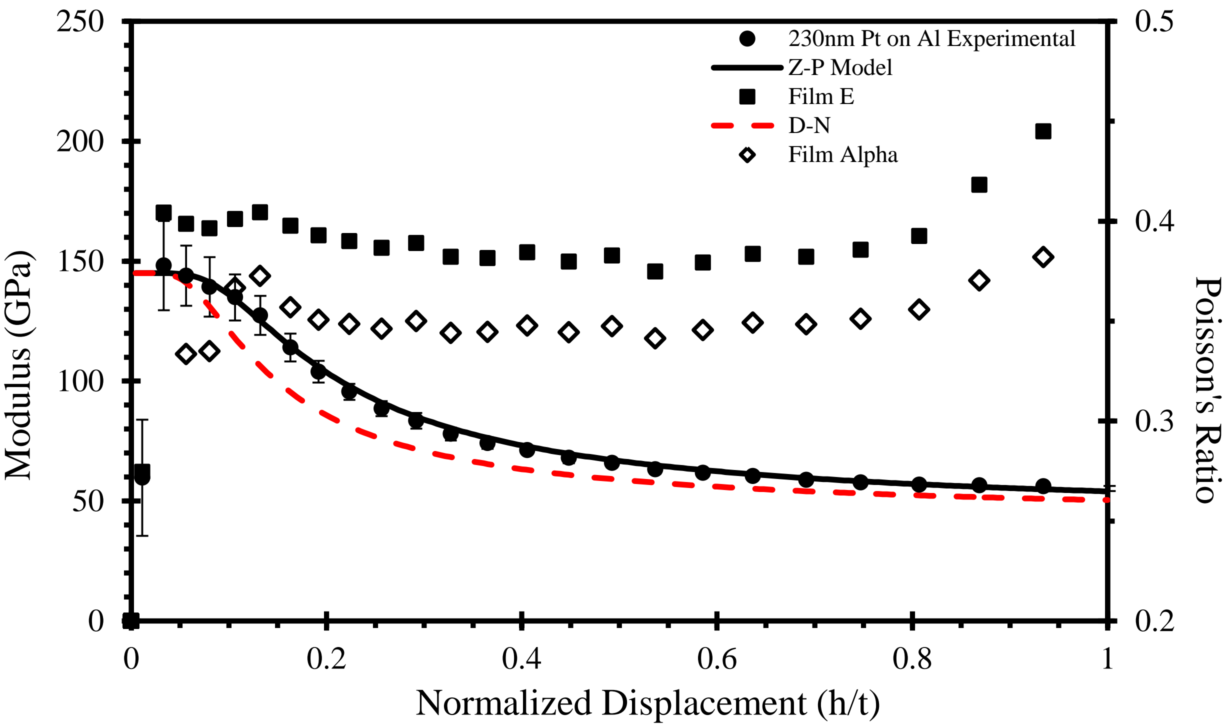

Figure 5.1.4c *E-h* curve for 230nm Pt on Al with Z-P model, D-N model, film E, and film alpha.

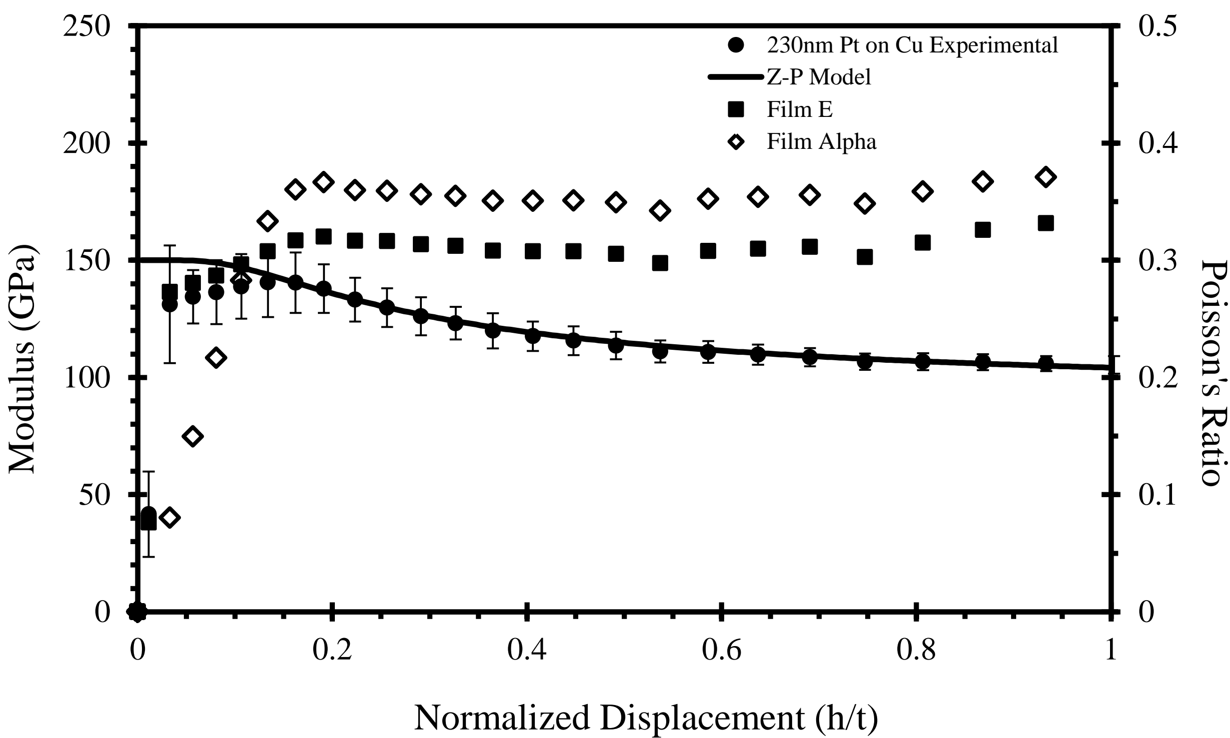

Figure 5.1.4d *E-h* curve for 230nm Pt on Cu with Z-P model, film E, and film alpha.

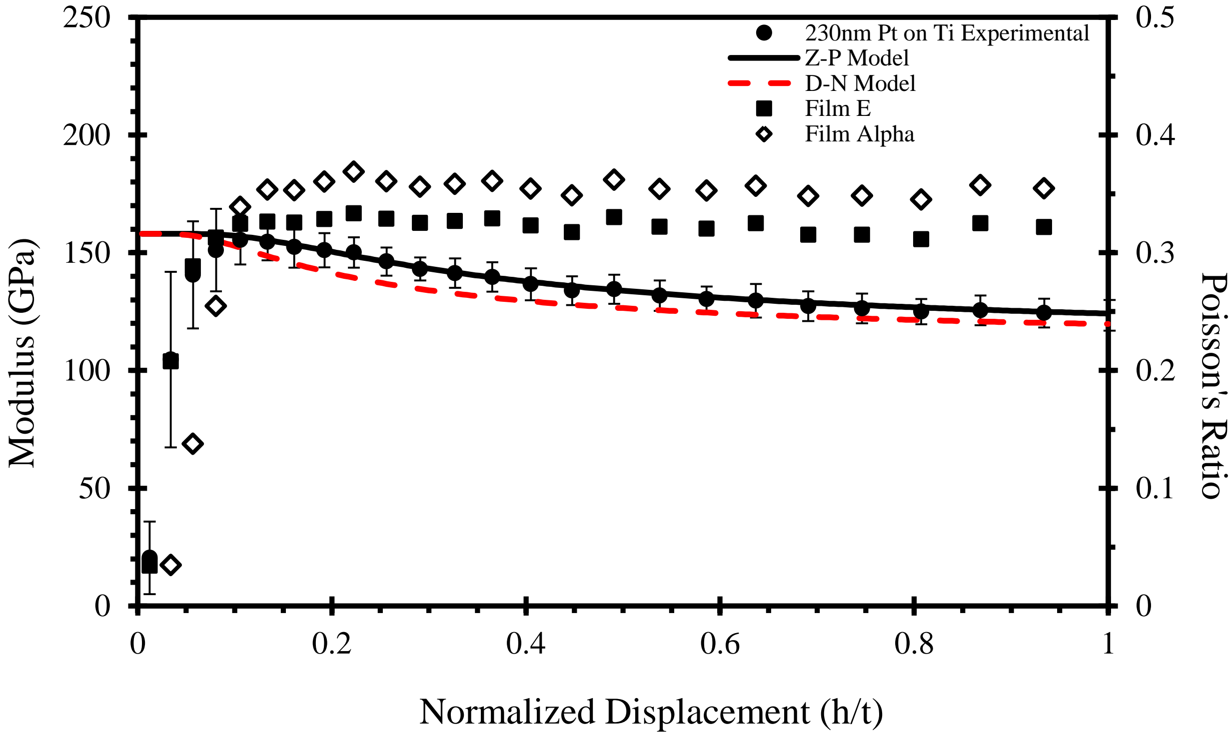

Figure 5.1.4e *E-h* curve for 230nm Pt on Ti with Z-P model, D-N model, film E, and film alpha.

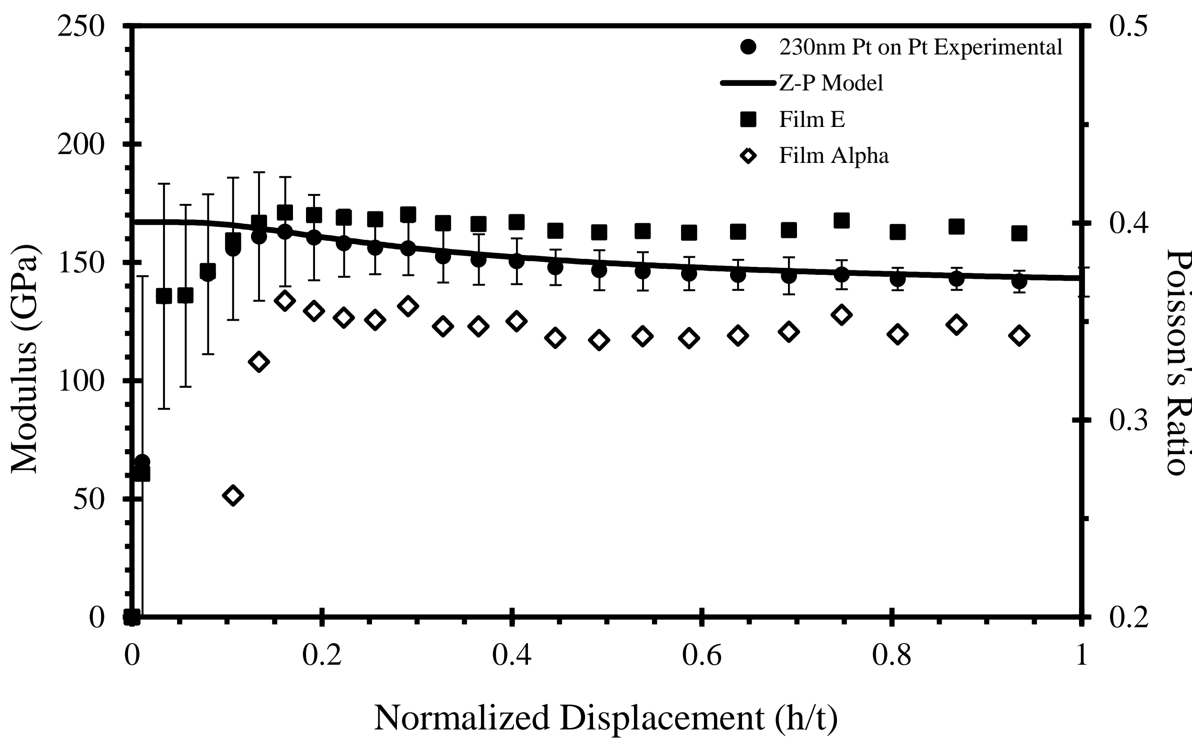

Figure 5.1.4f *E-h* curve for 230nm Pt on Pt with Z-P model, film E, and film alpha.

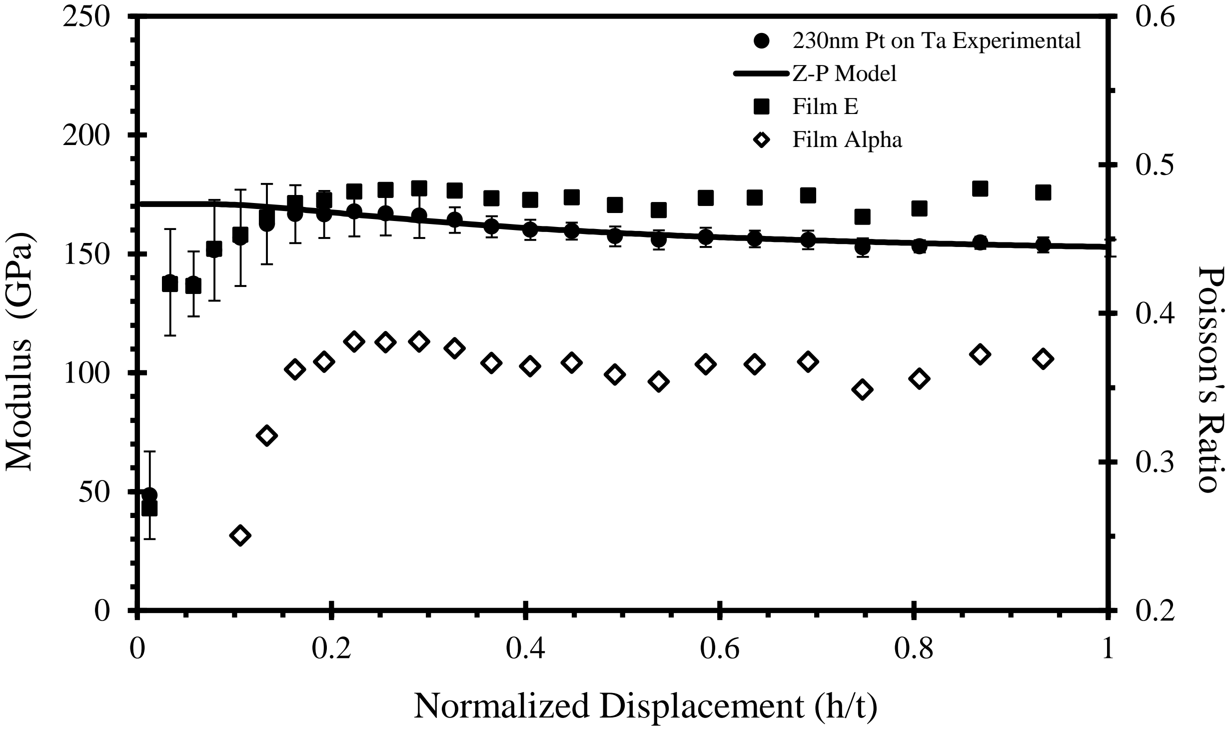

Figure 5.1.4g *E-h* curve for 230nm Pt on Ta with Z-P model, film E, and film alpha.

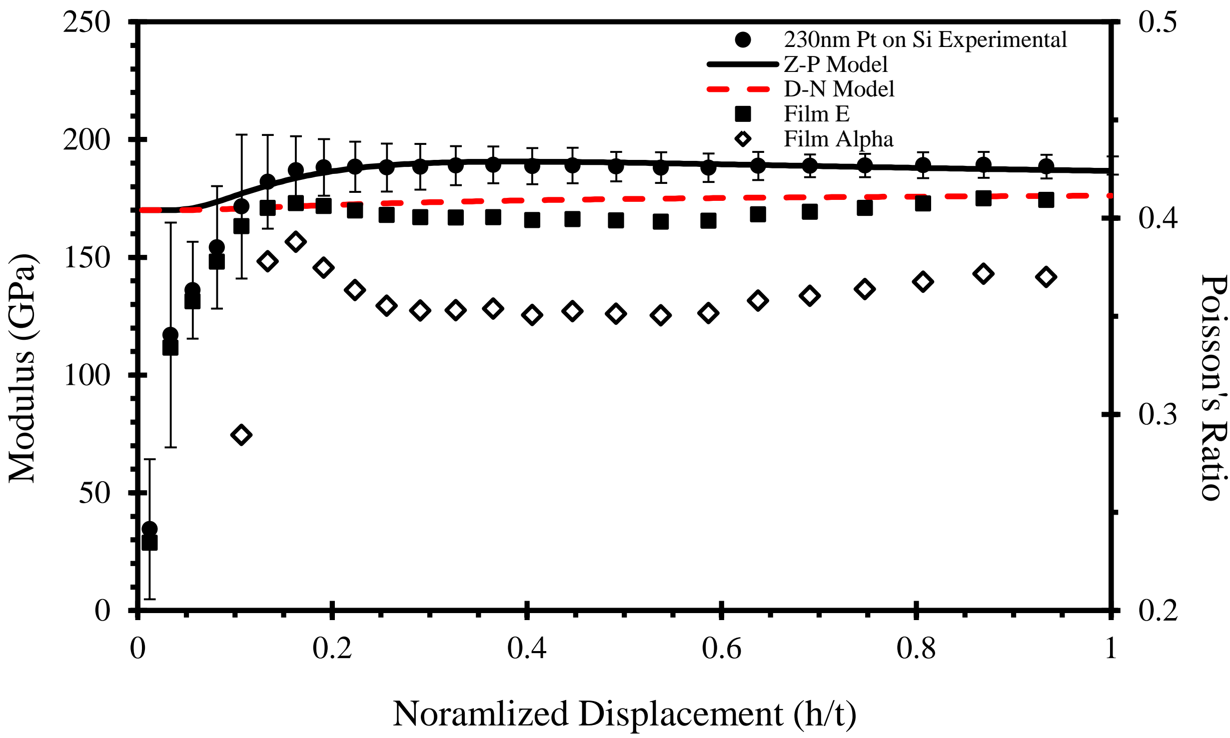

Figure 5.1.4h *E-h* curve for 230nm Pt on Si with Z-P model, D-N model, film E, and film alpha.

Table 5.1.1 Values of films' Young's moduli and alphas from Eq. (15) and (17) for each Pt film on substrate combination, as well each substrate's Young's Modulus obtained from nanoindenting directly into the substrate.

Substrate	E'sub	νsub	E'film	νfilm
In	12	0.44	?	?
Sn	42	0.36	163 ± 5	0.36
Al	60	0.35	157 ± 7	0.35
Cu	100	0.35	158 ± 7	0.35
Ti	116	0.32	162 ± 2	0.35
Pt	168	0.36	167 ± 4	0.35
Ta	153	0.34	171 ± 7	0.36
Si	178	0.28	166 ± 2	0.36

While the majority of the film-substrate combinations' experimental data matched well with the Zhou-Prorok model, along with its derived film alpha and E, there are a few of

occasions where this is not true; mainly with In and Sn. To further investigate why these cases don't hold true, it is best to have a better image of how the indents interact with the surface in terms of surface quality, and if erroneous contact area in the form of pile-up or sink in is a factor. Toward this end, SEM micrographs at 20,000 magnification were taken for each indent as shown in Figures 5.1.5a through 5.1.5h.

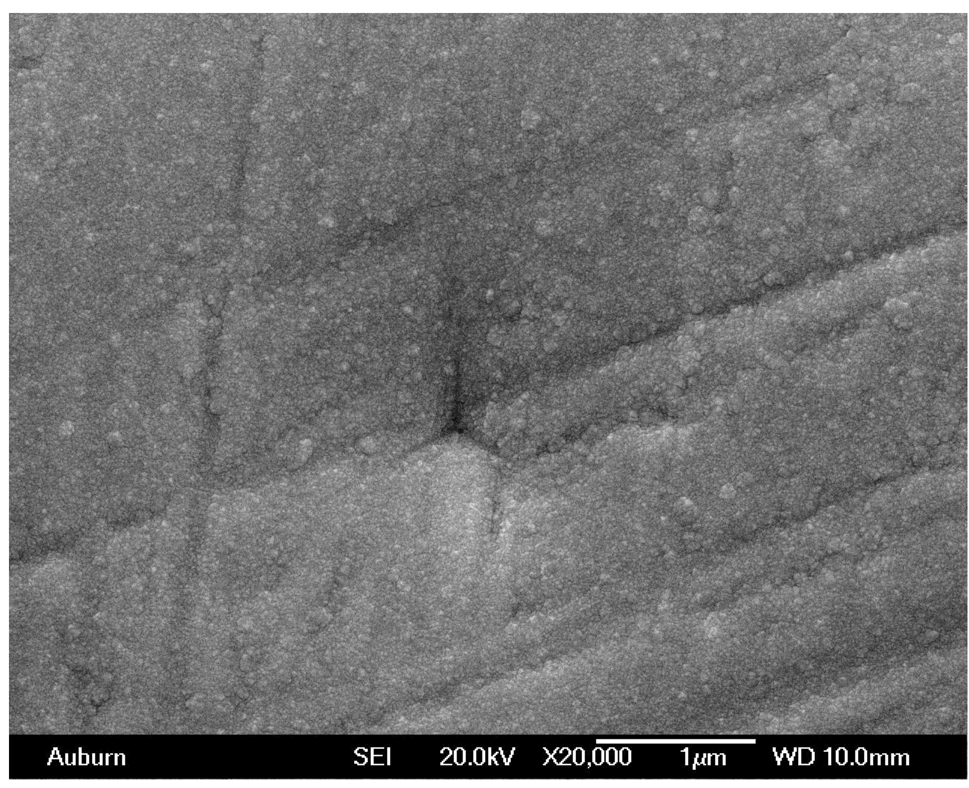

Figure 5.1.5a 230nm Pt on In: 500nm indention

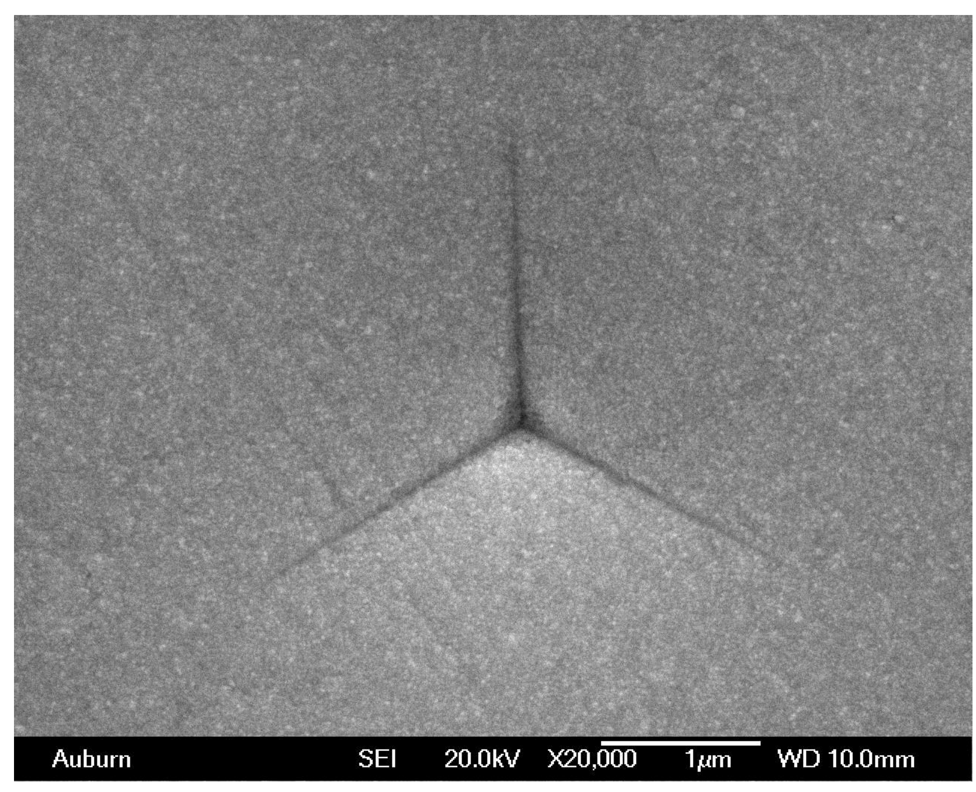

Figure 5.1.5b 230nm Pt on Sn: 500nm indention.

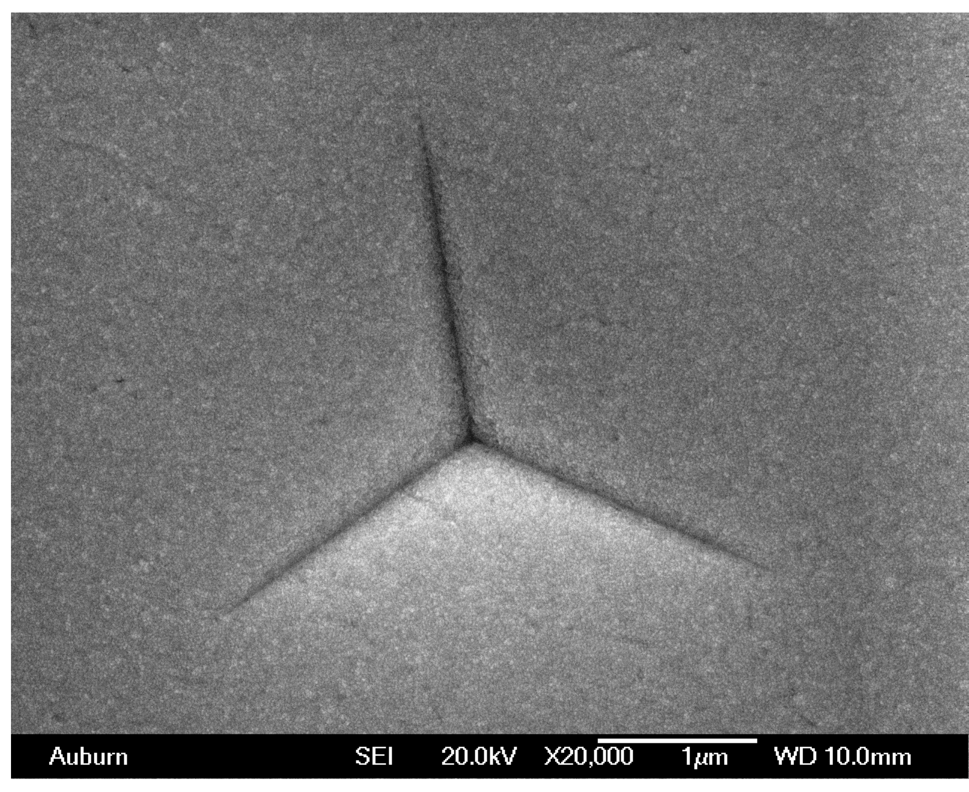

Figure 5.1.5c 230nm Pt on Al: 500nm indention.

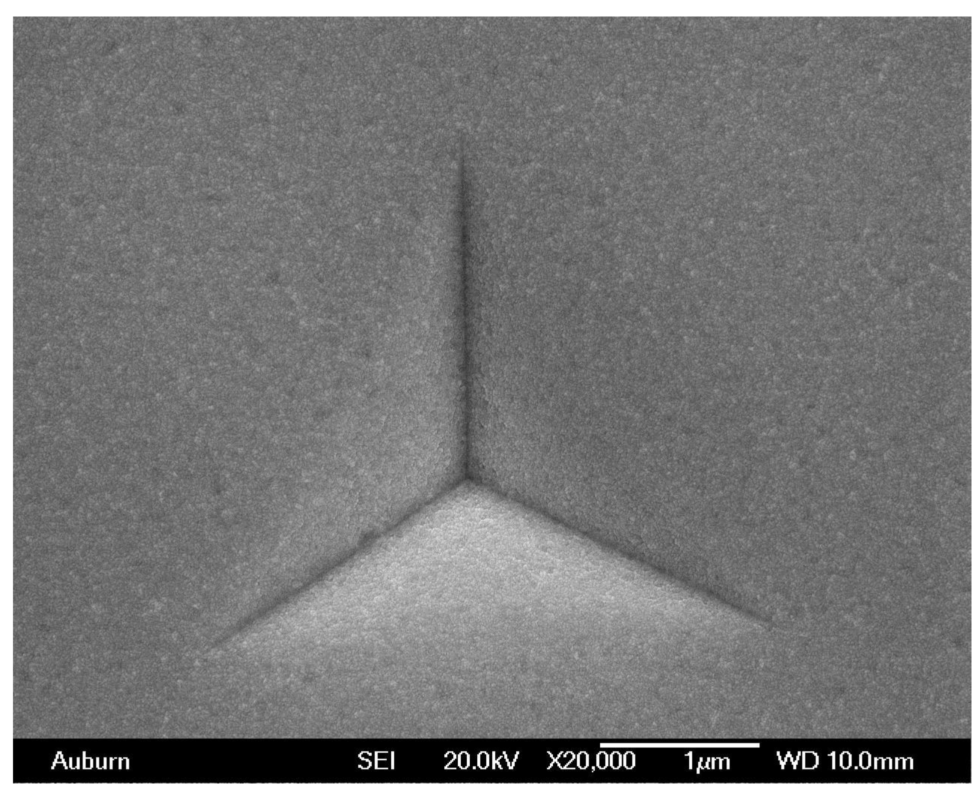

Figure 5.1.5d 230nm Pt on Cu: 500nm indention.

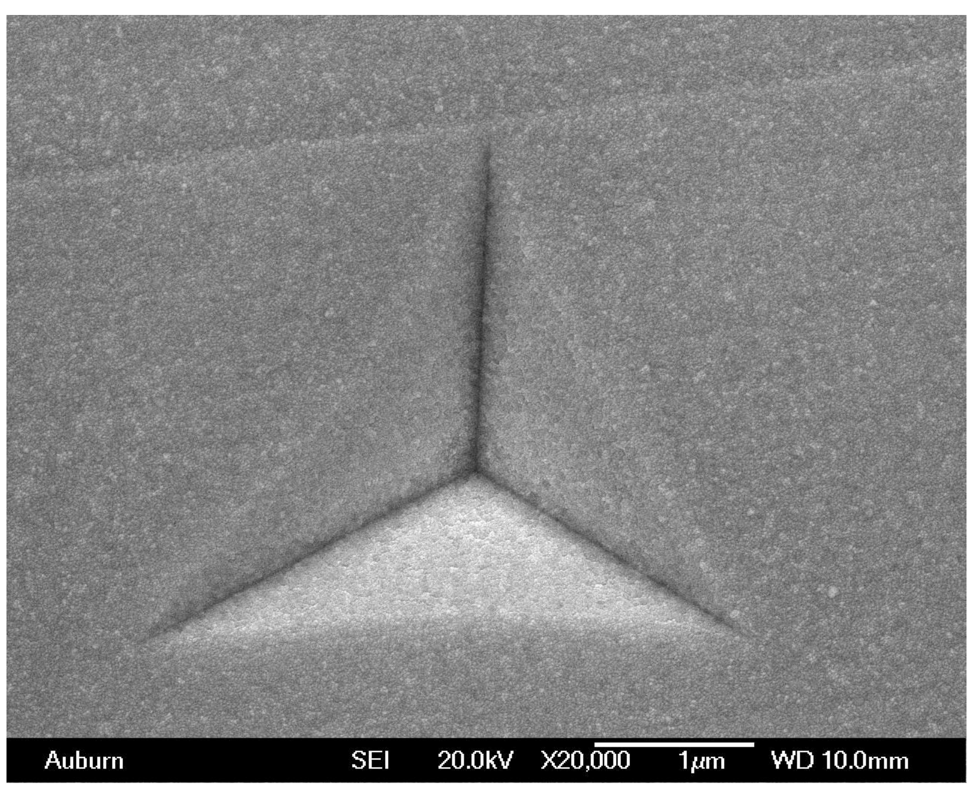

Figure 5.1.5e 230nm Pt on Ti: 500nm indention.

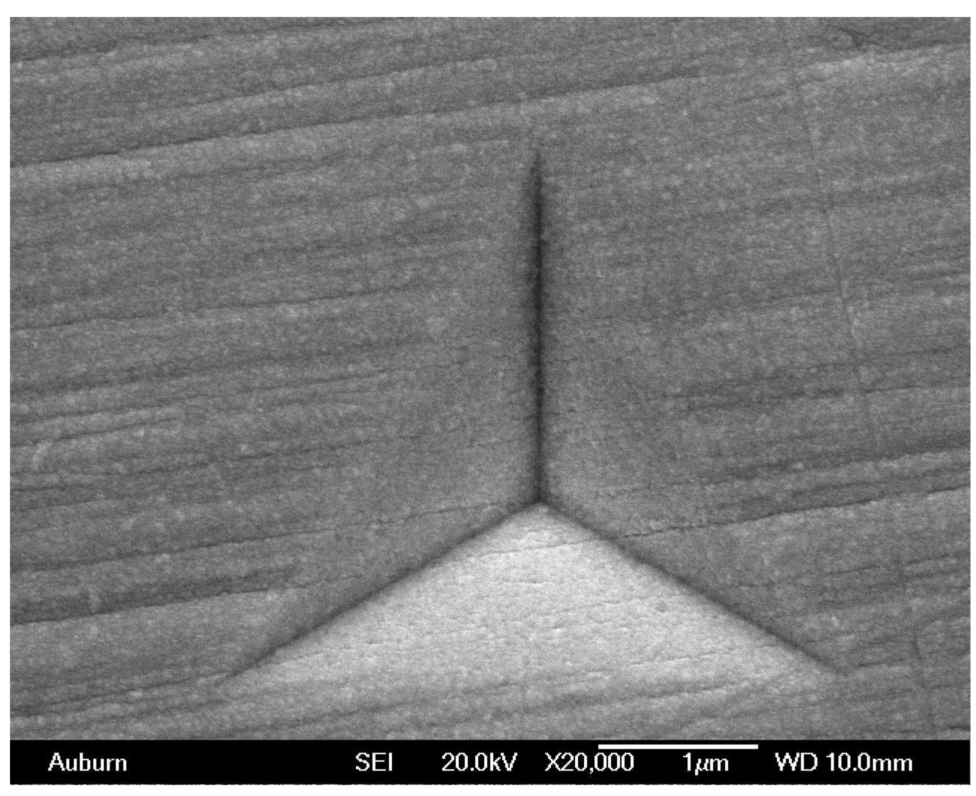

Figure 5.1.5f 230nm Pt on Pt: 500nm indention.

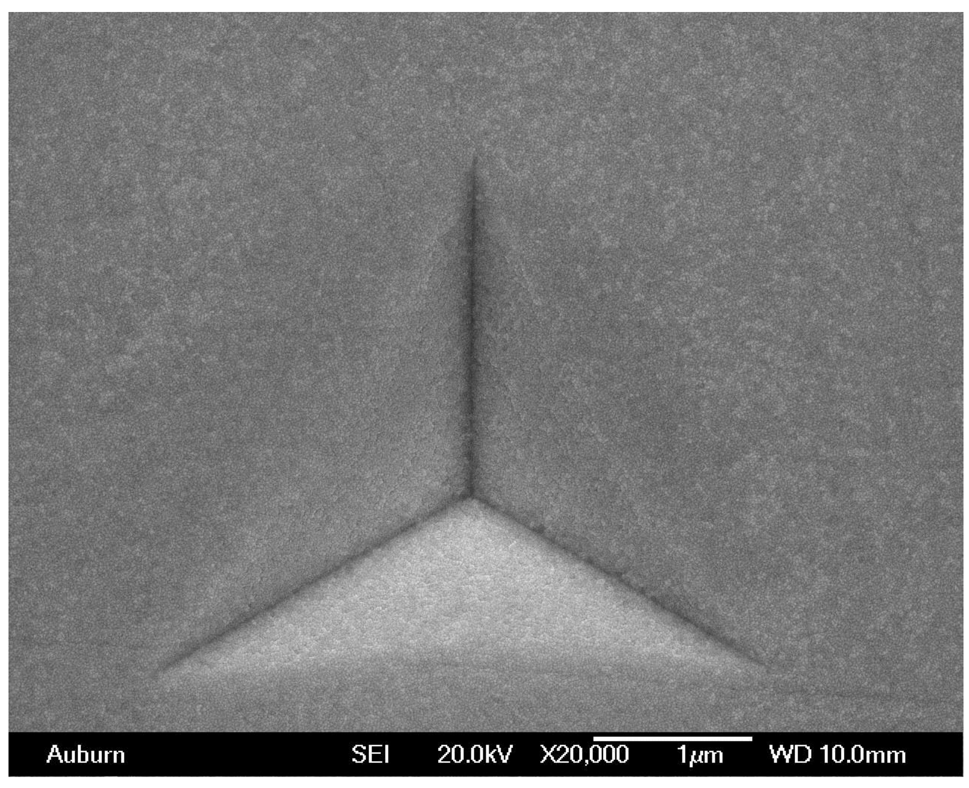

Figure 5.1.5g 230nm Pt on Ta: 500nm indention.

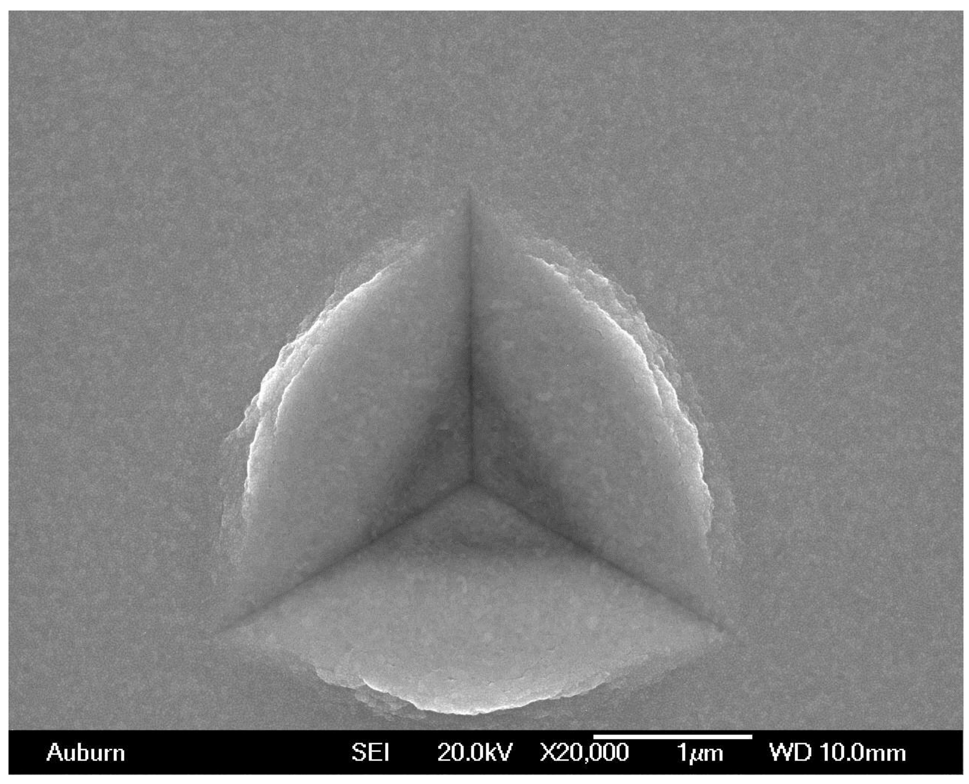

Figure 5.1.5h 230nm Pt on Si: 500nm indention.

It is obvious that for the Pt on In sample, the surface quality is not smooth enough for accurate nanoindentation data. Nonetheless, the indentation does show unusual behavior for the film's modulus from the Z-P model that may not be entirely resultant of the surface quality. It was noticed that the residual indention in the Pt-In surface was much smaller than that of the other materials, so another micrograph at 1,000 magnification was taken, Figure 5.1.6. In this micrograph there is a visible halo of deformation that spreads out wider than the readily identifiable indention shown in Figure 5.1.5a. It is believed that since the film is so much more stiff that as the tip pushes down on the film, a larger area of the film than that just below the tip begins to push down on the substrate; as demonstrated in Figure 5.1.7 (b, c). Shortly after the tip contacts the film's surface, the film's modulus as calculated through the Z-P model starts to rise toward its correct value, but once the previously mechanism becomes dominate, there is more plastic deformation than expected, allowing for less elastic recovery, so the film's modulus starts

to drop toward that of the substrate as the substrate becomes the driving force for elastic recovery.

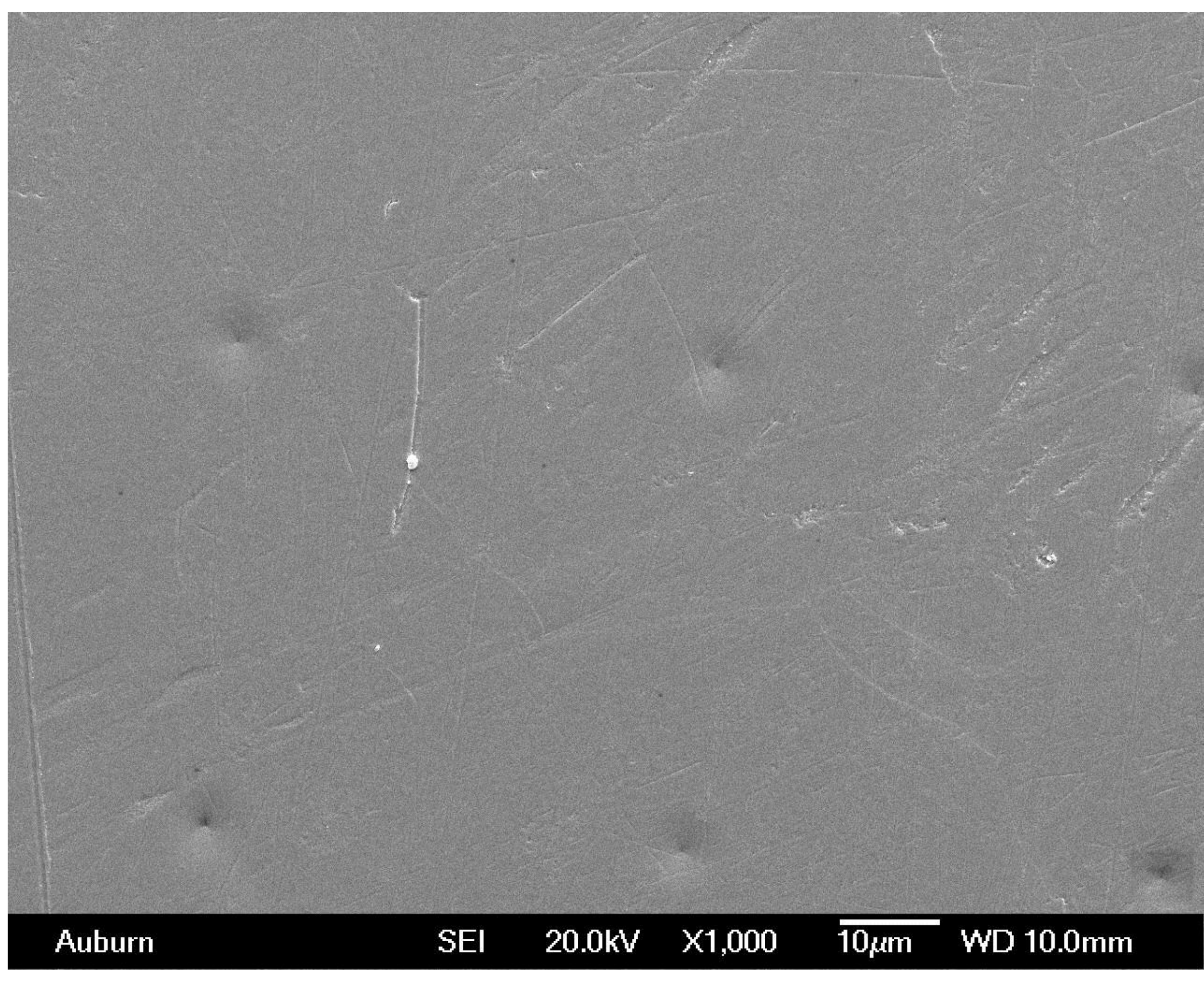

Figure 5.1.6 500nm indentions into 230nm Pt on Indium have a larger radius of volume than indicated by sharp edges shown in the 20,000 magnification.

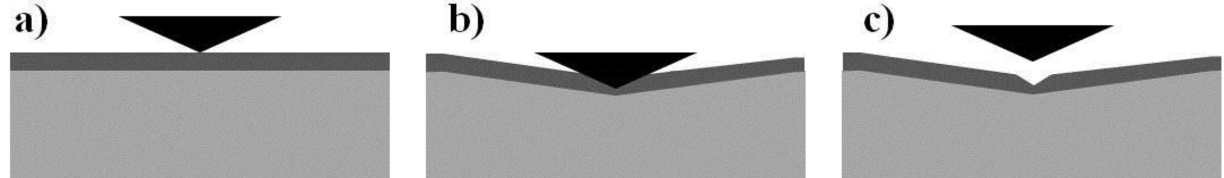

Figure 5.1.7 Stiff film plastically deforming a larger area than typical in a softer substrate, causing the readily visible residual indention to be much smaller than if deformation was localized to under the tip.

In Figure 5.1.4b the Sn sample showed a constant film E and alpha that correspond to the correct values, something dramatic happens to them near 0.6 to 0.8 normalized displacement, or 140 to 190nm indention depth. It is interesting to note that this depth roughly correlates to a large change in the substrate's Young's modulus in Figure 5.1.3b. While this bump in the Sn substrate's *E-h* curve is partially attributed to pile-up, it is believed another mechanical behavior of Sn under deformation contributes to the change in E; twinning. For the Pt-Sn sample the *E-h* curve behaves correctly until the load onto the sample allows for enough energy for the Sn substrate to start deformation twinning. Once twinning occurs, the amount of energy available for elastic recovery diminishes, reducing the perceived Young's modulus.

There is an interesting question to be asked after looking at micrographs of the 500nm indentions into all of the film-substrate combinations; why is there no discernible penetration into the substrate except for the platinum on silicon sample? The most reasonable answer would be that the films are not 230nm thick, but that is very unlikely to be the case as each sample had its film thickness measured in at least three, different, locations. Another explanation is that there is penetration into the substrate, but the micrographs are not showing it because the atomic number, Z, of some the substrates are similar to that of Pt. While this could possibly be the case

of tantalum, where Z = 73, as it is fairly close to Pt's Z of 78, it is unlikely the case for any other substrates. To follow up on that possibility more thoroughly, micrographs were taken of 500nm indentions into each sample using back-scattered electrons, as it is more dependent on the atomic number of the material. From the micrographs shown in Figures 5.1.7a through 5.1.7h, it is clear that the only substrate that is directly penetrated by the tip is silicon. To verify that what is being seen in Figure 5.1.7h is penetration into the Si substrate, EDS was performed on the surrounding film and indention, with results in Figure 5.1.8. While it is established that the film thickness is indeed 230nm, and that the substrate is indeed not being penetrated, it is not completely understood why this is the case. One possible explanation is that similar with the observed dispersed plastic deformation of indium, the substrates are plastically deforming in a wider volume than just under the indenter, allowing the film to bow out, absorbing some of the displacement.

In terms of range of applicability for the Zhou-Prorok model, there is one limitation due to a shortcoming of CSM nanoindentation at very shallow depths; loss of contact between the tip and surface due to the oscillation of the tip. While the current research could also indicate an inaccuracy with the model when there is a very large difference between the film and substrate's modulus as shown with the In substrate, there isn't enough information to confirm that assumption. The Indium sample's surface quality was not sufficient enough to draw conclusions about the Zhou-Prorok model's ability to predict film behavior. To either further understanding of the model's behavior with such an extreme case, it would be necessary to properly prepare the In sample through a more systematic method of mechanical flattening through use of rough surface contact models and controlling the load.[24, 25]

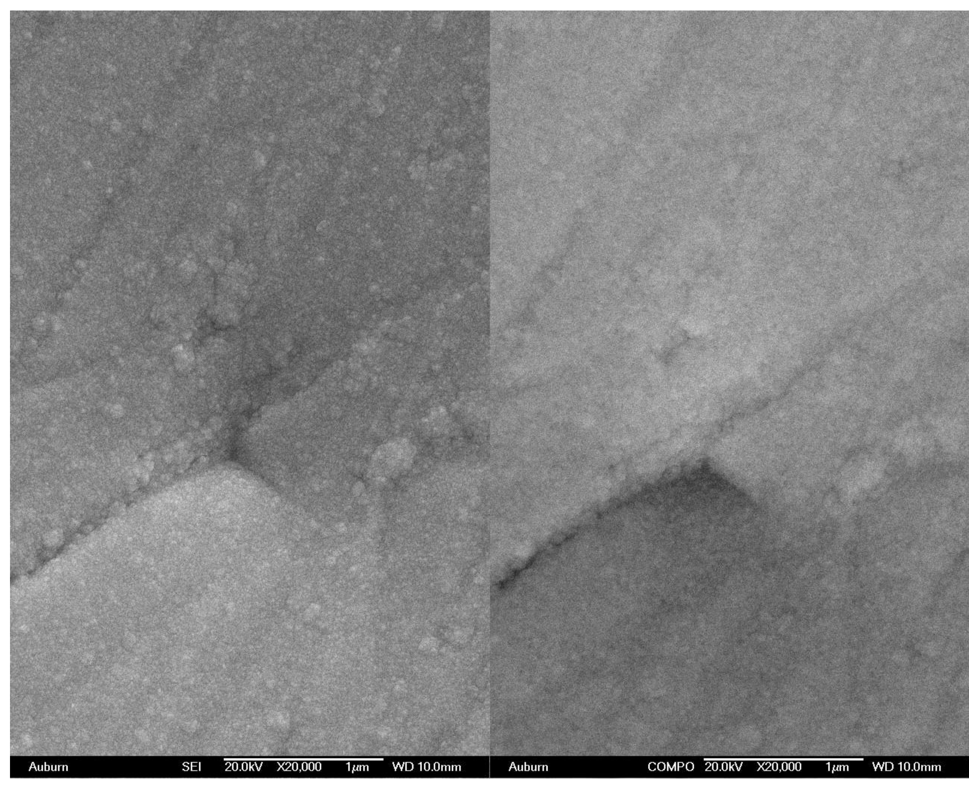

Figure 5.1.7a Micrograph of 230nm Pt on In. Left: secondary e^-. Right: back-scattered e^-.

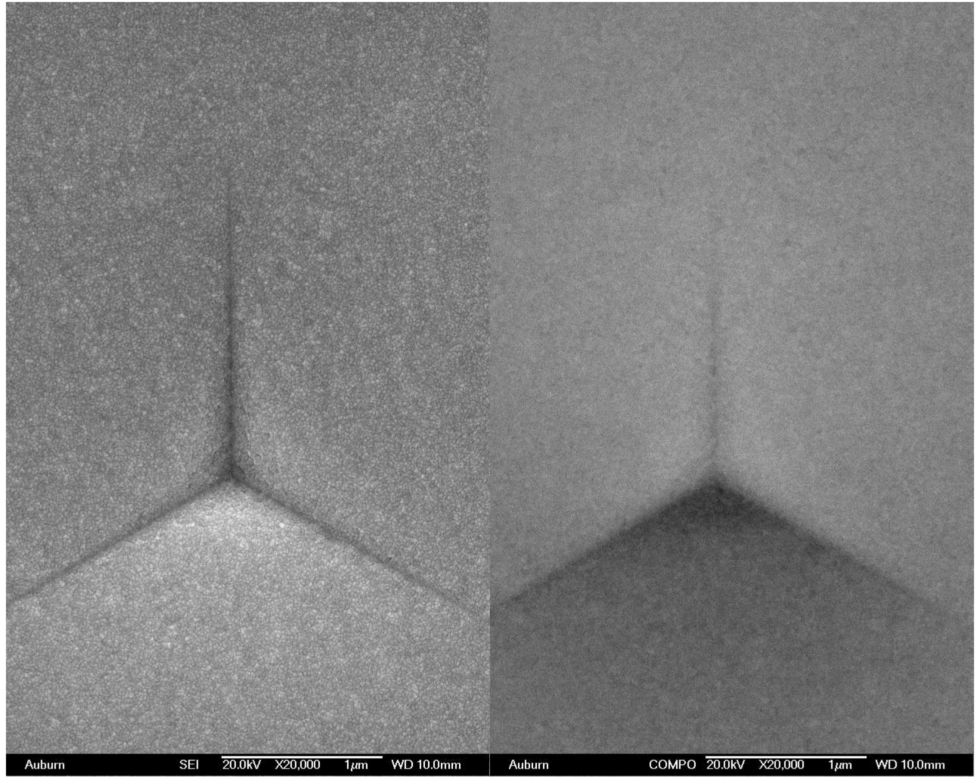

Figure 5.1.7b Micrograph of 230nm Pt on Sn. Left: secondary e^-. Right: back-scattered e^-.

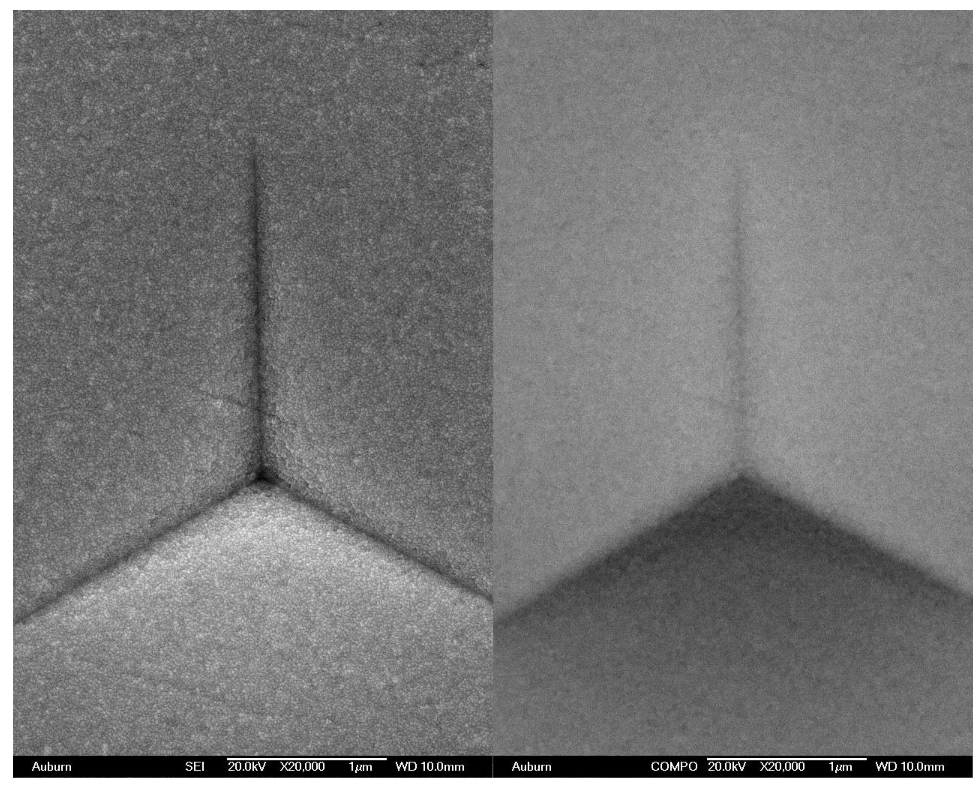

Figure 5.1.7c Micrograph of 230nm Pt on Al. Left: secondary e^-. Right: back-scattered e^-.

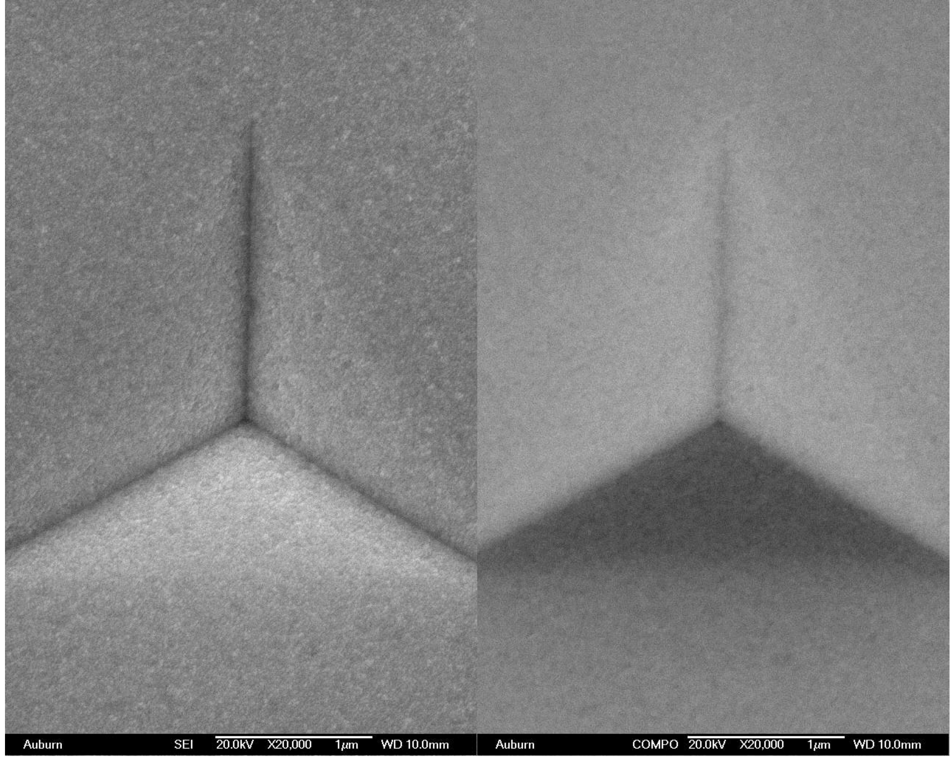

Figure 5.1.7d Micrograph of 230nm Pt on Cu. Left: secondary e^-. Right: back-scattered e^-.

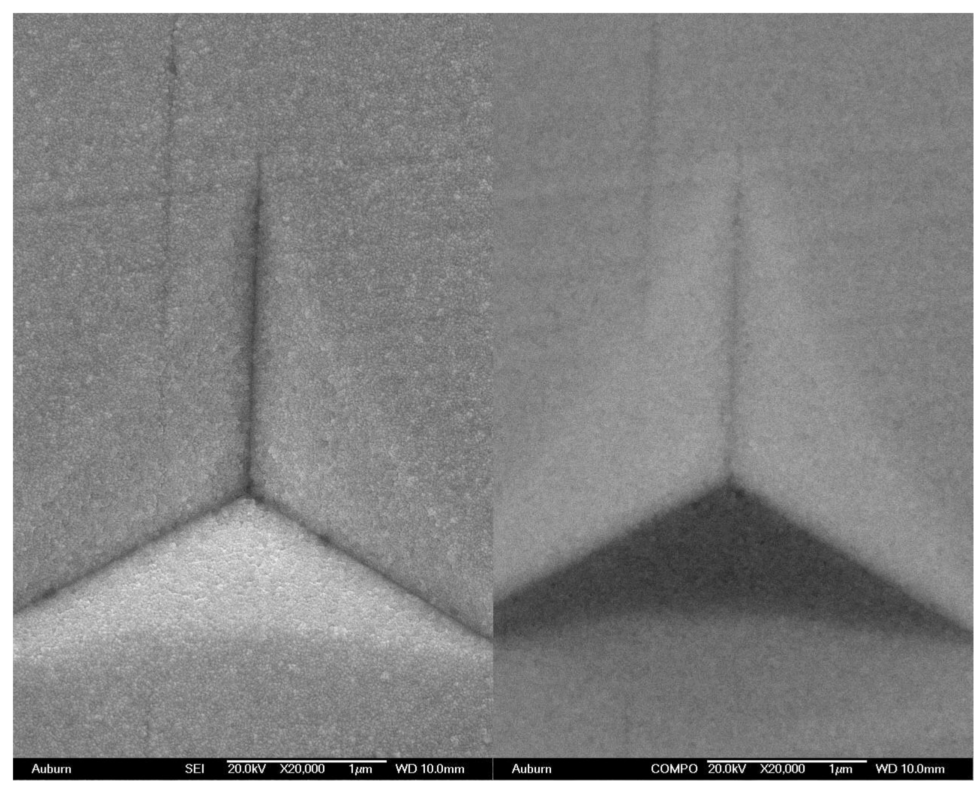

Figure 5.1.7e Micrograph of 230nm Pt on Ti. Left: secondary e^-. Right: back-scattered e^-.

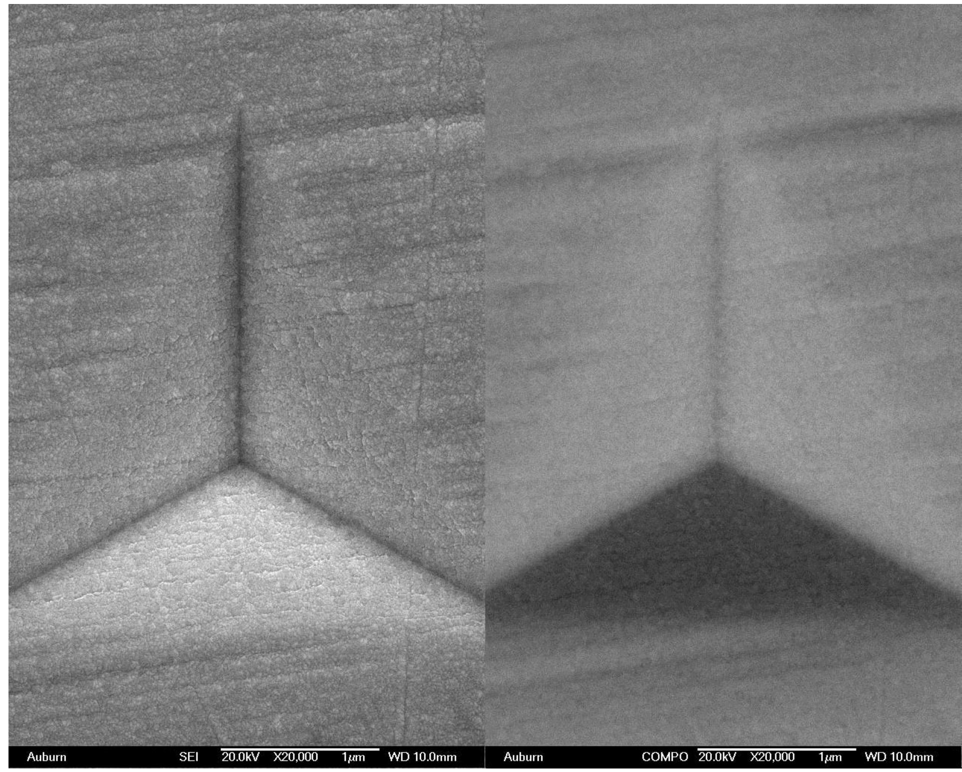

Figure 5.1.7f Micrograph of 230nm Pt on Pt. Left: secondary e^-. Right: back-scattered e^-.

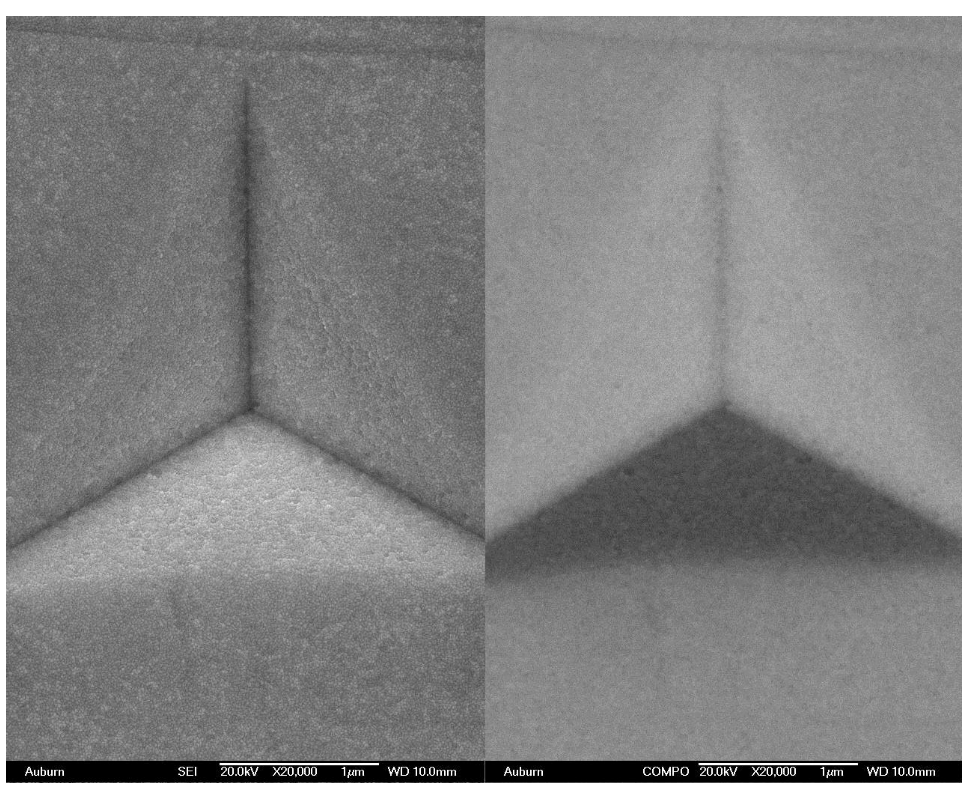

Figure 5.1.7g Micrograph of 230nm Pt on Ta. Left: secondary e^-. Right: back-scattered e^-.

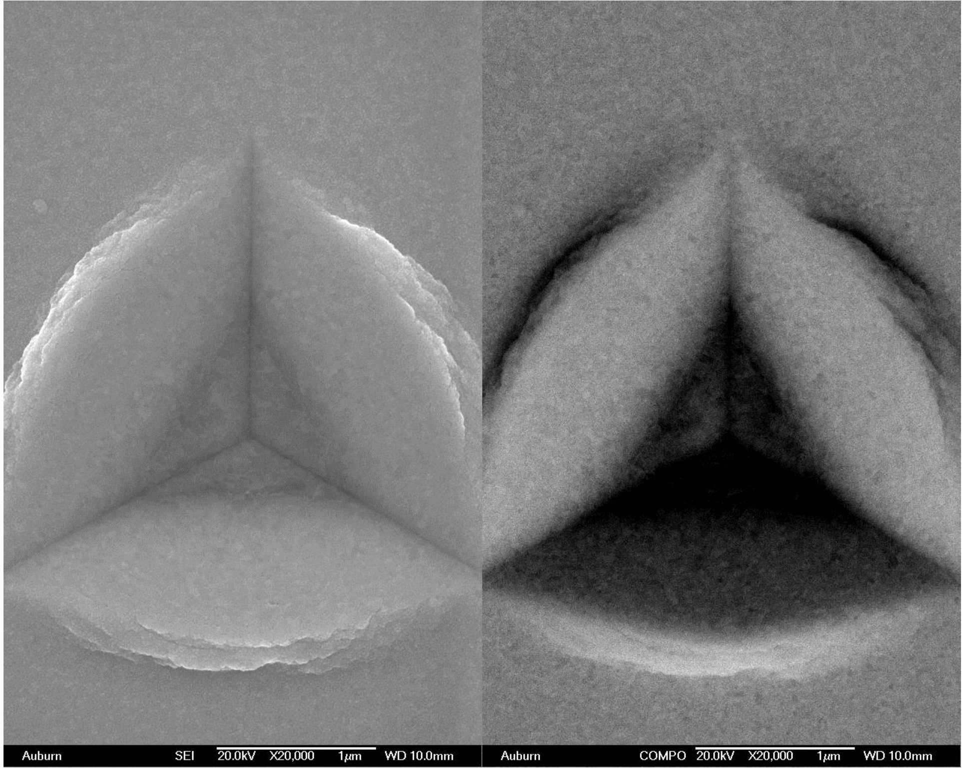

Figure 5.1.7h Micrograph of 230nm Pt on Si. Left: secondary e^-. Right: back-scattered e^-.

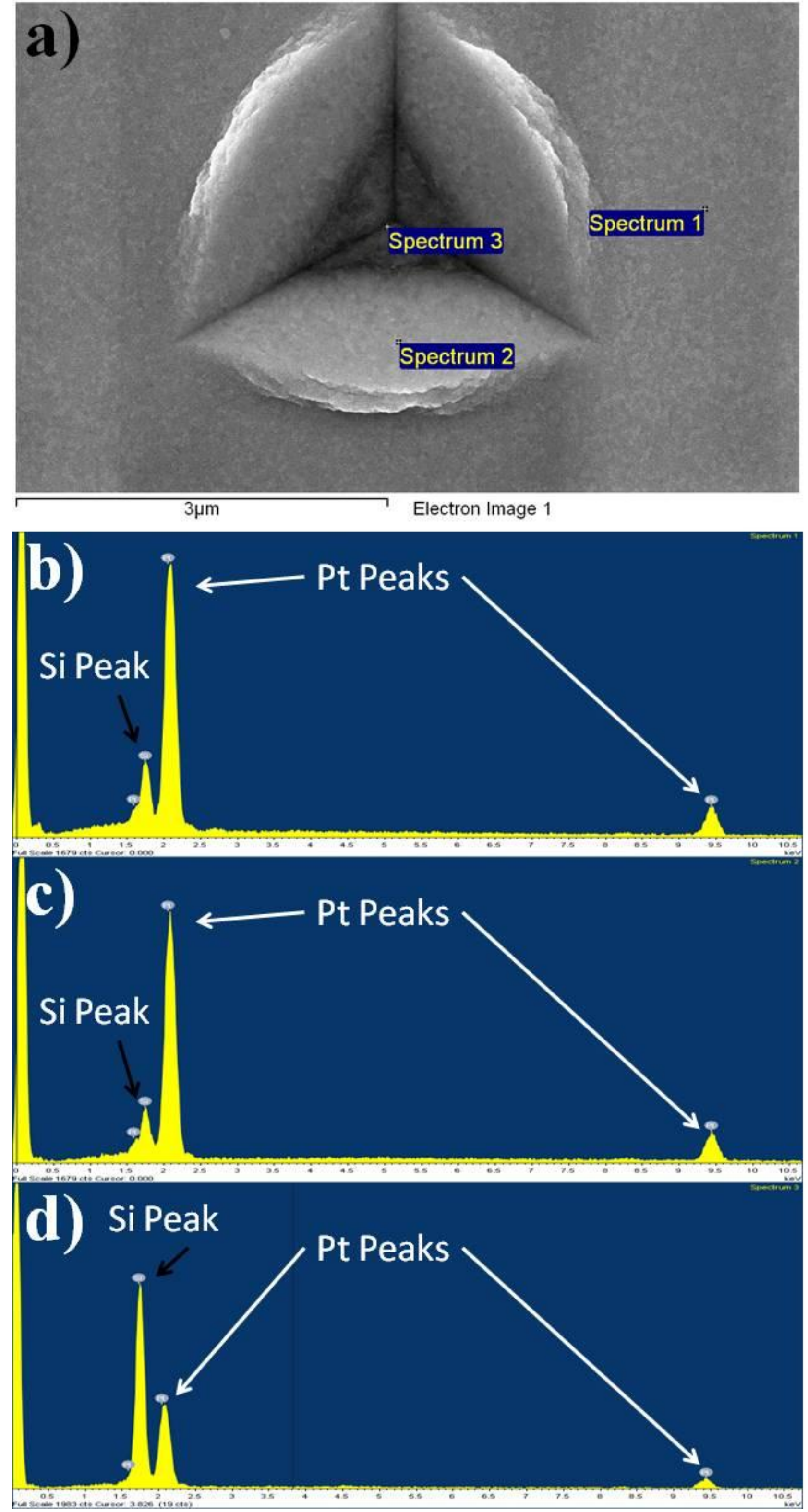

Figure 5.1.8 EDS of 500nm indention into 230nm Pt on Si. a) Spectrum locations for b) Spectrum 1, c) Spectrum 2 and d) Spectrum 3.

5.2 Validity of Zhou-Prorok Model in Investigated Materials

Although the behavior of film E and alpha being constant is a good indication that the Z-P model works well for the investigated stiff films on plastically deforming substrates, it is important to delve a bit deeper. Once the circumstances surrounding amiss *E-h* curves were well understood, the same process was followed as utilized by Zhou et al. in their derivation of their second model.[7] First, E_{flat} was plotted against E_s as a means to establish an estimated film modulus at where the points cross a line of elastic homogeneity shown by the dashed line in Figure 5.2.1; showing the Young's modulus of the film to be near the expected value of 168GPa.

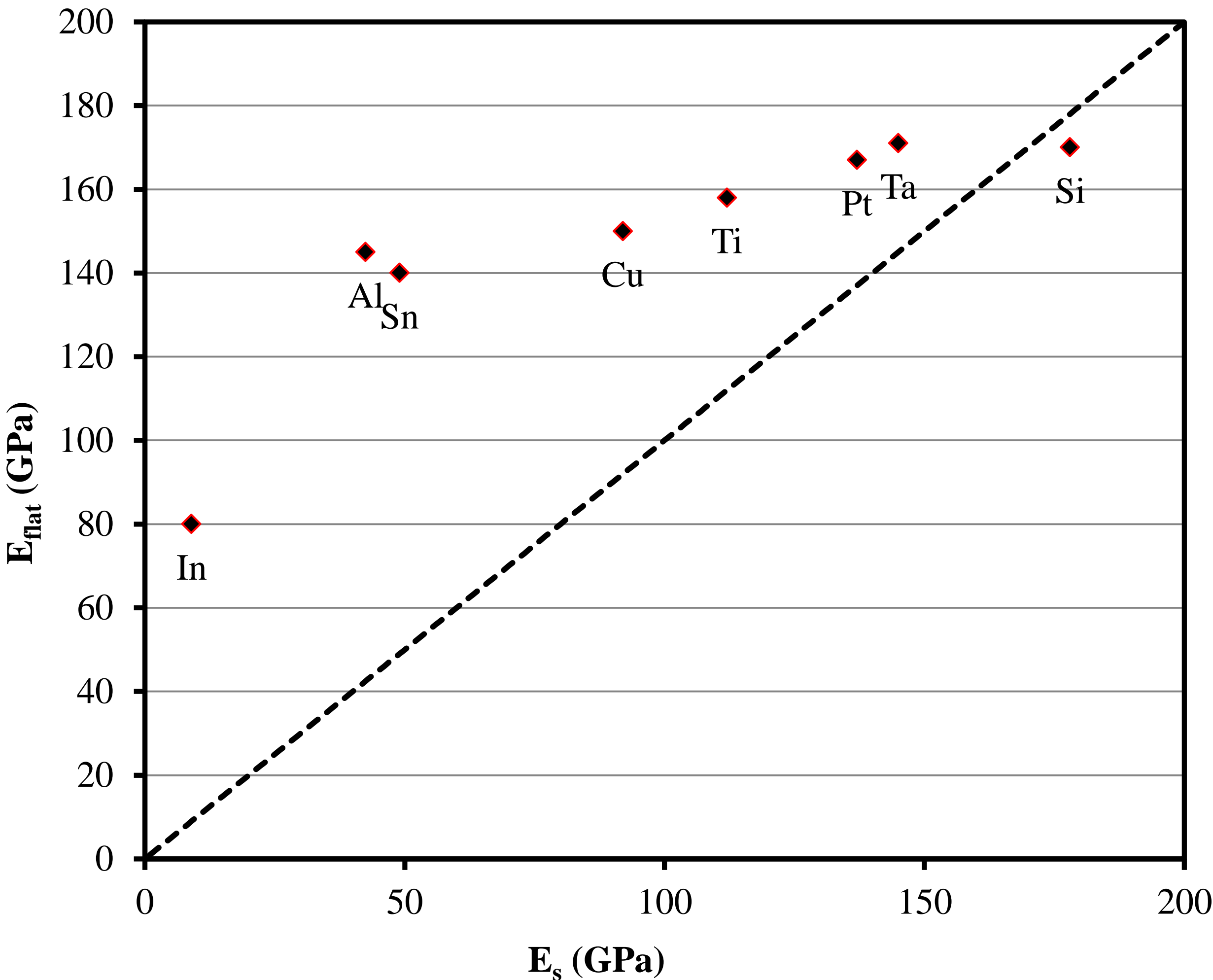

Figure 5.2.1 E_{flat} plotted against E_s for all substrates as a means to suggest the Pt film's actual Young's modulus by where it crosses the line of plastic homogeneity indicated by the dashed line.

The next pivotal step in their process was relating the ratios $\Delta E_f'/E_f'$ and E_s'/E_f' through the equation

$$\frac{\Delta E_f'}{E_f'} = \left(\frac{E_s'}{E_f'}\right)^{0.1} - 1 \quad (14)$$

where all boundary conditions were well known, except for the 0.1. This 0.1 was an empirically determined constant found by plotting the previously mentioned ratios against each other and creating a best fit line to describe their relationship; a power function of 0.1 as shown as the black X's in Figure 5.2.2.[7] This was repeated for the currently evaluated film-substrate combinations, and the same relationship persisted shown by the solid black diamonds.

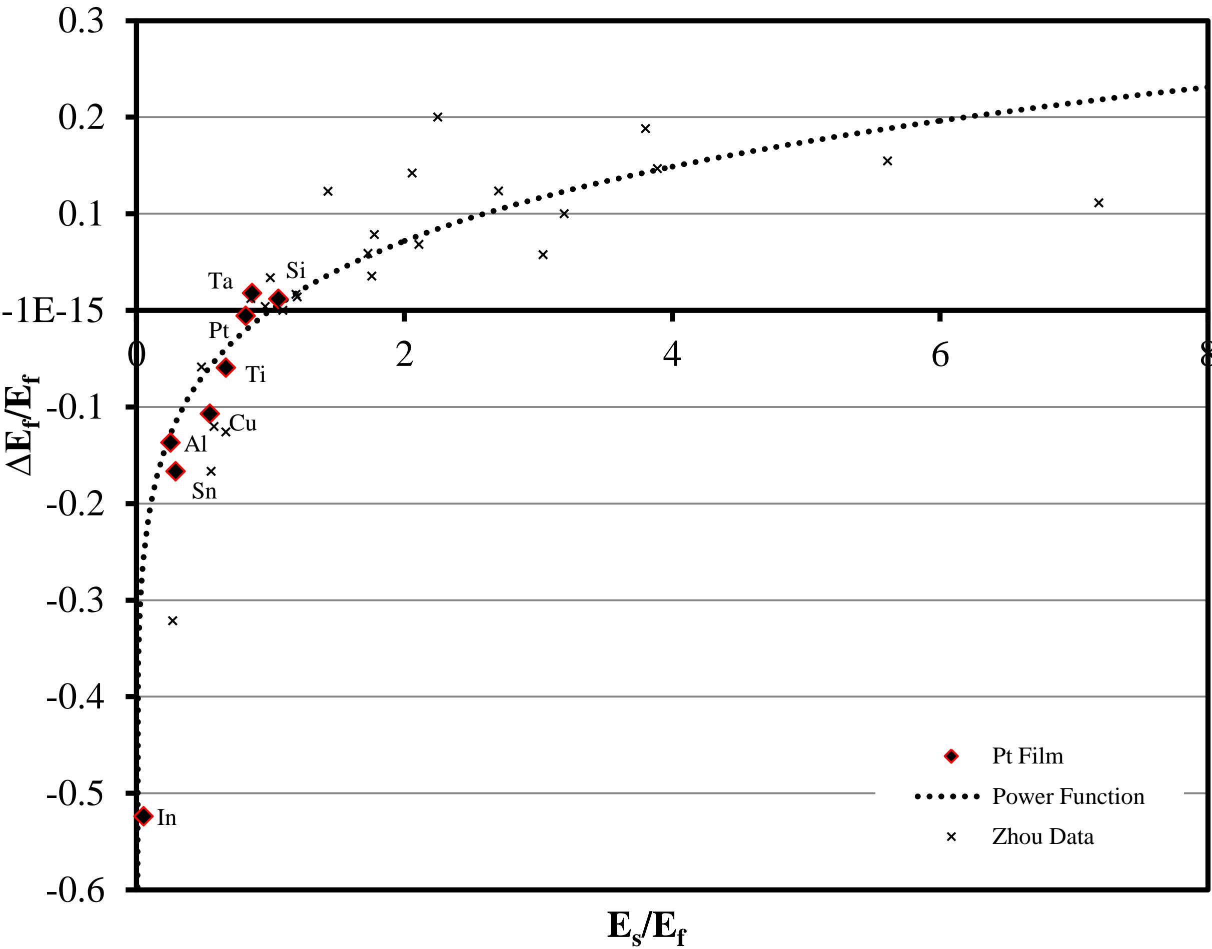

Figure 5.2.2 Plots of $\Delta E_f'$ verses the substrate modulus normalized by E_f'.

It is a worthy accomplishment that the Z-P model predicts behavior not only for their originally studied film-substrate combinations that were mostly compromised of substrates that do not plastically deform, but also for the currently investigated combinations with substrates

that do. To illustrate the wide variety of erroneous contact area that Z-P model works so well with, micrographs at a 70° tilt were taken for the 500nm indents into 230nm Pt on Si, Al, Ti, and Ta, as shown in Figures 5.2.3 through 5.2.6, in order to get a better perspective of pile-up and sink in, and the difference it will make on contact area and material behavior. For the 230nm Pt on Si sample, the film plastically deforms quite a bit, since the substrate is unable to, leading to a large quantity of pile-up. As the majority of film-sample combinations investigated by Zhou et al. have a similar behavior as Pt on Si, it is understandable or even expected that their model would predict the mechanical behavior well in this case. The current investigation shows another group of materials that the Z-P model performs well at predicting; substrates that are able to plastically deform. With a progression of harder substrates from Al to Ta, there is an evident increase in the residual indention depth and decrease in sink-in as the substrate increases in stiffness.

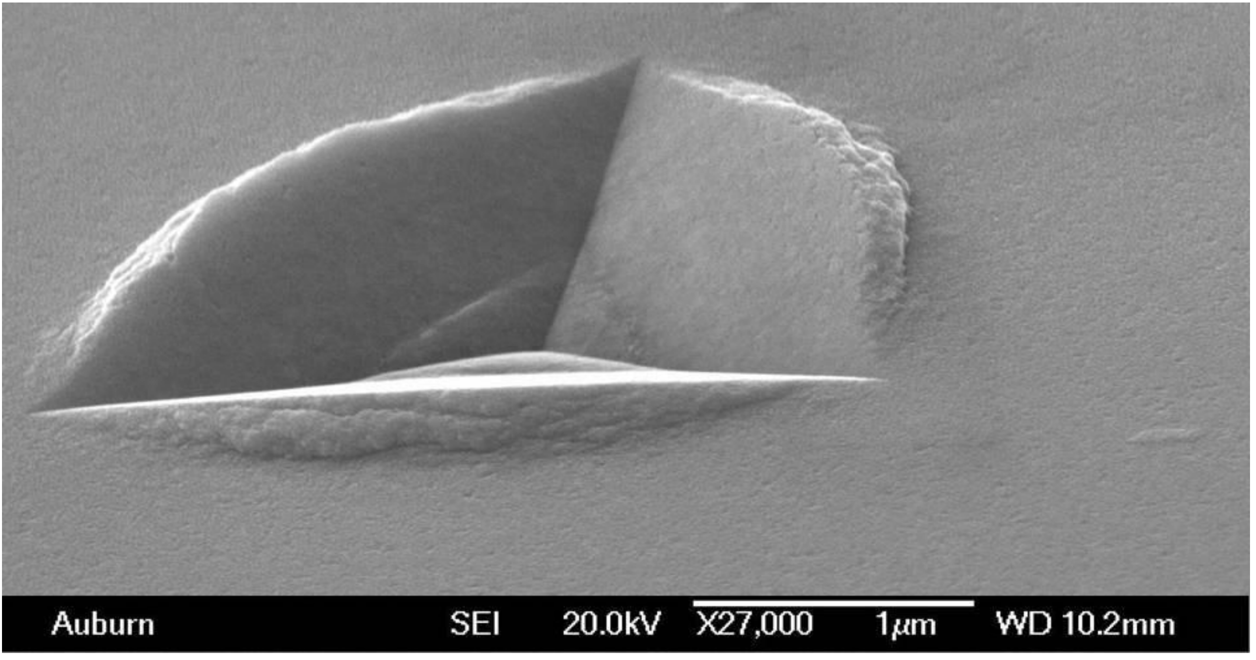

Figure 5.2.3 Micrograph of 230nm Pt on Si 500nm indention at a 70° tilt.

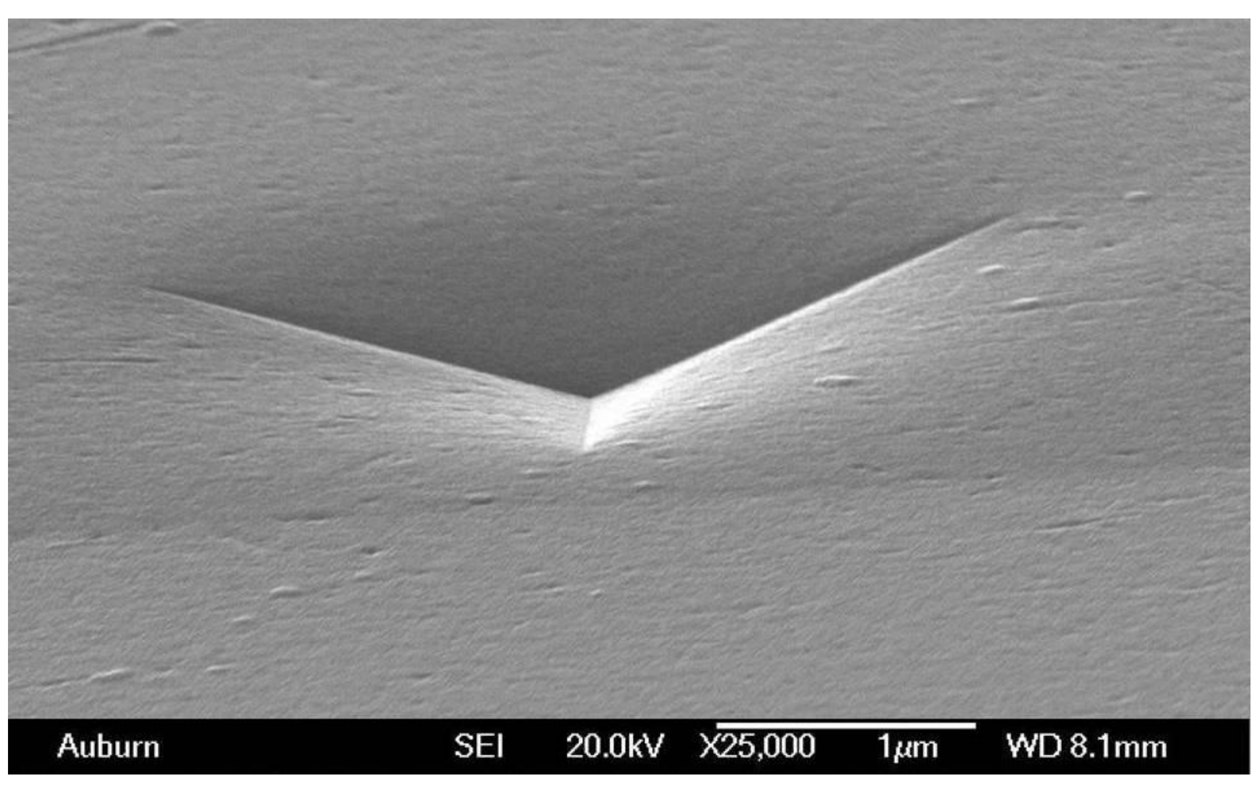

Figure 5.2.4 Micrograph of 230nm Pt on Al 500nm indention at a 70° tilt.

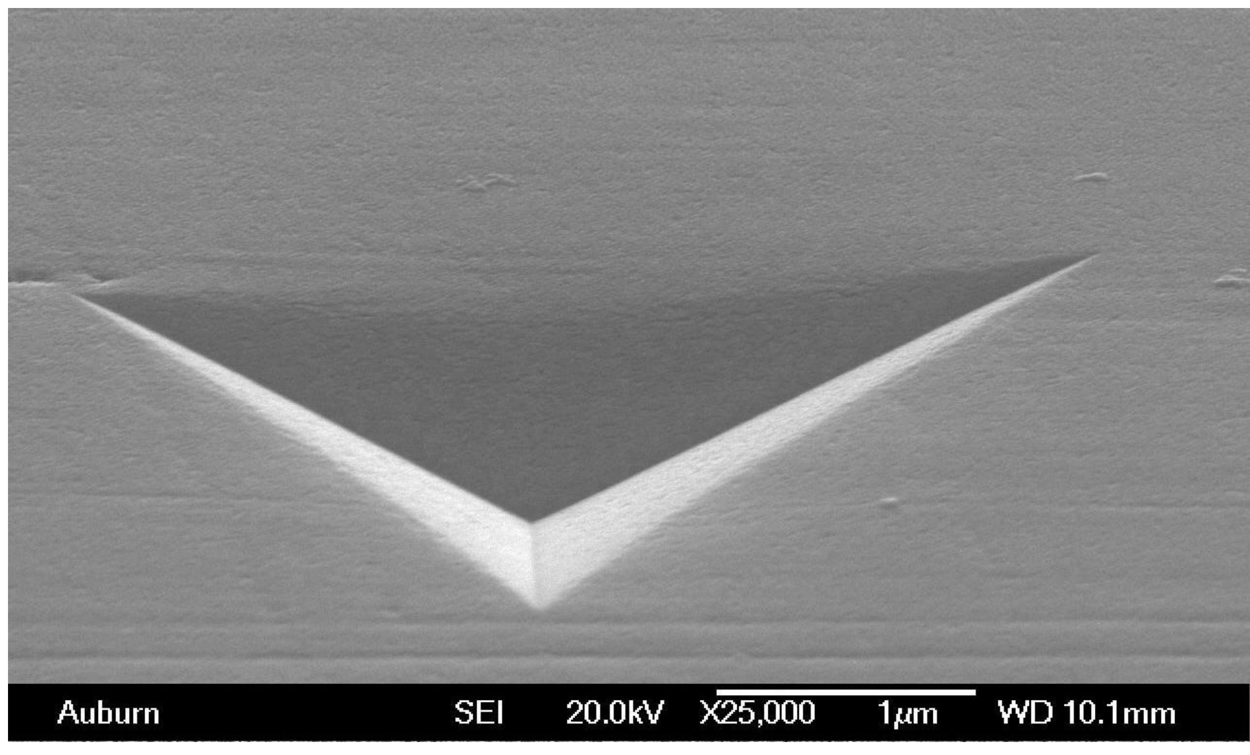

Figure 5.2.5 Micrograph of 230nm Pt on Ti 500nm indention at a 70° tilt.

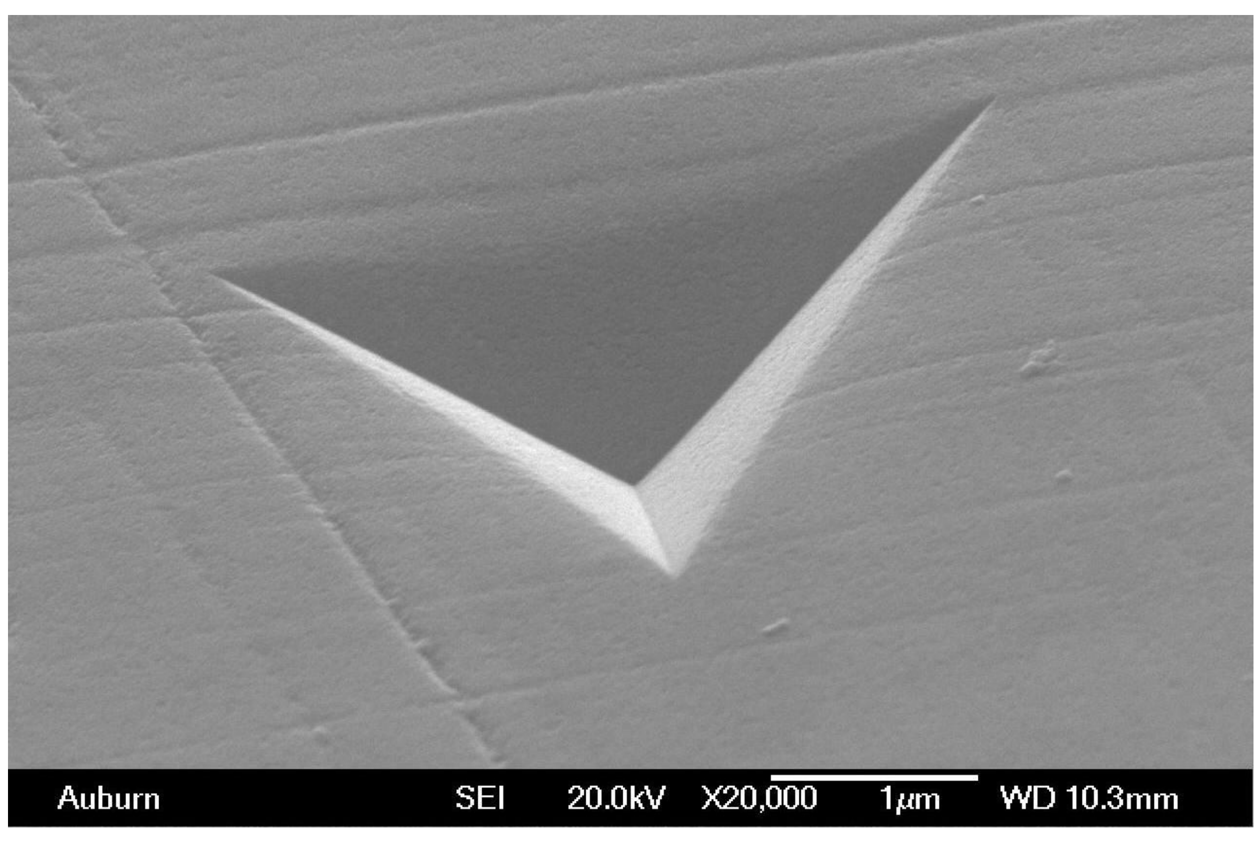

Figure 5.2.6 Micrograph of 230nm Pt on Ta 500nm indention at a 70° tilt.

Chapter 6: Conclusions

Instrumented indentation testing was used with the continuous stiffness method in order to evaluate nine different substrates, with the same film toward the goal to further evaluate the Zhou-Prorok model's ability to predict substrate effects during sink-in when the substrates are more willing to plastically deform. This was achieved by selecting plastically deforming substrates that have a high Poisson's ratio similar to that of the proposed film to be deposited onto them. First a deposition of aluminum was evaluated, but was determined to not be the ideal candidate due to Hillock growth grains prevalent on the surface. Even after optimizing the deposition parameters to reduce Hillock formation, the grains were determined to be much too large for nanoindentation data to be consistent or useful. A second candidate, platinum, was then looked at as it has a similar Poisson's ratio to aluminum, but is known to have a much better sputtered deposition surface quality.

Once deposited, the platinum film was evaluated through SEM and was found that surface quality and consistency were ideal for nanoindentation. The experimental data from indenting these samples was then compared to the model, and the associated extracted film's Young's modulus and Poisson's ratio to see to what degree they remain constant through indentation. The Zhou-Prorok model is adept at predicting substrate effect behavior for plastically deforming substrates, when sink-in is the dominating factor of erroneous contact area, not pile-up.

References

1. Doerner, M.F. and W.D. Nix, *A method for interpreting the data from depth-sensing indentation.* Journal of Materials Research, 1986. **1**(4): p. 601-609.

2. Hay, J. and B. Crawford, *Measuring substrate-independent modulus of thin films.* Journal of Materials Research, 2011. **26**(06): p. 727-738.

3. King, R.B., *Elastic analysis of some punch problems for a layered medium.* International Journal of Solids and Structures, 1987. **23**(12): p. 1657-1664.

4. Pharr, G.M., J.H. Strader, and W.C. Oliver, *Critical issues in making small-depth mechanical property measurements by nanoindentation with continuous stiffness measurement.* Journal of Materials Research, 2009. **24**(03): p. 653-666.

5. Saha, R. and W.D. Nix, *Effects of the substrate on the determination of thin film mechanical properties by nanoindentation.* Acta Materialia, 2002. **50**(1): p. 23-38.

6. Zhou, B. and B.C. Prorok, *A Discontinuous Elastic Interface Transfer Model of Thin Film Nanoindentation.* Experimental Mechanics, 2009. **50**(6): p. 793-801.

7. Zhou, B. and B.C. Prorok, *A new paradigm in thin film indentation.* Journal of Materials Research, 2010. **25**(09): p. 1671-1678.

8. *MTS Commercial Nanoindentation*. 2003 [cited 2011 June 11th]; Available from: http://www.nanoindentation.cornell.edu/pictures/schematic_nanoindenter.gif.

9. Prorok, B.C., et al., *Micro- and Nanomechanics.* Encyclopedia of Nanoscience and Nanotechnology, 2004. **5**: p. 555-600.

10. Li, X. and B. Bhushan, *A review of nanoindentation continuous stiffness measurement technique and its applications.* Materials Characterization, 2002. **48**(1): p. 11-36.

11. Zhou, B., *Exploration of the Origin of Substrate Effects and Elastic Strain Properties during Thin Film Nanoindentation*, in *Materials Engineering,* 2009, Auburn University: Auburn. p. 144.

12. McElhaney, K.W., J.J. Vlassak, and W.D. Nix, *Determination of indenter tip geometry and indentation contact area for depth-sensing indentation experiments.* Journal of Materials Research, 1998. **13**(5): p. 7.

13. Oliver, W.C. and G.M. Pharr, *An improved technique for determining hardness and elastic modulus using load and displacement sensing indentation experiments.* Journal of Materials Research, 1992. **7**(6): p. 1564-1583.

14. Rar, A., H. Song, and G.M. Pharr, *Assessment of new relation for the elastic compliance of a film-substrate system.* Thin Films: Stresses and Mechanical Properties IX, 2002. **695**: p. 431.

15. Hertzberg, R.W., *Deformation and Fracture Mechanics of Engineering Materials*. 4th ed1996: John Wiley & Sns, Inc.

16. Kulkarni, A.V. and B. Bhushan, *Nano/picoindentation measurements on single-crystal aluminum using modified atomic force microscopy.* Materials Letters, 1996. **29**(4-6): p. 221-227.

17. Branger, V., et al., *Study of the mechanical and microstructural state of platinum thin films.* Thin Solid Films, 1996. **275**(1-2): p. 22-24.

18. Fang, T.-H., W.-J. Chang, and C.-I. Weng, *Nanoindentation and nanomachining characteristics of gold and platinum thin films.* Materials Science and Engineering: A, 2006. **430**(1-2): p. 332-340.

19. Quiñones, C., W. Vallejo, and F. Mesa, *Physical and electrochemical study of platinum thin films deposited by sputtering and electrochemical methods.* Applied Surface Science, 2011. **257**(17): p. 7545-7550.

20. Espinosa, H.D., B.C. Prorok, and M. Fischer, *A methodology for determining mechanical properties of freestanding thin films and MEMS materials.* Journal of Mechanics and Physics of Solids, 2003. **51**: p. 46-67.

21. Furukawa, M., et al., *Surface morphologies of sputter-deposited aluminum films studied using a high-resolution phase-measuring laser interferometric microscope.* Appl. Opt., 1996. **35**(4): p. 701-707.

22. Herman, D.S., M.A. Schuster, and R.M. Gerber, *Hillock Growth on Vacuum Deposited Aluminum Films.* Journal of Vacuum Science and Technology, 1972. **9**(1): p. 515-519.

23. Voutsas, A.T., et al., *Structure engineering for hillock-free pure aluminum sputter deposition for gate and source line fabrication in active-matrix liquid crystal displays.* Journal of Vacuum Science & Technology A: Vacuum, Surfaces, and Films, 1998. **16**(4): p. 2668-2677.

24. Archard, J.F., *Elastic Deformation and the Laws of Friction.* Proceedings of the Royal Society of London. Series A, Mathematical and Physical Sciences, 1957. **243**(1233): p. 190-205.

25. Jackson, R., *An Analytical Solution to an Archard-Type Fractal Rough Surface Contact Model.* Tribology Transactions, 2010. **53**(4): p. 543-553.